

1. Report No. Research Report RC-1438	2. Government Accession No.	3. MDOT Project Manager Roger Till	
4. Title and Subtitle Durable Link Slabs for Jointless Bridge Decks Based on Strain-Hardening Cementitious Composites		5. Report Date November 16, 2003	
7. Author(s) Victor C. Li (Principal Investigator) G. Fischer, Y. Kim, M. Lepech, S. Qian, M. Weimann and S. Wang		6. Performing Organization Code	
9. Performing Organization Name and Address The Advanced Civil Engineering Material Research Laboratory Department of Civil and Environmental Engineering University of Michigan, Ann Arbor, MI 48109-2125, U. S. A.		8. Performing Org Report No.	
12. Sponsoring Agency Name and Address Michigan Department of Transportation Construction and Technology Division P.O. Box 30049 Lansing, MI 48909		10. Work Unit No. (TRAIS)	
		11. Contract Number: Master Contract #95-0242	
		11(a). Authorization Number: Work Auth #12	
15. Supplementary Notes		13. Type of Report & Period Covered Nov.1,2001- Nov.16,2003	
		14. Sponsoring Agency Code	
16. Abstract <p>The research presented herein describes the development of durable link slabs for jointless bridge decks based on strain-hardening cementitious composite - engineered cementitious composite (ECC). Specifically the superior ductility of ECC was utilized to accommodate bridge deck deformations imposed by girder deflection, concrete shrinkage, and temperature variations, providing a cost-effective solution to a number of deterioration problems associated with bridge deck joints.</p> <p>Current design concept of link slabs was first examined to form the basis of design for ECC link slabs. Microstructurally optimized ECC material, with good workability and satisfactory mechanical properties was then developed. After the material design, the shrinkage, shrinkage crack resistance and the freeze-thaw behavior of the pre-selected mix proportion was investigated and revealed excellent for the durability concern. Improved design of ECC link slab/concrete deck slab interface was confirmed in numerical analysis and further strengthened by excellent reinforcement pullout and shear stud pushout behavior in ECC.</p> <p>Based on the above findings, monotonic and subsequent cyclic tests of full-scale ECC link slab specimens were performed and compared with those of a conventional concrete link slab. It was revealed that the inherent tight crack width control of ECC decouples the dependency of crack width on the amount of reinforcement. This decoupling allows the simultaneous achievement of structural need (lower flexural stiffness of the link slab approaching the behavior of a hinge) and durability need (crack width control) of the link slab. Overall investigation supports the contention that durable jointless concrete bridge decks may be designed and constructed with ECC link slabs. Finally, a simple design guideline is presented.</p>			
17. Key Words ECC link slab, Jointless bridge deck, Strain-hardening, Durability, Crack width control		18. Distribution Statement No restrictions. This document is available to the public through the Michigan Department of Transportation.	
19. Security Classification (report) Unclassified	20. Security Classification (Page) Unclassified	21. No of Pages	22. Price

Final Report
on

Durable Link Slabs for Jointless Bridge Decks
Based on Strain-Hardening Cementitious Composites

By

Victor C. Li (Principal Investigator), G. Fischer, Y. Kim,
M. Lepech, S. Qian, M. Weimann and S. Wang

The Advanced Civil Engineering Material Research Laboratory
Department of Civil and Environmental Engineering
University of Michigan, Ann Arbor, MI 48109-2125, U. S. A.

Submitted to
Michigan Department of Transportation
November 16, 2003

Research Sponsor: Michigan Department of Transportation
MDOT Project Manager: Roger Till
Award Reference No: Master Cont #95-0242 Wrk Auth #12
Contract Period: Nov. 1, 2001 – Nov.16, 2003

DISCLAIMER

The contents of this report reflect the views of the authors, who are responsible for the facts and accuracy of the information presented herein. This document is disseminated under the sponsorship of the Michigan Department of Transportation, in the interest of information exchange. The Michigan Department of Transportation assumes no liability for the contents or use thereof.

Acknowledgments

The presented research has been sponsored by the Michigan Department of Transportation which is gratefully acknowledged. The authors thank the Michigan DOT projector manager David Juntunen, Roger Till and other members of the MDOT Research Advisory Panel for their useful comments, discussions and support.

Table of Contents

Table of Contents	i
List of Tables	ii
List of Figures	iii
1.0 Introduction-----	1
1.1 Background -----	1
1.2 Goal and impact-----	3
1.3 Overview -----	4
2.0 Literature review -----	4
2.1 Current design concept of link slabs-----	5
2.2 Analysis of current design procedure-----	10
3.0 ECC material design-----	13
3.1 Property Requirements of ECC for link slabs-----	13
3.2 Freeze-thaw durability consideration on design of ECC-----	15
3.3 ECC designed for link slab application -----	16
3.4 Long term tensile strain capacity -----	20
4.0 Shrinkage and shrinkage crack resistance-----	21
4.1 Determination of free shrinkage properties -----	22
4.2 Determination of restrained shrinkage properties -----	25
5.0 Freeze-thaw durability -----	29
5.1 Pore size distribution -----	29
5.2 Freeze-thaw exposure testing -----	30
5.3 Tensile testing of freeze-thaw specimens -----	35
5.4 Compression testing of freeze-thaw specimens-----	36
6.0 Design of ECC link slab/concrete deck slab interface-----	40
6.1 Conventional and improved interface design methods-----	40
6.2 Analysis of bridge model-----	42
7.0 Testing of ECC link slab/concrete deck slab interface -----	44

7.1 Development length of reinforcements in ECC -----	45
7.1.1 Specimen design and experimental setup/procedure -----	45
7.1.2 Pullout test results -----	49
7.2 Lap splice length of reinforcements in ECC -----	51
7.3 Stud shear connection in ECC -----	53
7.3.1 Experimental preparation and setup -----	53
7.3.2 Pushout behavior of concrete and ECC specimens -----	55
7.3.3 Load capacity of stud shear connection in concrete and ECC -----	58
8.0 Laboratory testing of ECC link slab -----	59
8.1 Design of test specimens -----	59
8.2 Experimental setup and procedure -----	65
8.3 Monotonic Behavior of Link Slab Specimens -----	68
8.4 Fatigue crack resistance -----	74
8.5 Conclusions from laboratory testing of ECC link slab -----	78
9.0 Design Guideline of ECC link slab -----	81
10.0 Conclusions -----	87
11.0 Appendix -----	90
11.1 Non-Linear Sectional Analysis -----	90
11.2 Simplified Loading of Bridge Span-----	92
12.0 References-----	94

List of Tables

Table 3.1	ECC mix proportions by weight -----	16
Table 3.2	PVA-ECC initial tensile test results -----	19
Table 3.3	Mix proportion of Mix 45 ECC by weight in a cubic yard -----	19
Table 3.4	Tensile Strain Capacity Development of M45 ECC -----	20
Table 5.1	ECC and reference concrete mix designs (lb/yd ³) -----	31
Table 5.2	Freeze-thaw tensile test results -----	36
Table 5.3	Freeze-thaw and fog room curing compressive strength -----	37
Table 7.1	Mix Proportion of ECC and concrete by weight and compressive strength (fiber by volume) -----	45

Table 7.2	Calculated, measured strength, and slip capacity of a stud in concrete and ECC -----	59
Table 8.1	Comparison between laboratory testing condition and field condition---	67

List of Figures

Figure 1.1	Typical tensile strain-stress behavior of ECC -----	2
Figure 2.1	Simplified geometry and loading of two-span bridge structure -----	5
Figure 2.2	Cross-sectional dimensions and reinforcement of link slab in uncracked condition - -----	6
Figure 2.3	Deformed shape of link slab at imposed rotation angle θ -----	6
Figure 2.4	Cross-sectional dimensions and reinforcement of link slab in cracked condition -----	7
Figure 2.5	Stress in longitudinal reinforcement at expected rotation angle as a function of reinforcement ratio -----	9
Figure 2.6	Stress state in link slab at imposed rotation angle θ -----	10
Figure 2.7	Analogous deformation controlled element in tension -----	11
Figure 2.8	Moment rotation relationship of link slab element -----	12
Figure 3.1	Permeability coefficient as a function of crack width -----	14
Figure 3.2	Schematical simply supported two span bridge with jointless deck (Assuming hinge-roller-roller-hinge support) -----	14
Figure 3.3	Particle size distributions of solids -----	17
Figure 3.4	Representative tensile stress-strain behavior of ECC (M34 and M45) ---	18
Figure 3.5	Tensile stress-strain and crack width-strain curves for ECC M45 -----	18
Figure 3.6	Demonstrations of ECC workability in patching of a bridge deck for (a) mixing in a 12ft ³ capacity drum mixer; and (b) pouring without any vibration -----	20
Figure 3.7	Typical stress-strain curve for M45 ECC at 6 months-----	21
Figure 3.8	Tensile strain capacity development of M45 ECC-----	21
Figure 4.1	Specimen dimensions and test setup -----	22
Figure 4.2	Drying shrinkage as a function of relative humidity-----	23
Figure 4.3	Mean annual relative humidity in the U.S.A. (AASHTO, 1996) -----	24

Figure 4.4	Test setup for measurement of the crack width of restrained shrinkage---	26
Figure 4.5a	Dimension of test specimen (plan view) -----	26
Figure 4.5b	Dimension of test specimen (side view section A-A) -----	27
Figure 4.6	Average crack width development over time (obtained from ring tests) -	28
Figure 4.7	Permeability coefficient as a function of crack width (from Wang et al., 1997) -----	29
Figure 5.1	ECC pore size distribution -----	30
Figure 5.2	Freeze-Thaw test results showing (a) dynamic modulus, and (b) relative dynamic modulus -----	32
Figure 5.3	Regular Concrete Normal Curing and Freeze-Thaw Specimens-----	33
Figure 5.4.	M34 ECC Normal Curing and Freeze-Thaw Specimens-----	34
Figure 5.5	M45 ECC normal curing and Freeze-Thaw specimens -----	34
Figure 5.6	M45LA ECC normal curing and Freeze-Thaw specimens -----	35
Figure 5.7	Stress-Strain Curve for ECC Normal Curing and Freeze-Thaw Specimens -----	36
Figure 5.8	Comparison between (a) M45LA Freeze-thaw specimen: and (b) M45LA fog room curing specimen after compression testing -----	37
Figure 5.9	Concrete compressive strength vs. maturity (Mindess, 1981) -----	39
Figure 6.1	Comparison of interface design in LS between (a) conventional method and (b) improved method -----	41
Figure 6.2	Model of the bridge (close look at the link slab) -----	42
Figure 6.3	Normalized envelope stress developed at the top surface of link slab--	44
Figure 7.1	Exposed reinforcements before patch repair -----	46
Figure 7.2	Exposed No.3 reinforcementand threaded bars of pullout specimen before casting-----	47
Figure 7.3	Pullout test setup -----	48
Figure 7.4	LVDTs attached to the reinforcement for measurement of pullout displacement-----	48

Figure 7.5	Comparison of pullout load-displacement curves for No. 3 reinforcement(a) in concrete; (b) in ECC; and (c) No. 3 epoxy-coated reinforcement in ECC, with 6 inch embedment length (where yield load corresponds to the yield strength of bare steel reinforcement) -----	50
Figure 7.6	Lap splice of bars in concrete (J. G. MacGregor, 1998) -----	52
Figure 7.7	Comparison of pullout failure modes between ECC and concrete specimen -----	53
Figure 7.8	Geometry of a shear stud -----	53
Figure 7.9	Geometry of the pushout specimen (unit: inch) -----	54
Figure 7.10	Setup of pushout tests and close view of LVDTs -----	55
Figure 7.11	Comparison of pushout load per stud–average slip curves for specimens made of (a) concrete; (b) ECC M45+; (c) ECC M45-----	56
Figure 7.12	Macro cracks developed in concrete pushout specimen show a brittle failure mode-----	57
Figure 7.13	Microcracks developed outside (left) and inside (right, cut section along shear stud) of ECC specimen -----	57
Figure 8.1	Schematics of two span bridge subjected to point load at midspan for (a) deformed shape of bridges; and (b) moment distribution on bridge span and corresponding deformed shape of link slab region -----	61
Figure 8.2	Geometry of link slab specimens for (a) LS-1; (a) LS-2; and (b) LS-3 ---	62
Figure 8.3	Required minimum reinforcement ratio 0.013 (0.014 used in the test) designed at expected rotation angle (0.0015rad) -----	63
Figure 8.4	Laboratory test setup and instrumentation of specimen -----	66
Figure 8.5	Loading sequence, in which the midspan deflections at step4 corresponds to the load at the reinforcement stress equal to $0.4\sigma_y$ in specimen LS-1--	67
Figure 8.6	Applied load vs. midspan deflection curves during pre-loading test (step1: 0.06in., step2: 0.10in., step3: 0.14in., step4: 0.185in., and step5: 0.375in. in midspan deflection) on (a) LS-1; (b) LS-2; and (c) LS-3 -----	69

Figure 8.7	Strain distribution measured at three data points across the midspan section at each loading step (step1: 0.06in., step2: 0.10in., step3: 0.14in., step4: 0.185in., and step5: 0.375in. in midspan deflection) for (a) LS-1; (b) LS-2; and (c) LS-3 -----	70
Figure 8.8	Compatible deformation between ECC and steel reinforcement (right) showing microcracking in ECC with load transmitted via bridging fibers. In contrast, the brittle fracture of concrete in normal R/C (left) causes unloading of concrete, resulting in high interfacial shear and bond breakage (Fischer and Li, 2002) -----	72
Figure 8.9	Comparison of reinforcement stress in between R/C beam and R/ECC beam with the same geometry and reinforcement ratio at identical rotation angle, θ , and curvature, Φ -----	73
Figure 8.10	The response of midspan deflection vs. actuator force (load) behavior to cyclic deflection during cyclic test on specimen LS-3 -----	74
Figure 8.11	Stiffness change and crack width evolution of link slab specimens during cyclic test -----	75
Figure 8.12	Crack pattern marked with magic ink pen after cyclic test for (a) LS-1; (b) LS-2 and (b) LS-3 -----	77
Figure 8.13	Crack pattern marked with magic ink pen at interface zone for (a) LS-2; and (b) LS-3 -----	79
Figure 9.1	Simplified geometry and loading of two-span bridge structure -----	83
Figure 9.2	Cross-sectional dimensions and reinforcement of link slab in uncracked condition -----	84
Figure 9.3	Deformed shape of link slab at imposed rotation angle θ -----	84
Figure 9.4	Schematic stress and strain profile in a cross section of link slab for calculation of required longitudinal reinforcement ratio (profile of R/C is shown for comparison) -----	85
Figure 9.5	Design chart for required longitudinal reinforcement ratio -----	86
Figure 9.6	Conceptual illustration of the interface design between ECC link slab and concrete deck -----	87

Figure 11.1 Strain and stress profile in a cross section of ECC link slab for calculation
of required longitudinal reinforcement ratio/moment capacity -----90

Figure 11.2 Schematics of two span simply supported bridge and loading for (a)
resultant of HS-20, and (b) HS-20 -----93

1.0 Introduction

1.1 Background

Many highway bridges are composed of multiple span steel or prestressed concrete girders simply supported at piers or bents. The girders support cast-in-place concrete decks. A mechanical joint is typically employed at the end of the simple span deck to allow deck deformations imposed by girder deflection, concrete shrinkage, and temperature variations. It is well known that bridge deck joints are expensive to install and maintain. Deterioration of joint functionality due to debris accumulation can lead to severe damage in the bridge deck and substructure. The durability of beam ends, girder bearings, and supporting structures can be compromised by water leakage and flow of deicing chemicals through the joints. A significant negative economic impact of mechanical joints in all phases of bridge service life, from design to construction and maintenance, was documented by Wolde-Tinsae and Klinger (1987). A possible approach to alleviate this problem is the elimination of mechanical deck joints in multispan bridges.

Two solutions to elimination of deck joints have been attempted in the US, specifically an integral construction concept with girder continuity and a jointless bridge deck concept with simply supported girders. Alampalli and Yannotti (1998) found that the jointless deck construction practice is generally more efficient than the integral bridge construction practice. Based on field inspection of 105 jointless bridge decks, including 72 with concrete superstructures and 33 with steel superstructures, it was found that the bridges were functioning as designed without significant problems except for minor deck cracking. The performance of the jointless decks was inferior in bridges with concrete superstructures, with 12 out of 72 decks receiving condition rating of 4. While further improvement on jointless bridge deck construction practice was recommended, Alampalli and Yannotti concluded that as a group, they generally perform better than decks with joints.

The section of the deck connecting the two adjacent simple-span girders is called the link slab. Caner and Zia (1998) experimentally analyzed the performance of jointless bridge decks and proposed design methods for the link slab. These investigations revealed that the link slab was subjected to bending under typical traffic conditions rather

than axial elongation. Tensile cracks were observed at the top of the link slab under service conditions due to a negative bending moment. For steel girders, the measured maximum crack width was 0.012” at 40% of ultimate load and 0.030” at 67% of ultimate load. They pointed out that additional tensile stress may be imposed on the link slabs due to shrinkage, creep, and temperature loading, and that crack width must be carefully controlled. The recommendation was to use epoxy coated reinforcing bars in the link slab in order to avoid reinforcement corrosion. To reduce the stiffness of the link slab, debonding of the link slab over the girder joint for a length equal to 5% of each girder span was also recommended. This link slab concept can be used for new bridge decks and also for replacement of deteriorated joints of existing bridge decks.

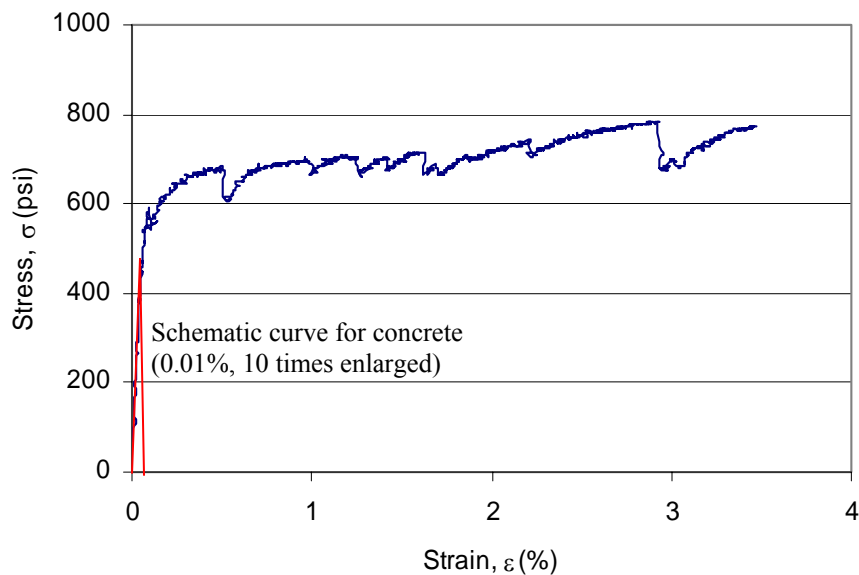


Figure 1.1 Typical tensile stress-strain behavior of ECC

Engineered Cementitious Composite (ECC) is a high performance fiber reinforced cementitious composite designed to resist tensile and shear force while retaining compatibility with normal concrete in almost all other respects (Li, 2002). Figure 1.1 shows the uniaxial tensile stress-strain curve of an ECC reinforced with Polyvinyl Alcohol (PVA) fiber. After first cracking, the composite undergoes plastic yielding and strain-hardening to a tensile strain of 3.5% prior to developing a macroscopic crack. The tensile strain capacity of ECC is about 350 times that of normal concrete (0.01%). ECC achieves strain-hardening with moderate amount of fibers (typically less than or equal to 2% by volume) compared to other high performance fiber reinforced concrete.

This is particularly important for practical field applications, where the mixing process must be simple and similar to that used in mixing and placing conventional concrete. As confirmed by studies on self-compacting ECC (Kong et al, 2003) and sprayable ECC (Kim et al, 2003), the fresh properties of ECC can be adjusted by optimizing the composition of ECC for given workability requirements. Thus, the introduction of ECC to link slab construction is proposed for its ability to control crack widths and its processing flexibility.

1.2 Goal and impact

The goal of this research is to provide a cost-effective solution to bridge deck deterioration problems associated with joints, by developing durable and maintenance-free ECC link slabs used in jointless bridge decks. To achieve this goal, a number of requirements must be met. These include the design of ECC with properties satisfying mechanical requirements in the link slab under normal service and environmental loading conditions, and assuring the durability of the link slab, including the interface between ECC link slab and concrete bridge deck.

The effective use of ECC link slabs for retrofitting simple span bridges is expected to remedy a number of deterioration problems experienced by Michigan bridges, particularly those related to bridge deck joints. It is expected that the high resistance to cracking in ECC and its ability to accommodate deformation imposed by shrinkage, thermal variation, and live load will lead to crack free decks, effectively prolonging the life of bridge decks while minimizing the cost and inconvenience to the motorist public of continual maintenance.

The research program is expected to significantly impact the aged infrastructure locally and nationally. It directly addresses Item 2 (Methods to eliminate or improve bridge joints) identified as focus areas beneficial to the Michigan Department of Transportation (MDOT) in the document entitled “Strategic Research Program for Next Five Years – Bridges and Structures”. The proposed research also contributes to addressing Item 5 (Methods to increase life of bridge decks from 30 years to 75 years) and Item 7 (High performance concrete). Furthermore, according to Federal Highway Administration (FHWA) officials, 42% of the highway bridges in the USA should be

urgently rehabilitated, and the cost of rehabilitation is estimated at \$50 billion by the year 2010 (Ashley, 1996). The cost effective, maintenance-free ECC link slab may greatly improve the durability and service life of the country's bridges.

1.3 Overview

In Section 2, current design concept of link slabs will be discussed and examined. This information will form the basis of design for new link slabs by taking into account the superior ductility of the ECC material. For the ECC material design, property requirements of ECC for link slabs, particularly the tensile strain capacity, will first be determined, providing input for micromechanical design of ECC. As a result, microstructurally optimized ECC material, with good workability and satisfactory mechanical properties, will be available for use for link slabs. This part of work will be presented in Section 3. After the material design, the shrinkage, shrinkage crack resistance and the freeze-thaw durability of the pre-selected mix proportion will be investigated for the durability concern in Section 4 and 5, respectively.

The interface between ECC and concrete may form a weak link since the fibers in the ECC cannot penetrate the concrete. To address this potential problem, Section 6 and 7 will focus on the design and testing of ECC link slab/concrete deck slab interface. To reduce interfacial stress, special attention will be placed on strengthening measures, such as extension of shear studs into ECC link slab and lap splice of the existing longitudinal reinforcements with new reinforcing bars within the ECC link slab.

Based on the above findings, monotonic and subsequent cyclic tests of full-scale ECC link slab specimens were performed. The test results were compared with those of a conventional concrete link slab. The mode of deformation, fatigue cracking resistance, and design of link slab associated with the development of reinforcement stress and crack width, will be discussed in Section 8, followed by design guidelines of ECC link slabs in Section 9. The overall conclusions will be presented in Section 10.

2.0 Literature review of current link slab design concept

The assessment of current link slab design concepts is primarily based on a previous investigation carried out by Caner and Zia (1998). This design procedure has

been adopted by MDOT for laboratory investigations as well as for field applications. In addition, design recommendations from an FHWA report (Oesterle et al., 1999) are reviewed. Although the design procedure as recommended by FHWA report is not adopted in its entirety by MDOT, it will be included in this document.

2.1 Current design concept of link slabs (Caner and Zia, 1998)

The design concept for a reinforced concrete link slab with two identical adjacent spans outlined in Caner and Zia (1998) will be summarized in the following.

Notation of live load, geometry and material properties:

A_s	=	Total area of longitudinal reinforcement in link slab
B_{ls}	=	Width of link slab
E_c	=	Elastic modulus of concrete
H_{ls}	=	Height of link slab
$I_{ls,cr}$	=	Moment of inertia of link slab (cracked)
$I_{ls,g}$	=	Moment of inertia of link slab (uncracked)
I_{sp}	=	Moment of inertia of span (girder and concrete deck)
L_{dz}	=	Debond zone length = (5% of span length) x 2
L_{sp}	=	Span length (assuming same length for adjacent spans)
P	=	Live load
σ_{cr}	=	Flexural tensile strength of concrete

Step 1 Determine end rotation angle of spans θ

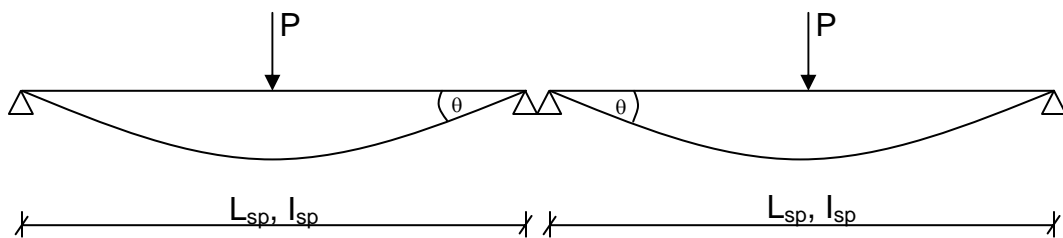


Figure 2.1 Simplified geometry and loading of two-span bridge structure

The rotation angle θ is a function of the geometry of the spans, their loading, and material properties. Assuming both spans are simply supported, the rotation angle can be derived as

$$\theta = \frac{PL_{sp}^2}{16E_c I_{sp}} \quad (\text{Eq. 2-1})$$

Step 2 Determine moment of inertia of link slab (uncracked)

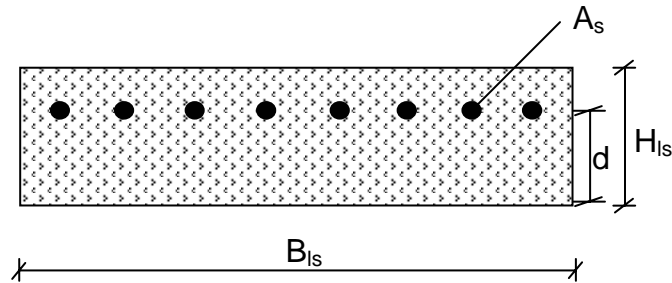


Figure 2.2 Cross-sectional dimensions and reinforcement of link slab in uncracked condition

The moment of inertia of the link slab in the uncracked conditions is a function of the cross-sectional geometry and independent of the reinforcement ratio $\rho = A_s / B_{ls} H_{ls}$.

$$I_{ls,g} = \frac{B_{ls} H_{ls}^3}{12} \quad (\text{Eq. 2-2})$$

Step 3 Determine moment M_a developed in the link slab at rotation angle θ

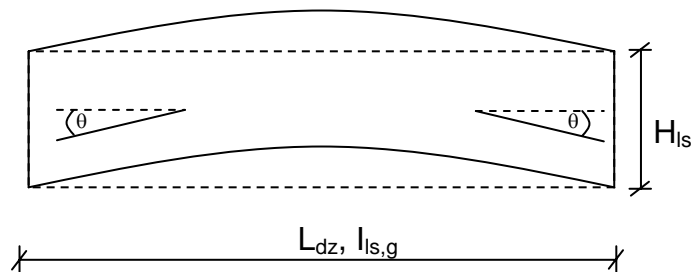


Figure 2.3 Deformed shape of link slab at imposed rotation angle θ

The moment developed in the uncracked link slab is a function of the material properties and geometrical dimensions. It is proportional to the imposed rotation angle θ .

$$M_a = \frac{2E_C I_{ls,g}}{L_{dz}} \theta \quad (\text{Eq. 2-3})$$

Step 4 Determine cracking moment M_{cr} in link slab

The cracking moment M_{cr} is a function of the first cracking strength of the cementitious material used in this particular link slab with given geometry.

$$M_{cr} = \frac{\sigma_{cr} I_{ls,g}}{\frac{H_{ls}}{2}} = \sigma_{cr} \frac{B_{ls} H_{ls}^2}{6} \quad (\text{Eq. 2-4})$$

Compare applied moment M_a to cracking moment M_{cr} .

Step 5 Select reasonable longitudinal reinforcement ratio $\rho = 0.01$

Step 6 Determine cracked moment of inertia I_{cr}

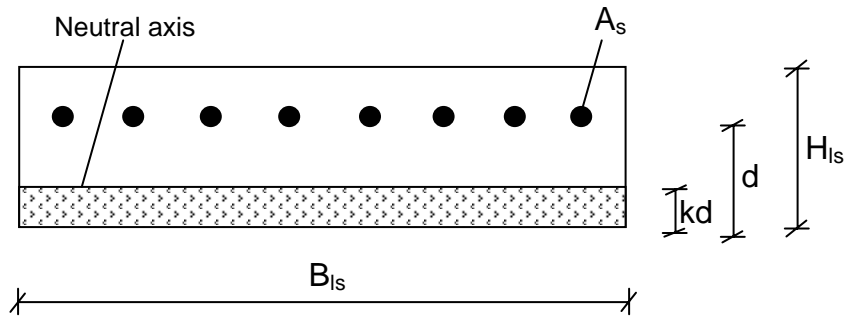


Figure 2.4 Cross-sectional dimensions and reinforcement of link slab in cracked condition

The cracked moment of inertia results from contributions of the uncracked portion below the neutral axis, of the reinforcement itself, and from the eccentricity of the reinforcement with respect to the neutral axis. With

$$n = \frac{E_s}{E_c} \quad (\text{Eq. 2-5})$$

and

$$k = -n\rho + \sqrt{(n\rho)^2 + 2(n\rho)} \quad (\text{Eq. 2-6})$$

follows

$$\begin{aligned}
 I_{ls,cr} &= \frac{B_{ls}(kd)^3}{12} + B_{ls}kd\left(\frac{kd}{2}\right)^2 + nA_s(d - kd)^2 \\
 &= \frac{B_{ls}(kd)^3}{3} + nA_s(d - kd)^2
 \end{aligned} \tag{Eq. 2-7}$$

The cracked moment of inertia is a function of the cross-sectional dimensions as well as of the reinforcement ratio ρ . Assuming a fixed position of the neutral axis and elastic material behavior, it will remain constant at increasing rotation angles θ .

Step 7 Determine stress in longitudinal reinforcement σ_s and compare with allowable stress $0.40\sigma_y$

The stress in the link slab reinforcement σ_s as derived in Caner and Zia (1998) is expressed as

$$\sigma_s = \frac{M_a}{M_{cr}} \frac{\sigma_{cr}}{6\rho\gamma^2\left(1 + \frac{1}{3}\left(n\rho - \sqrt{(n\rho)^2 + 2n\rho}\right)\right)} \tag{Eq. 2-8}$$

This expression indicates a dependency of the stress in the reinforcement on the ratio of applied moment M_a to the cracking moment of the link slab M_{cr} . However, with

$$\gamma = \frac{d}{H_{ls}} \tag{Eq. 2-9}$$

follows

$$\begin{aligned}
 \sigma_s &= \frac{M_a}{M_{cr}} \frac{\sigma_{cr}}{6 \frac{A_s}{\gamma B_{ls} H_{ls}} \left(\frac{d}{H_{ls}}\right)^2 \left(1 - \frac{1}{3}k\right)} = \frac{M_a}{M_{cr}} \frac{\sigma_{cr} \frac{B_{ls} H_{ls}^2}{6}}{A_s \left(d - \frac{1}{3}kd\right)} \\
 &= \frac{M_a}{A_s \left(d - \frac{1}{3}kd\right)} = \frac{\frac{2E_c I_{ls,g}}{L_{dz}} \theta}{A_s \left(d - \frac{1}{3}kd\right)} \leq 0.40 \sigma_y
 \end{aligned} \tag{Eq. 2-10}$$

In order to satisfy this condition ($\sigma_s < 0.40\sigma_y$), the amount of reinforcement A_s , i.e. the reinforcement ratio ρ , is to be adjusted (Figure 2.5). Although the ratio of applied moment M_a to cracking moment M_{cr} apparently enters the expression, the cracking moment ultimately cancels out and does not affect the stress in the longitudinal reinforcement. Note that in this expression, only the denominator is a function of the reinforcement ratio, while the numerator, i.e. the applied moment M_a , is independent of the amount of reinforcement provided.

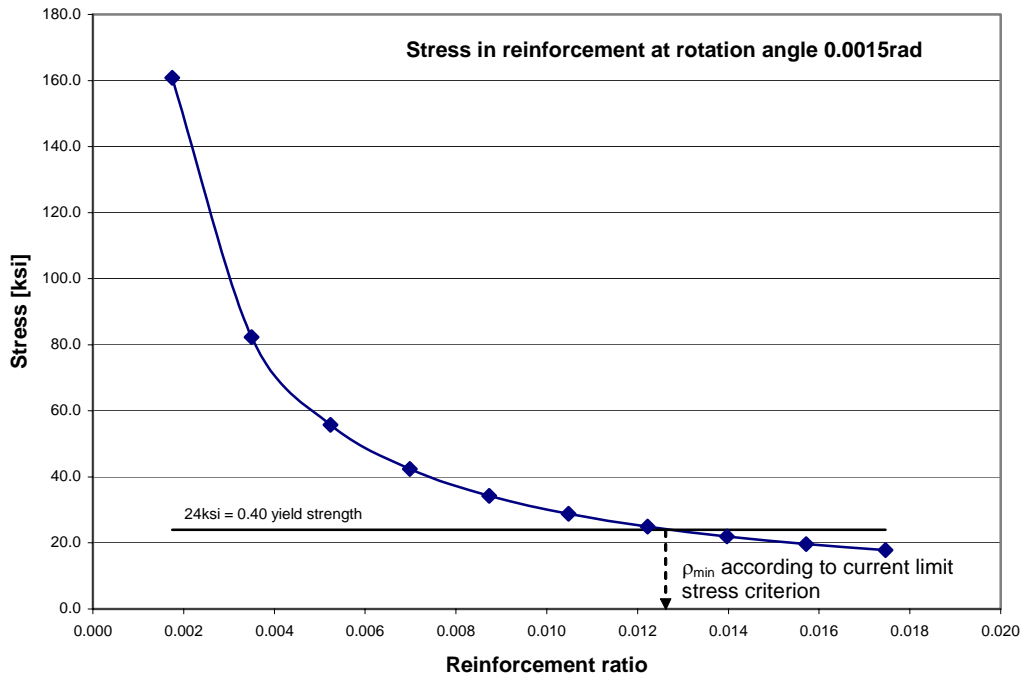


Figure 2.5 Stress in longitudinal reinforcement at expected rotation angle as a function of reinforcement ratio

Step 8 Check surface crack width criterion ($w < w_{max}$)

Besides the stress limit state described above, the current design procedure also limits the maximum crack width at the top of the link slab. The expected crack width is a function of the stress in the reinforcement as determined in Step 7 as well as a function of the geometry of the link slab. The following expression has been adopted from Gergely and Lutz (1968).

$$w = 0.076\beta\sigma_s\sqrt[3]{d_c A} \text{ [0.001 in]}, \quad (\text{Eq. 2-11})$$

with

$$\beta = \frac{H_{ls} - kd}{H_{ls} - d}, \quad (\text{Eq. 2-12})$$

d_c = concrete cover depth [in],

A = effective concrete area per reinforcing bar [in²]

In addition to the crack width criterion adopted in this design guideline (Caner and Zia, 1998), FHWA recommends a minimum reinforcement ratio $\rho=0.015$ with a clear cover of 2.5in for the purpose of controlling the crack width in the link slab.

In essence, the design criteria of this procedure are the stress in the reinforcement σ_s at an expected rotation angle θ and the maximum crack width w_{\max} at the tension face of the link slab.

2.2 Analysis of current design procedure

The derivation of the stress in the reinforcement σ_s as described above is conservative, yet incorrect since the expected applied moment M_a is determined assuming an uncracked link slab, which is consequently relatively stiff and will develop a relatively large moment at a given imposed rotation angle. The link slab is then designed to resist the moment M_a in the cracked condition, however, the reinforcement ratio ρ is chosen for an expected moment M_a in the uncracked condition.

The dependency of link slab deformation and maximum stress experienced within the structural element can be explained as follows (Figure 2.6).

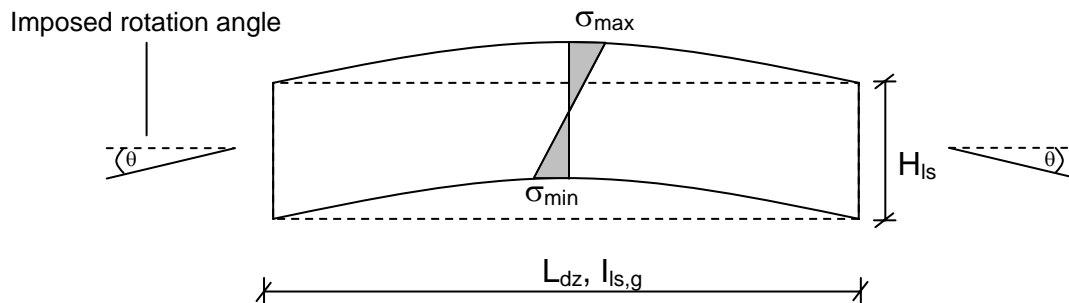


Figure 2.6 Stress state in link slab at imposed rotation angle θ

The moment M_{I_s} developed in the link slab at a given rotation angle θ is dependent on the moment of inertia $I_{I_s,g}$ of the link slab.

$$M_{I_s} = \frac{2E I_{I_s,g}}{L_{dz}} \theta. \quad (\text{Eq. 2-13})$$

The maximum stress in the link slab at a moment M_{I_s} is also a function of $I_{I_s,g}$

$$\sigma_{\max} = \frac{M_{I_s} H_{I_s}}{2I_{I_s,g}}. \quad (\text{Eq. 2-14})$$

Combining these two expressions results in

$$\sigma_{\max} = E \frac{H_{I_s}}{L_{dz}} \theta, \quad (\text{Eq. 2-15})$$

which indicates that the stress in the link slab is independent of the moment of inertia of the link slab with a given height H_{I_s} . This means that a link slab with a high stiffness (large $I_{I_s,g}$) will develop a relatively large moment M_{I_s} at a given rotation angle θ while a link slab with a low stiffness (small $I_{I_s,g}$) will develop a relatively small moment M_{I_s} at the same rotation angle θ . However, the stress in both link slabs is identical at a given rotation angle θ .

This can be further illustrated using an analogous deformation controlled element in tension (Figure 2.7).

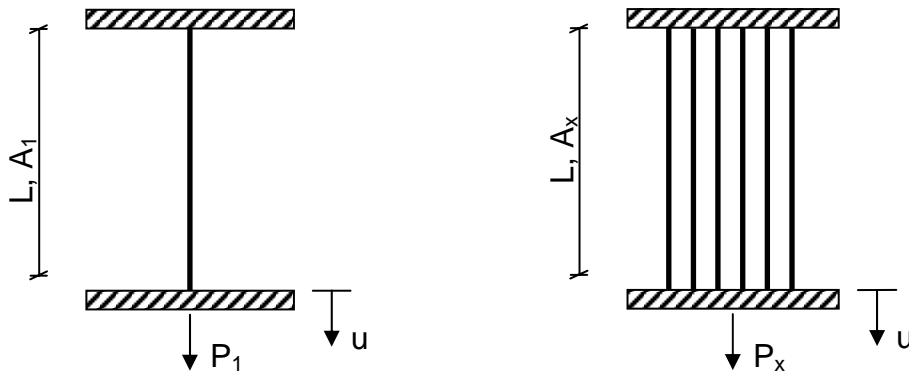


Figure 2.7 Analogous deformation controlled element in tension

Considering a single steel bar fixed at both ends and elongated by a given displacement u , the applied load P to achieve this deformation can be expressed as

$$P_1 = \frac{EA_1}{L} u . \quad (\text{Eq. 2-16})$$

Considering a second configuration with x number of steel bars, the applied load is proportionally higher than that in the case of one reinforcement due to the larger reinforcement ratio ρ of this configuration.

$$P_x = \frac{EA_x}{L} u , \quad (\text{Eq. 2-17})$$

However, the stress in the reinforcement σ in both cases can be determined as

$$\sigma = \frac{P_1}{A_1} = \frac{P_x}{A_x} = E \frac{1}{L} u , \quad (\text{Eq. 2-18})$$

which is independent of the area of the reinforcement A_x , i.e. independent of the reinforcement ratio ρ .

Thus, the stress in the reinforcement σ is not a suitable criterion to determine the reinforcement ratio required in the design of this example configuration as well as in the design of a link slab.

The effect of using the uncracked moment of inertia $I_{Is,g}$ instead of the cracked moment of inertia $I_{Is,cr}$ on the derivation of the moment M_a in the link slab at an expected rotation angle θ_{exp} can be visualized in the following graph (Figure 2.8).

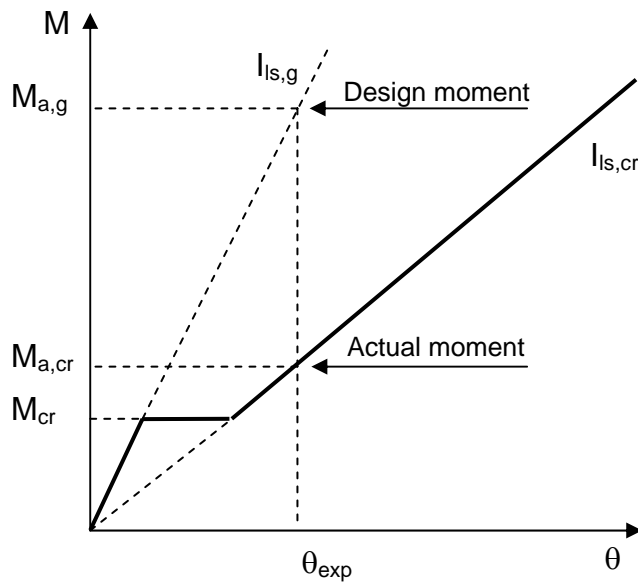


Figure 2.8 Moment rotation relationship of link slab element

By assuming the link slab in an uncracked condition, the design moment M_a at the expected rotation angle θ_{exp} far exceeds the actual moment $M_{a,cr}$ that the link slab develops at this angle in the cracked condition. This leads to an overestimation of the required amount of longitudinal reinforcement in the link slab to satisfy the limit stress criterion.

A more appropriate link slab design guideline is given in Section 9.

3.0 ECC material design

3.1 Property Requirements of ECC for link slabs

For material selection based on the Integrated Structure-Material Design concept (Li and Fischer, 2002), property requirements of ECC material for link slabs were examined prior to material design. A minimum compressive strength of 4,500 psi was adopted on the basis of the compressive strength requirement of concrete in bridge deck slabs (MDOT guideline). Current AASHTO Standard Specifications for Highway Bridges (AASHTO code hereafter) provide a maximum permissible crack width of 0.013” in reinforced concrete bridge decks in severe exposure conditions. The influence of reduced crack width on the permeability of water contaminated by harmful substances, such as chlorides introduced by deicing salt, can be evaluated using reference data (Wang et al, 1997). The data in Figure 3.1 indicate that for crack widths below 0.004”, the permeability coefficient remains relatively small and constant (10^{-9} in./s). At increasing crack widths however, the permeability coefficient increases rapidly and reaches values four orders of magnitudes higher (10^{-5} in./s at 0.013” crack width). Therefore, the desired crack width in ECC was minimized to less than 0.004” to approach transport properties of sound uncracked concrete for corrosion resistance of reinforcements.

Assuming a 5% debond length between deck and girder at the end of each bridge span, of length L_{sp} , as shown in Figure 3.2, the strain capacity (ϵ_{ls}) of the ECC link slab needed to accommodate the movement imposed by a $\Delta T = 90^\circ\text{F}$ temperature variation can be calculated using Eq.3-1. The shrinkage strain, ϵ_{sh} ($\sim 0.1\%$, Section 4), and the maximum tensile strain, ϵ_{LL} ($< 0.1\%$, Section 8), in the link slab due to the imposed

bending moment from the end rotations caused by live loading of adjacent spans are also taken into account.

$$\varepsilon_{ls} = \frac{\alpha_T \cdot \Delta T \cdot 2L_{sp}}{L_{dz}} + \varepsilon_{sh} + \varepsilon_{LL} = \frac{0.0000065 \times 90 \times 2L_{sp}}{0.1 \cdot L_{sp}} + 0.001 + 0.001 \approx 1.37\% \quad (\text{Eq. 3-1})$$

where α_T is the coefficient of thermal expansion of steel. With a safety factor of two, the minimum required tensile strain capacity of ECC material was estimated to be 2.74% for link slab applications. It is worth mentioning that this value is only valid for the worst case, i.e., hinge-roller-roller-hinge support, while for other cases, the tensile strain capacity requirement may be greatly reduced. It is noted that much of the tensile strain capacity demand in Eq. (3-1) comes from temperature induced deformation of the bridge deck.

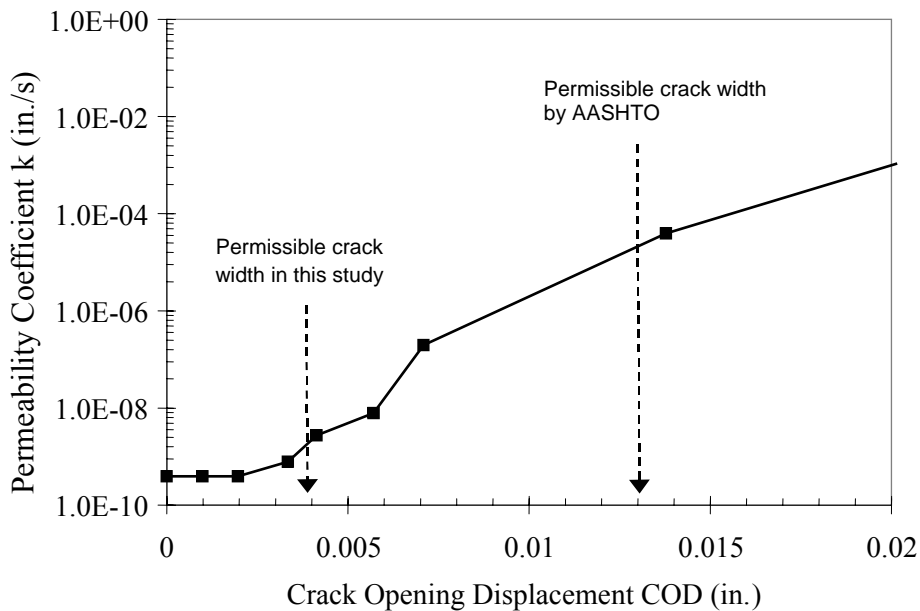


Figure 3.1 Permeability coefficient as a function of crack width.

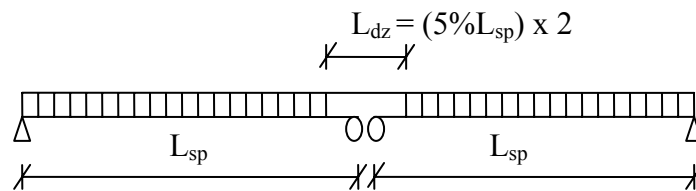


Figure 3.2 Schematic simply supported two span bridge with jointless deck (Assuming hinge-roller-roller-hinge support)

3.2 Freeze-thaw durability consideration on design of ECC

Besides above considerations on property requirement of ECC for link slab, the freeze-thaw durability concern needs to be addressed since this is critical for successful implementation of ECC link slab in Michigan.

The most important factor leading to freeze-thaw resistance in both plain concrete and fiber-reinforced composites is air entrainment. By providing space for freezing water to expand, resistance to freezing and thawing cycles can be dramatically improved. However, the types of air voids provided must be correctly sized and spaced to allow for entrapped water to expand and also permeate out of the matrix when necessary. From numerous studies, and according to ASTM 457-71, the critical spacing for these voids is shown to be less than 0.008". The critical size of the voids, however, can vary. For plain concrete, voids approximately 0.040" in diameter appear to impart good freeze-thaw resistance, however it has been shown that these voids are difficult to produce when using super-plasticized mortar. Litvan (1983), and Cheng-yi and Feldman (1985) found that when using superplasticizer, much smaller air voids ranging from 0.0001" to 0.0008" become critical in maintaining freeze-thaw resistance. Therefore the ECC design criteria focused on forming both large air voids (0.040" diameter) and small air voids (0.0004" diameter).

There are a number of techniques for entraining the desired air voids mentioned above into fiber-reinforced mortars such as ECC. First among these is the addition of fly ash to the mortar (Cheng-yi and Feldman 1985). During mixing and hydration, calcium hydroxide present in the cement accumulates in interface regions surrounding the aggregates and fibers. Fly ash reacts with the calcium hydroxide to create a boundary zone filled with small pores approximately 0.0004" diameter.

A second method for entraining air is using diatomaceous earth or clay as filler in the matrix. Micro-pores present in the clay provide the void spaces necessary for freeze-thaw protection. However, using clay has proven difficult due the tendency of the clay particles to absorb large amounts of mixing water and drastically altering the fresh and hardened properties of the matrix. Finally, introduction of the fiber itself into the mixing process entrains large amounts of air. The mechanical action of the fibers stiffening the fresh mortar allow it to form large air voids and maintain them throughout mixing,

casting, and hydration. Air contents around 15% have been observed when mixing mortar with steel fibers (Pigeon et al., 1996).

3.3 ECC designed for link slab application

Based on the property requirements of ECC material aforementioned, design of ECC has focused on achieving high tensile ductility, good durability and workability. A number of mix proportions were attempted using the above design criteria and are summarized in Table 3.1. Using both fly ash and clay in three of the four initial mixes, an acceptable amount of air entrainment is possible. However, in Mix 31, 32, and 33 the ECC was so viscous that it was difficult to pour. This is likely due to the clay absorbing much of the mixing water resulting in poor flowability and a need for more superplasticizer. Finally, use of clay was abandoned and both the water and superplasticizer were reduced for the initial test mix, Mix 34. Further work on the ECC design for the second round of freeze-thaw testing yielded a further increase in the amount of fly ash to promote formation of small air voids with an accompanying increase of water for both hydration and flowability of the ECC when casting (Mix 45).

Table 3.1 ECC Mix Proportions by Weight

Mix No.	V _f (%)	Cement	Water	Sand	Fly Ash	MC	SP	Clay
M31	2.0	1.0	0.43	0.8	0.5	0.001	0.03	0.1
M32	2.0	1.0	0.48	0.8	0.6	0.001	0.04	0.2
M33	2.0	1.0	0.48	0.8	0.8	0.001	0.04	0.05
M34	2.0	1.0	0.44	1.0	0.8	0.001	0.02	0.0
M45	2.0	1.0	0.53	0.8	1.2	0.0	0.03	0.0

(MC: Methyl Cellulose, SP: Superplasticizer)

Furthermore, a dense microstructure of the particle system was achieved in this study by optimizing the particle size distribution of the composite and maintaining a comparable size distribution of different particles. Particularly, a type F fly ash was chosen due to its comparable size distribution with cement and sand used in the investigation. The particle size distributions of the individual solids used in this study are given in Figure 3.3.

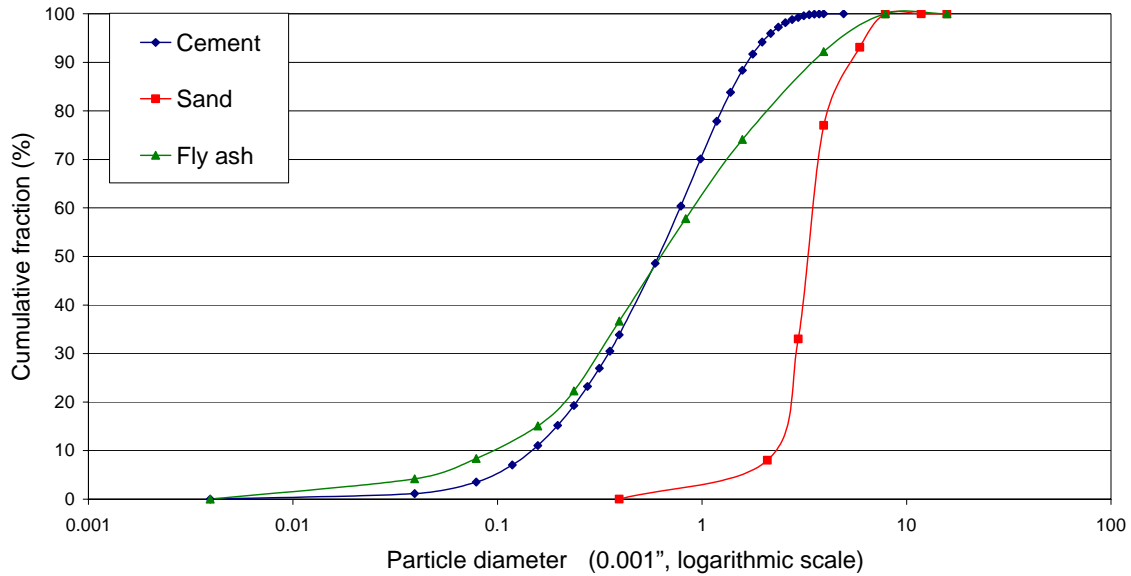


Figure 3.3 Particle size distributions of solids

As shown in Figure 3.4, both ECC proportions used for testing, Mix 34 and Mix 45 exhibited a strain capacity around 3.5% before freeze-thaw exposure (Table 3.2). Therefore, the expected maximum imposed strain (2.74% with a safety factor of two) remains within the strain-hardening regime of these ECCs, with microcrack widths maintained below 0.003". The tensile stress-strain and crack width-strain curves for an ECC M45 specimen is shown in Figure 3.5, where the crack width increases in the initial stage and then remains constant during the steady state cracking stage. Mechanical properties for Mixes 31, 32, and 33 were not determined since these mixes were too difficult to mix and are deemed not suitable. Likewise, these three mixes were not subjected to the extensive freeze-thaw testing regimen (Section 5).

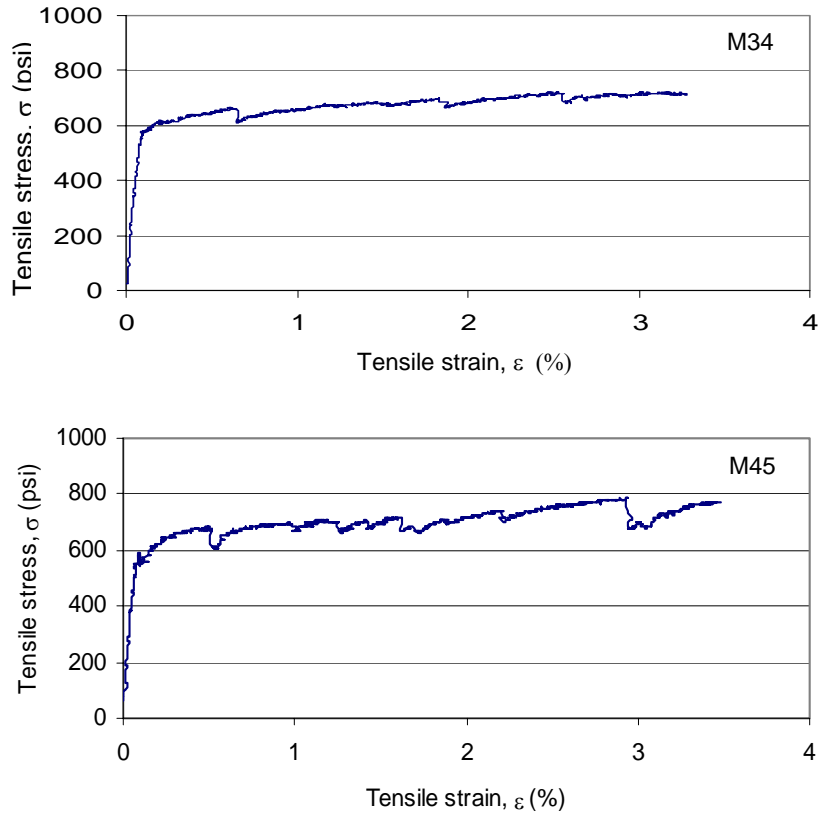


Figure 3.4 Representative tensile stress-strain curves of ECC M34 and M45

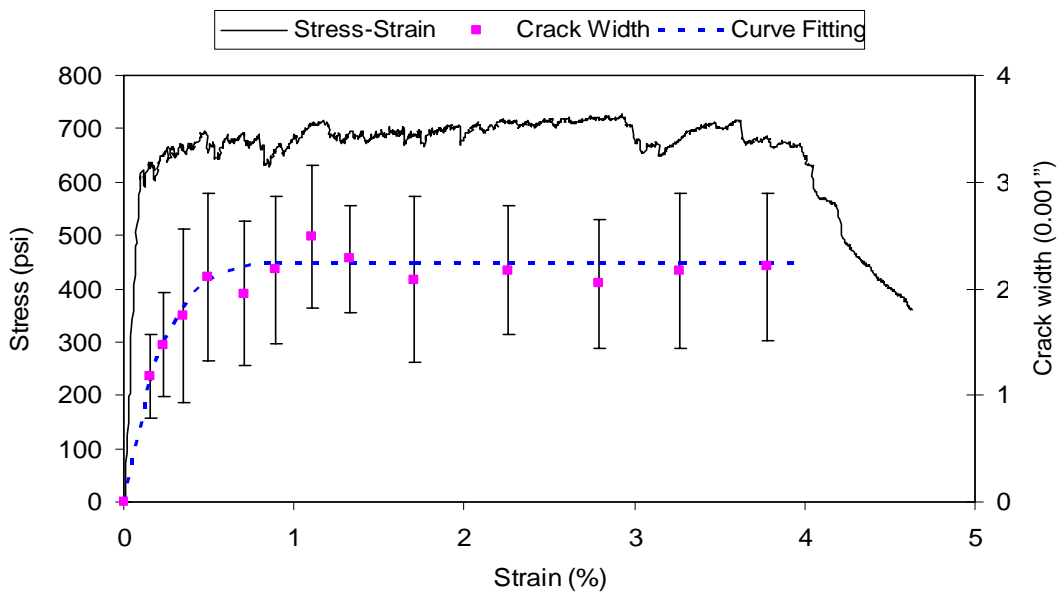


Figure 3.5 Tensile stress-strain and crack width-strain curves for ECC M45.

Table 3.2 PVA-ECC Initial Tensile Test Results

Mix No.	First cracking strength (psi)	Ultimate strength (psi)	Ultimate strain (%)
M31	508 ± 46	653 ± 36	1.2 ± 0.44
M32	450 ± 38	609 ± 22	0.8 ± 0.28
M33	566 ± 45	667 ± 33	1.7 ± 0.39
M34	580 ± 22	725 ± 44	3.6 ± 0.44
M45	580 ± 32	841 ± 54	3.7 ± 0.35

(± means standard deviation of three specimens tested for each mix proportion. Unless otherwise stated, it remains the same throughout the report)

Table 3.3 Mix Proportion of Mix 45 ECC by weight in a cubic yard (Unit: lb/yard³)

Mix	C	W	S	FA	SP	Fiber
M45	983	502	787	1,180	29	44

(C: Type I normal Portland cement produced by LaFarge; W: water; S: silica sands named SILICA SAND F-110 Natural Grain from U.S. Silica co.; FA: a Type F fly ash from Boral Material Technology; SP: Superplasticizer from W.R. Grace & Co. named Daracem ML330; Fiber: a type of poly(vinyl alcohol) fiber (PVA fiber), KURALON K-II REC15, developed by Kurary Co., LTD (Japan) in collaboration with ACE-MRL)

A uniaxial tensile test was carried out to characterize the tensile behavior of ECC. The coupon specimen dimensions used herein were 12”x 3”x 0.5”. Aluminum plates were glued at the end of the coupon specimen to facilitate gripping. Tests were conducted in an MTS machine with a 5.6 kip capacity under displacement control. The loading rate was 0.2mil/s throughout the test. Two external linear variable displacement transducers (LVDTs) were mounted to specimen surface with a gage length approximately 7 inch to measure the displacement. Further test configuration details can be found in the literature (Li et al, 1996).

As shown in Table 3.2, tensile strain capacity of ECC M45 (which was finally chosen as the ECC mix for link slab applications) can meet and exceed the deformation requirement of a link slab. Furthermore, the compressive strength of ECC M45 cured in air is around 8700 psi, well above 4500 psi acceptable for a bridge deck. The mix proportion of M45 by weight in a cubic yard is shown in Table 3.3. In addition to the hardened properties, the mixing process and workability are also critical for practical applications. The fresh properties of M45 were demonstrated in a bridge deck patching project. The ECC was mixed in a 12ft³ capacity drum mixer (Figure 3.6), and then placed into the patch. The ECC patch was hand finished with steel trowels to a smooth surface followed by tining to create transverse grooves in the pavement. It was found

that ECC exhibited excellent workability, eliminating the need for vibration between the reinforcing steel, and moderate finishability as well.



Figure 3.6 Demonstrations of ECC workability in patching of a bridge deck for (a) mixing in a 12ft³ capacity drum mixer; and (b) pouring without any vibration.

3.4 Long term tensile strain capacity

Concerning the long-term strain capacity, uniaxial tensile tests have been used to evaluate the tensile strain capacity of ECC M45 over time. This ECC composite exhibited a strain capacity more than 3% at 28 days, as reported previously. The 3-month and 6-month strain capacity of M45 is slightly lower than the 28-day strain capacity (Figure 3.7 and Figure 3.8), however the observed 3.0% strain capacity remains acceptable for an ECC link slab application. The overall effect of this slight drop in long-term strain capacity is minimal. Based on the test results up to 6 months, the tensile strain capacity seems to stabilize near 3.0% after 28 days.

Table 3.4 Tensile Strain Capacity Development of M45 ECC

Curing time (days)	7	14	18	22	28	98	183
Strain capacity (%)	5.10	4.55	4.20	3.80	3.60	3.50	3.70
	4.40	4.50	3.92	3.50	3.20	2.95	3.10
	4.28	4.06	3.58	3.22	3.00	2.90	1.90*
	4.22	4.10			2.96	2.85	
Average strain capacity (%)	4.50± 0.41	4.30± 0.26	3.90± 0.31	3.51± 0.29	3.19± 0.29	3.05± 0.30	3.40± 0.42

(* indicates premature failure due to alignment problem, excluded from calculation of average strain capacity and standard deviation; ± means standard deviation of the specimens tested at the same age)

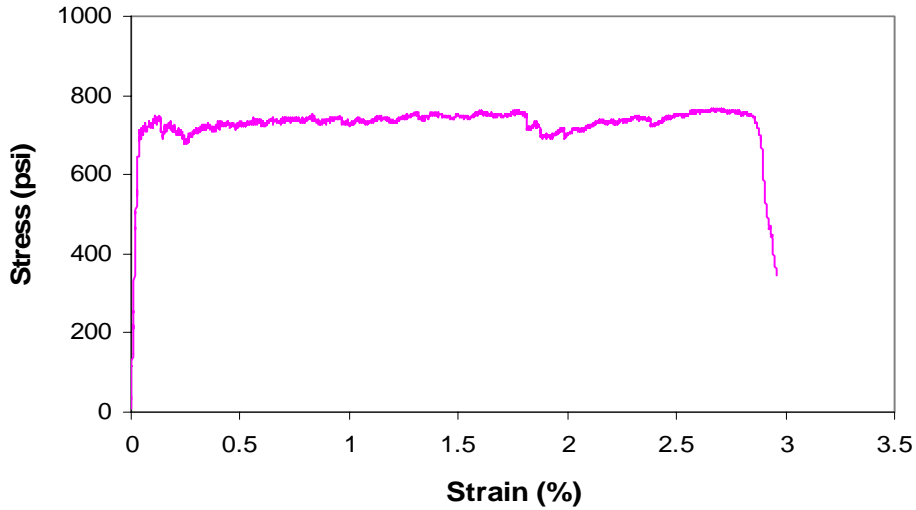


Figure 3.7 Typical stress-strain curve for M45 ECC at 6 months.

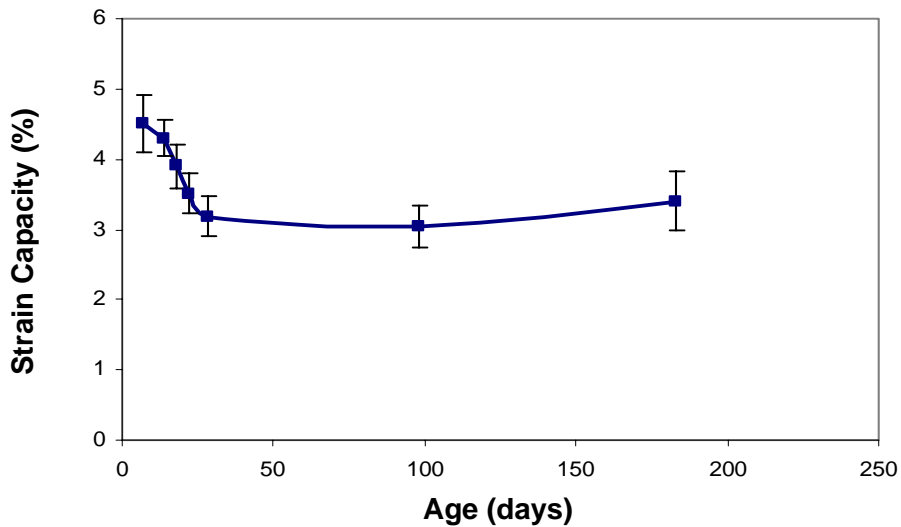


Figure 3.8 Tensile strain capacity development of M45 ECC.

4.0 Shrinkage and shrinkage crack resistance

The investigation of the shrinkage properties of ECC and assessment of cracking due to restrained shrinkage are of interest for the estimation of the shrinkage deformations and the durability of a steel reinforced ECC link slab, which may be subject to aggressive agent (e.g. chlorides) penetration. In this section, first, the free and restrained shrinkage behavior of ECC (M45) were determined and compared to that of a concrete. It is expected that ECC will show higher shrinkage deformation as compared to concrete due to the relatively high total cement and water content. However, due to the

multiple cracking and strain hardening behavior of ECC, it is expected that restrained shrinkage crack widths will be much smaller than that of normal concrete.

Furthermore, the free and restrained shrinkage behavior of ECC produced with a normal Portland cement (from Lafarge Cement) and with a low alkali content Portland cement (from Lafarge Cement, Alpena Michigan) were compared. It can be expected that ECC made with a low alkali content Portland cement (M45 LA) will show lower shrinkage deformation as compared to ECC produced with a normal Portland cement (M45). The explanation for this behavior was published by Beltzung et al. (2001).

4.1 Determination of free shrinkage properties

The investigation of drying shrinkage of ECC (M45) was conducted in accordance to ASTM C157/C157M-99 and ASTM C596-01. Six specimens were cast and demolded after one day. After storage under water for two days the specimens were in equilibrium with 100% relative humidity. After two days of water storage three specimens were stored in a relative humidity of 66% and three specimens were stored in a relative humidity of 33%. The drying shrinkage deformation was measured as a function of drying time until the hygral equilibrium was reached. Figure 4.1 shows the dimensions and test setup of the specimen used to determine the free shrinkage properties of ECC.

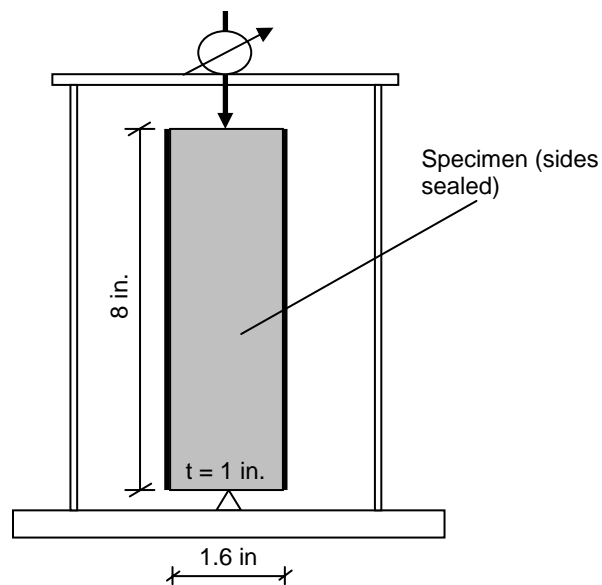


Figure 4.1 Specimen dimensions and test setup

The drying shrinkage was equal to the relative deformation between any R.H and 100% R.H. divided by specimen length at 100% R.H. The measured average drying shrinkage as a function of the relative humidity is plotted in Figure 4.2. In addition to the drying shrinkage of ECC (M45), the drying shrinkage of a concrete control specimen is also shown. The drying shrinkage of the ECC (M45) is found to be approximately twice as high as the drying shrinkage of the investigated concrete. This is due to a total cement and water content per volume of the ECC (M45) twice as high as those in concrete. While the total shrinkage deformation is relatively large (0.15% at 20%R.H.) it should be noted that the average value of the relative humidity in Southeast Michigan is approximately 75%, which corresponds to shrinkage deformations of approximately 0.1%. Figure 4.3 shows the mean annual relative humidity in the U.S.A. (AASHTO, 1996).

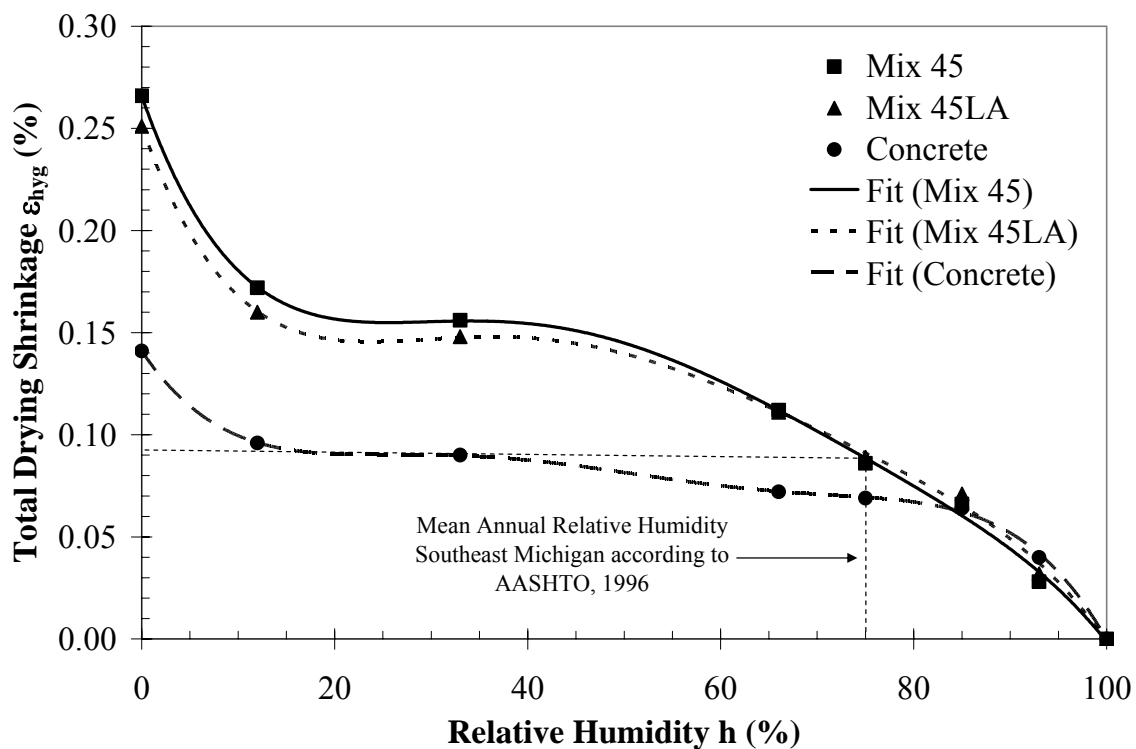


Figure 4.2 Drying shrinkage as a function of relative humidity

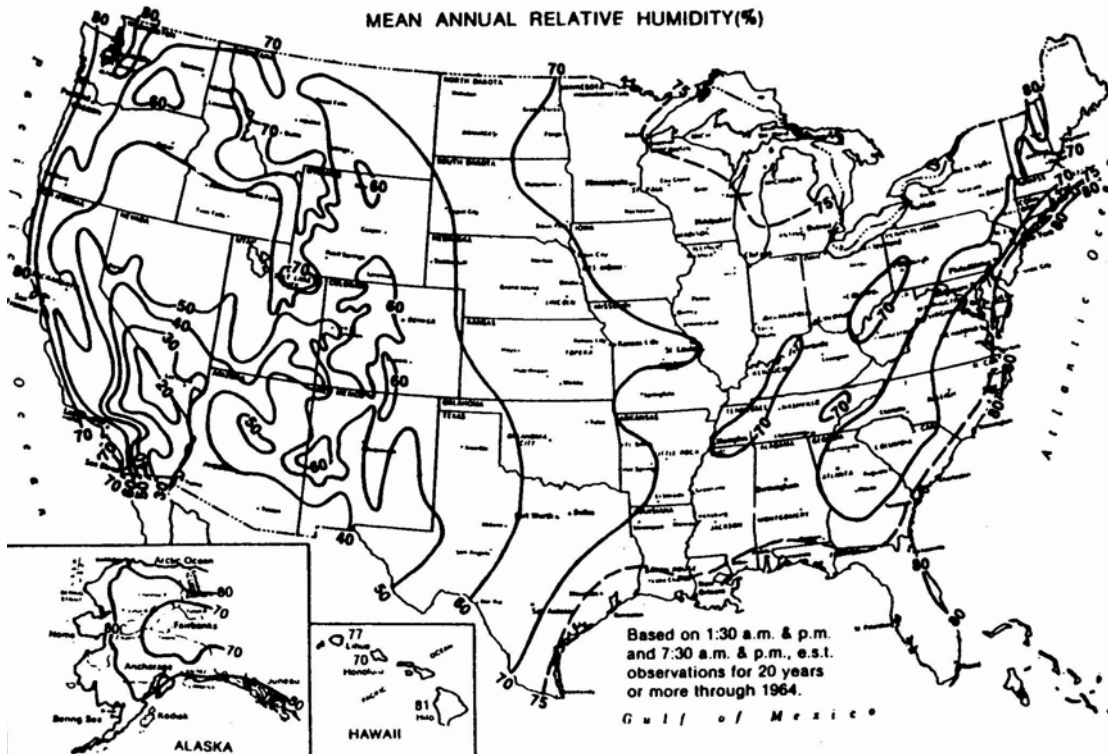


Figure 4.3 Mean annual relative humidity in the U.S.A. (AASHTO, 1996)

To reduce shrinkage deformation, ECC made with a low alkali content Portland cement (M45 LA) was investigated and compared to ECC produced with a normal Portland cement (M45). Same ASTM standards were applied as before. Twenty-one specimens were cast and demolded after one day. After storage under water for two days, the specimens were in equilibrium with 100% relative humidity. Specimens were stored in seven separate containers with relative humidities of 93%, 85%, 75%, 66%, 33%, 12% and 0%. With three specimens in each container, the drying shrinkage deformation was measured as a function of drying time until hygral equilibrium was reached.

The measured drying shrinkage deformation as a function of the relative humidity is plotted in Figure 4.2. The drying shrinkage of ECC produced with a low alkali content Portland cement is similar to the drying shrinkage of the ECC produced with normal Portland cement above 66% relative humidity. At a relative humidity lower than 66%,

the drying shrinkage of M45 LA is slightly lower than M45. The total amount of drying shrinkage of M45 LA is 5% lower compared to M45 at 0% R.H.

At 75% humidity (for Southeast Michigan), the amount of drying shrinkage of M45 LA was similar to that of the normal M45. Thus, the use of a low-alkali cement in ECC to reduce drying shrinkage is unlikely to be an advantage over using ordinary Portland cement. It should be noted that even with the large shrinkage strain in ECC ($\sim 0.1\%$), it remains much smaller than its ultimate tensile strain capacity ($>3.5\%$) at early age. Thus when shrinkage cracks form in ECC, the material will still be in the early strain hardening stage.

4.2 Determination of restrained shrinkage properties

The investigation of restrained shrinkage utilizes a ring test (Shah et al, 1992) (Figure 4.4 and 4.5) to determine the number and width of cracks in the cementitious matrix exposed to 30% relative humidity. First, two specimens of ECC (M45) and two concrete control specimens were compared. Furthermore, two specimens of ECC (M45 LA) were cast for a second round of tests to examine the possible improvement on the shrinkage properties of ECC by using low alkali content cement.

During casting, a plastic covered paper cylinder was used as an outer mold. The outer mold was removed three days after casting. Subsequently, the specimen was exposed to 30% relative humidity. Drying of the specimen leads to an internal radial pressure in the specimen resulting from the restraint of the drying shrinkage deformation provided by the steel ring. Using the dimensions shown in Figure 4.5 it can be shown that the difference between the value of the circumferential stress on the outer and inner surfaces is only 14%. Also the maximum value of the radial stress is only 14% of the maximum circumferential stress. This justifies the assumption that the specimen is subject to a uniaxial tensile stress state when it is restrained from shrinkage deformation by the steel ring.

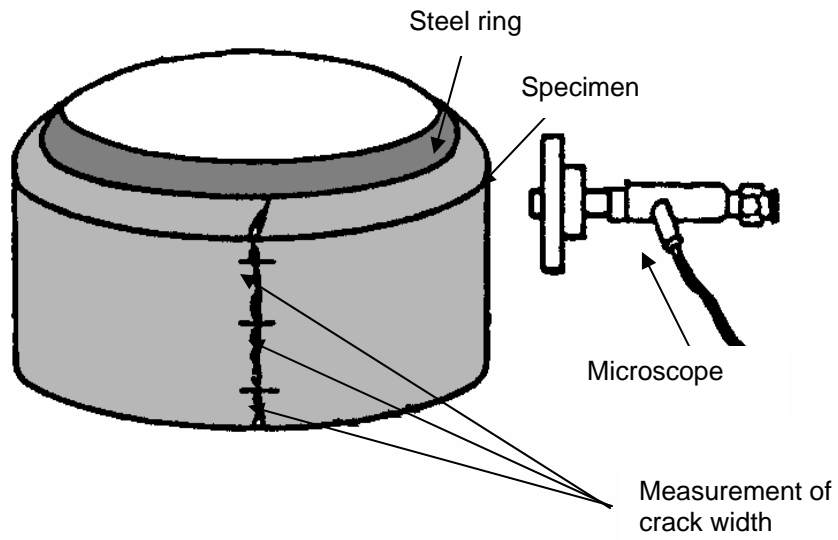


Figure 4.4 Test setup for measurement of the crack width of restrained shrinkage

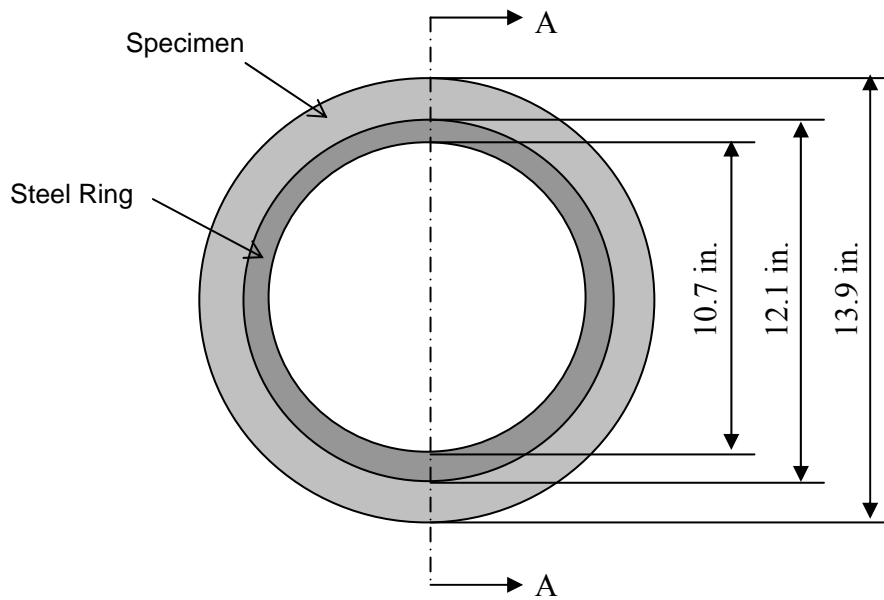


Figure 4.5a Dimension of test specimen (plan view)

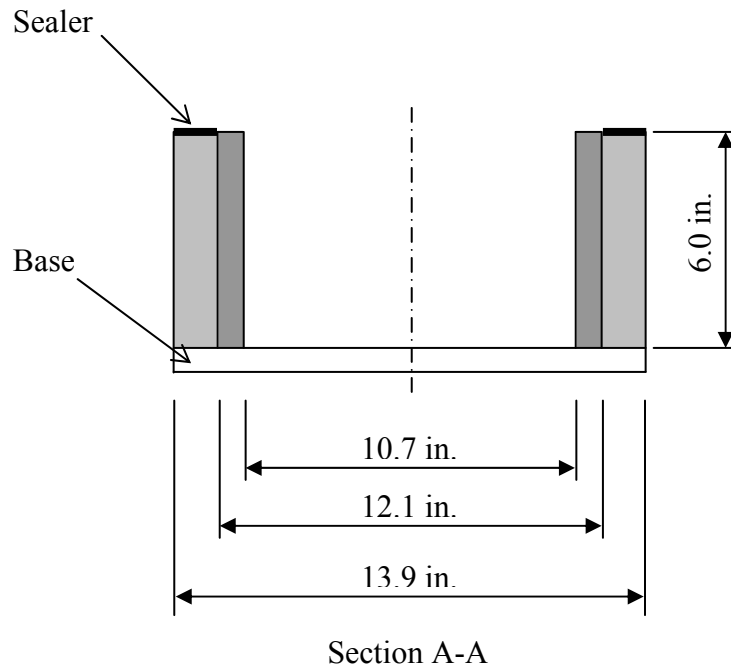


Figure 4.5b Dimension of test specimen (side view section A-A)

The measured crack widths due to drying shrinkage in ECC (M45) and concrete are shown in Figure 4.6. In the concrete control specimen, one crack was formed with an approximate crack width of 0.040". The crack width shown (Figure 4.6) represents the average value of three measurements of the crack width at three different locations of the crack length as shown in Figure 4.4. For the ECC specimen with multiple cracking, the average value of the crack width was taken over the number of cracks and specimen height. In the ECC (M45) specimen, ten cracks were observed. The average crack width observed in the ECC (M45) specimen is relatively small, about 0.003", and is approximately one order of magnitude smaller than that in the concrete specimen. Furthermore, it was found that the average value of crack width measured in M45 LA ECC specimen was similar to the crack width measured in M45 ECC specimen, as shown in Figure 4.6. Thus, the use of a low-alkali cement in ECC to is unlikely to be an advantage over using ordinary Portland cement in terms of restrained shrinkage and crack width.

In terms of durability of an ECC link slab, the influence of reduced crack width on the permeability of harmful substances can be evaluated using reference data (Figure

3.1 and reproduced in Figure 4.7 with expanded scale). The graph shows the dependency of the permeability coefficient as a function of crack width (Wang et al, 1997) in concrete. These data indicate that for crack widths below 0.004" the permeability coefficient remains relatively small and constant (10^{-9} inch/s). At increasing crack widths, however, the permeability coefficient increases rapidly and reaches values several magnitudes higher (10^{-3} inch/s at 0.020" crack width). For the reference concrete with a crack width measured at about 0.040" (Figure 4.6) at steady state, the expected permeability will exceed 1 inch/s. It is expected that the low permeability of ECC due to relatively small crack widths (0.003") will positively affect the durability of an ECC link slab particularly under severe environmental conditions, such as in regions where deicing salts are used.

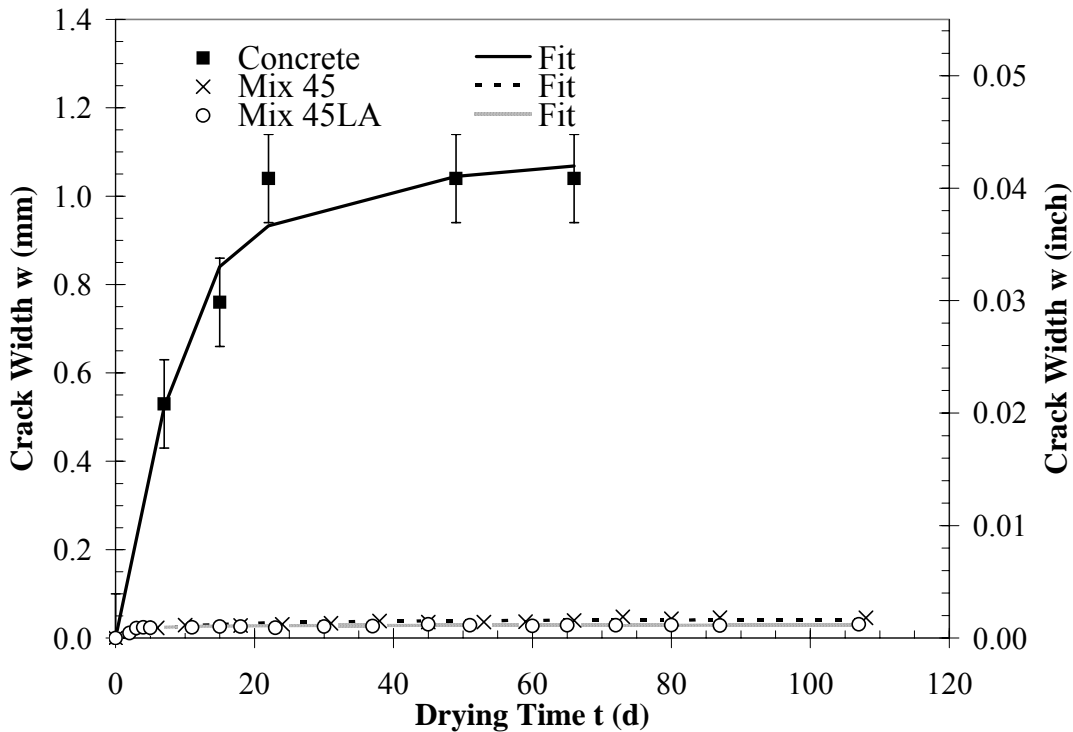


Figure 4.6 Average crack width development over time (obtained from ring tests based on 2 specimens. Crack width measurement made at three points along each crack observed.)

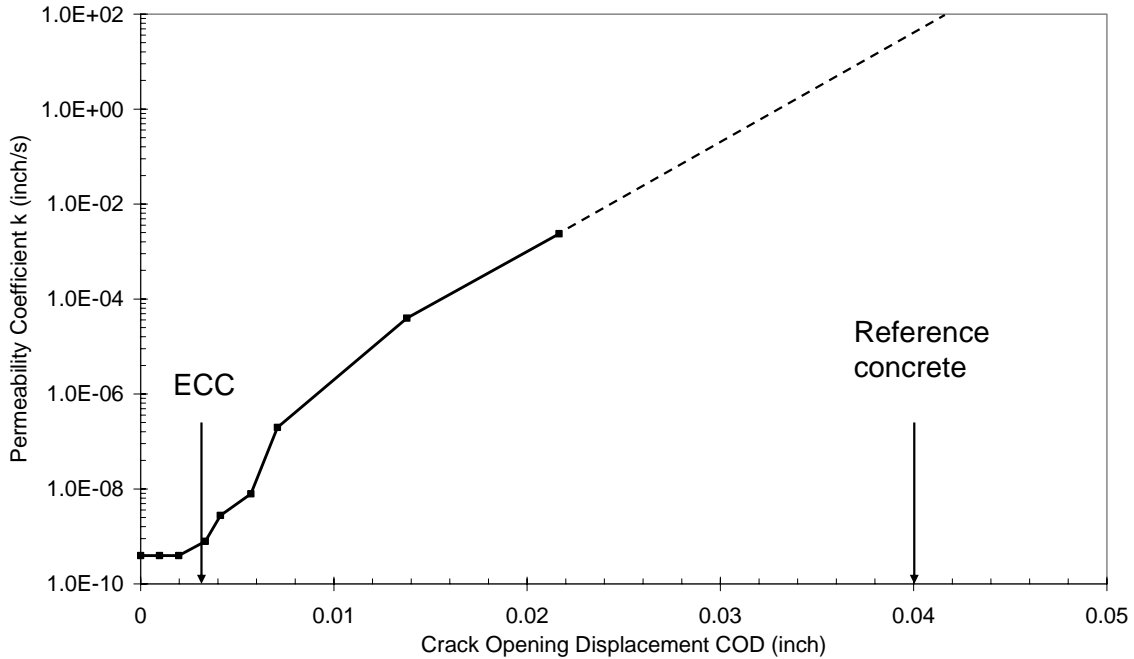


Figure 4.7 Permeability coefficient as a function of crack width (from Wang et al., 1997)

5.0 Freeze-thaw durability

5.1 Pore size distribution

The entrainment of correct size air voids is critical to good freeze-thaw resistance. Methods such as the addition of fly ash, silica fume, and the fibers themselves, have been shown to entrain an adequate size range and number of air voids. Verification of these techniques was carried out through mercury intrusion and porisometry of a standard ECC mix according to standard test specifications (ASTM C-457). The results from this test are summarized in the cumulative pore volume distribution (Figure 5.1). Through the reaction of the added fly ash with calcium hydroxide at the fiber and aggregate interface, a large number of pores in the target range between 0.000014" and 0.00008" have been created. Furthermore, the large porosity value of 21.6% seen from porisometry indicates that a large number of these small pores exist. From this pore distribution, good freeze-thaw protection can be expected from all ECC specimens. Furthermore, porisometry cannot detect voids larger than 0.040" in diameter. The existence of these voids will only further enhance the freeze-thaw durability of the ECC beyond that shown in the pore distribution.

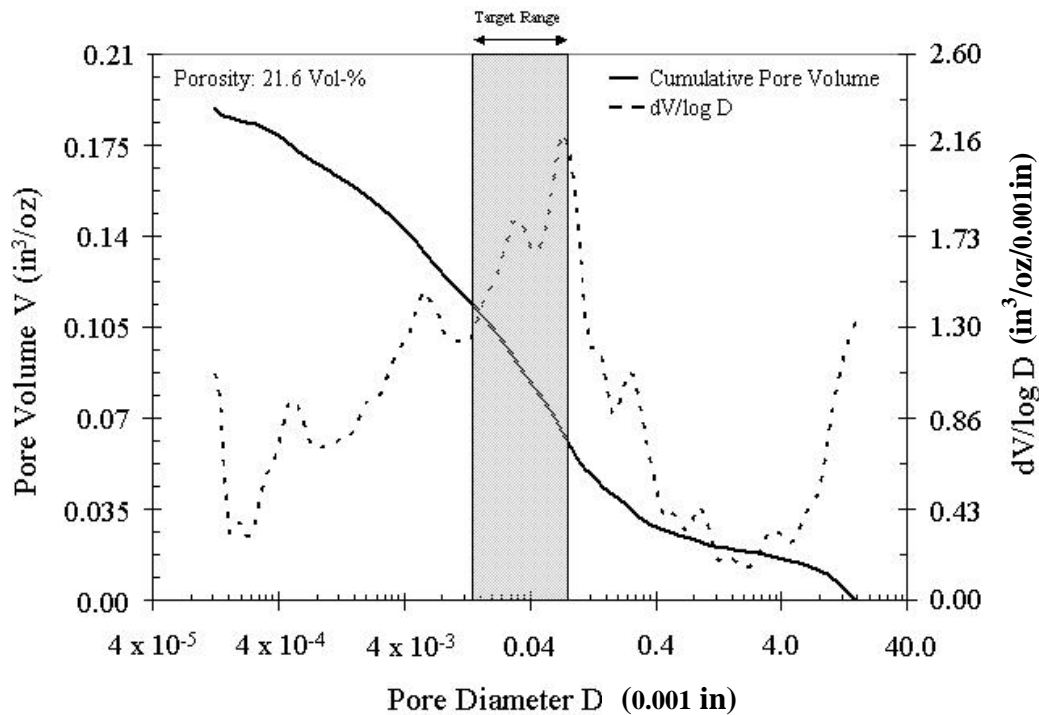


Figure 5.1 ECC pore size distribution

Additionally, the spacing of air voids in the matrix is critical to imparting good freeze-thaw resistance. Using the cumulative distribution curve shown in Figure 5.1 and some simple geometrical assumptions, the average spacing between each micro-pore is found to be approximately 0.000033". This spacing is well below the maximum 0.008" recommended by ASTM. This close spacing is critical for the excellent freeze-thaw resistance of ECC specimens.

5.2 Freeze-thaw exposure testing

Preparation of freeze-thaw and concrete specimens was conducted under ASTM Method C 192 for preparation of laboratory concrete specimens. Four separate test series were conducted. Three series consisted of various ECC mix designs while the fourth was a standard concrete for reference. For consistency, no air entrain was applied in any of the material tested. The three ECC mix designs are designated M34, M45, and M45 LA. Mix proportions for each of these versions are given in Table 5.1. For each series, three prismatic specimens for determination of durability factor and three standard cylinders for compressive strength were subjected to freeze-thaw cycles (carried out at Purdue

University). Additionally, seven ECC tensile test plates in each series were subjected to freeze-thaw cycles in addition to prisms and cylinders. ASTM C666 Procedure A was conducted to test the freezing and thawing durability of prismatic specimens. Dynamic moduli measurements were conducted each week (one week corresponded to approximately 36 cycles of freezing and thawing). The flexural resonant frequency was obtained by using Grindstone Resonant Frequency equipment. The dynamic modulus was calculated based on the procedure described in ASTM C 215. Overall test results indicate that ECC provides superior resistance to deterioration subjected to freeze-thaw cycles when compared to standard concrete.

Table 5.1 ECC and Reference Concrete Mix Designs (lb/yd³)

Mix No.	Cement	Gravel	Sand	Fly Ash	Water	Superplaticizer	MC	PVA Fiber
M34	1370	0.0	1370	150	584	27.3	1.37	43.8
M45	945	0.0	757	1134	551	23.6	0.0	43.8
M45 LA	945*	0.0	757	1134	551	23.6	0.0	43.8
Concrete	728	1456	1456	0.0	324	7.25	0.0	0.0

(* Denotes the use of low alkali cement, MC: Methyl Cellulose)

For each ECC specimen subjected to freeze-thaw cycles the dynamic modulus remained nearly constant or increased while the dynamic modulus of the regular concrete dropped dramatically (Figure 5.2). The three rounds of freeze-thaw testing show an average durability factor over 100 for M34 ECC samples and an average durability factor of 20 for the concrete samples. Furthermore, the regular non-air-entrained concrete samples failed after only 110 of the 300 recommended freeze-thaw cycles while the ECC specimens survived all 300 test cycles. Similar to M34, M45 specimens subjected to freeze-thaw cycles exhibited a constant or slight increase in dynamic modulus when compared to regular concrete (Figure 5.2). Also similar to M34, the average durability factor of M45 ECC is 104, far above the concrete durability factor.

Unlike previous results, M45LA specimens subjected to freeze thaw cycles exhibited an increase in dynamic modulus while undergoing freeze thaw exposure (Figure 5.2). While the relative dynamic modulus of M45 after 300 freeze-thaw cycles increased only 3%, the relative dynamic modulus of M45LA increased approximately

20%, showing a substantial change. However, this increase is in accordance with the companion M45LA ECC specimens cured in a fog room, which showed an analogous increase. According to ASTM freeze thaw testing procedures, freeze-thaw exposure begins 14 days after specimens are cast. While all other specimens were tested in this manner, due to testing machine availability, freeze thaw cycles for M45LA ECC specimens commenced 11 days after casting. The increase in dynamic modulus of M45LA ECC during the early portion of freeze-thaw exposure may be partially credited to the early start of testing, but may more likely be due to a slightly different hydration rate of low alkali content cement when compared with normal Portland cement quarried and ground at different manufacturing facilities.

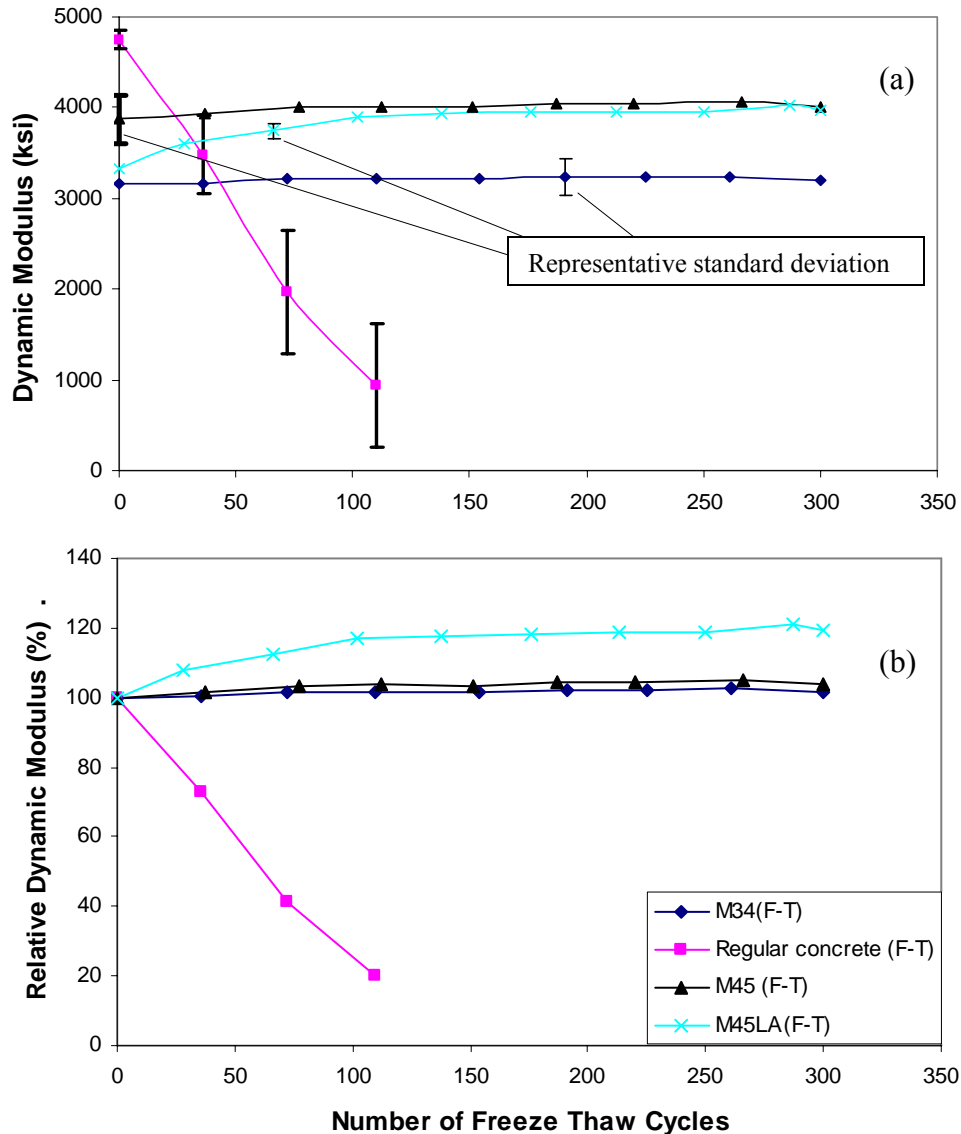


Figure 5.2 Freeze-Thaw test results showing (a) dynamic modulus, and (b) relative dynamic modulus

The mass loss experienced by the ECC freeze-thaw specimens was less than the mass loss from the regular concrete samples. Each ECC prism subjected to freeze-thaw conditions lost an average of 0.9% of initial mass over 300 cycles while the concrete specimens lost an average of 2.0% of initial mass after completing only 110 cycles. A number of regular concrete cylinder specimens were left exposed to freeze-thaw conditions after 110 cycles but were reduced to loose aggregates by 144 cycles. Photographs of ECC specimens and regular concrete specimens are shown below (Figure 5.3-5.6).

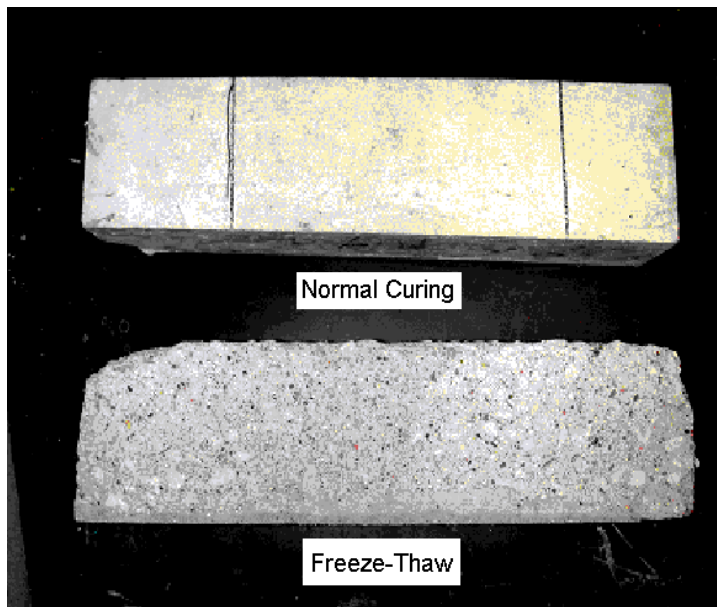


Figure 5.3 Regular Concrete Normal Curing and Freeze-Thaw Specimens



Figure 5.4. M34 ECC Normal Curing and Freeze-Thaw Specimens

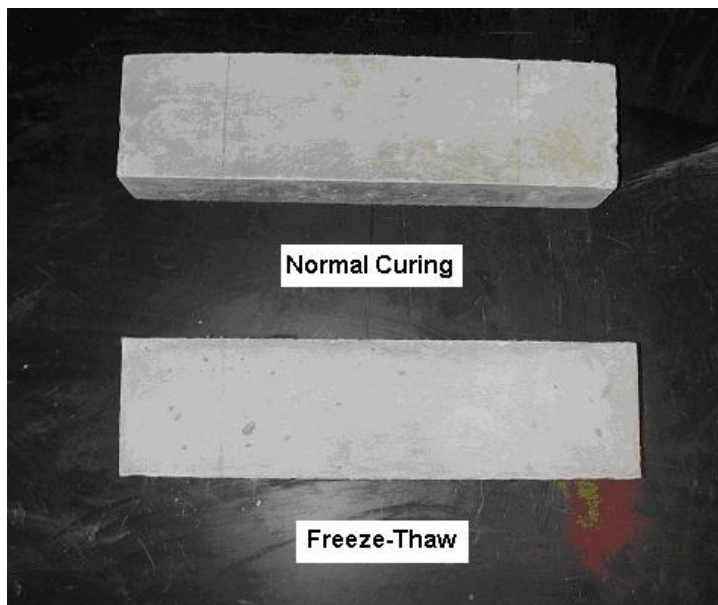


Figure 5.5 M45 ECC Normal Curing and Freeze-Thaw Specimens

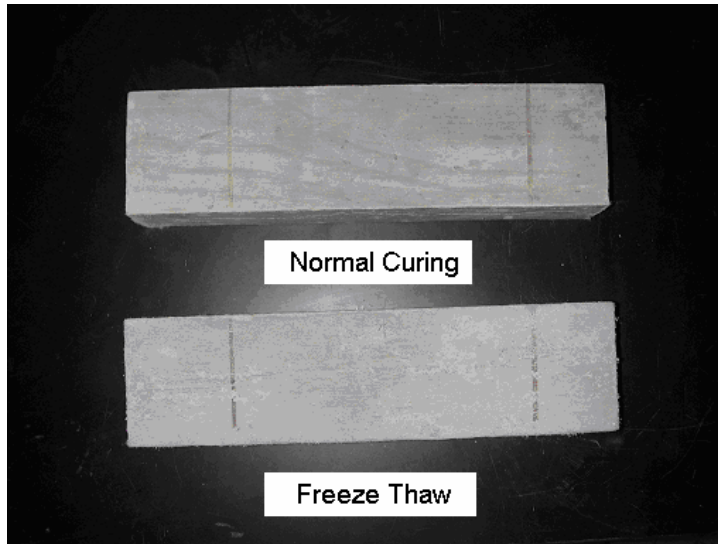


Figure 5.6 M45LA ECC normal curing and Freeze-Thaw specimens

5.3 Tensile testing of freeze thaw specimens

After undergoing 300 freeze-thaw cycles in a 14 weeks test, the ECC specimens retain much of their initial tensile ductility. For each mix tested, all tensile specimens subjected to freeze-thaw show an average ultimate strain capacity over 2.0%, with most nearing 3.0%. This is close to the 2.5% - 3.0% strain capacity seen from specimens of the same age not subjected to freeze-thaw conditions. Typical tensile stress-strain curves are shown in Figure 5.7 and Table 5.2 for M34, M45, and M45LA for both normal cured and freeze thaw tensile specimens. From this, it is seen that freeze-thaw exposure has little effect on the tensile performance of ECC material. Furthermore, the strain capacity seen in these freeze thaw specimens remains acceptable for the ECC link slab application.

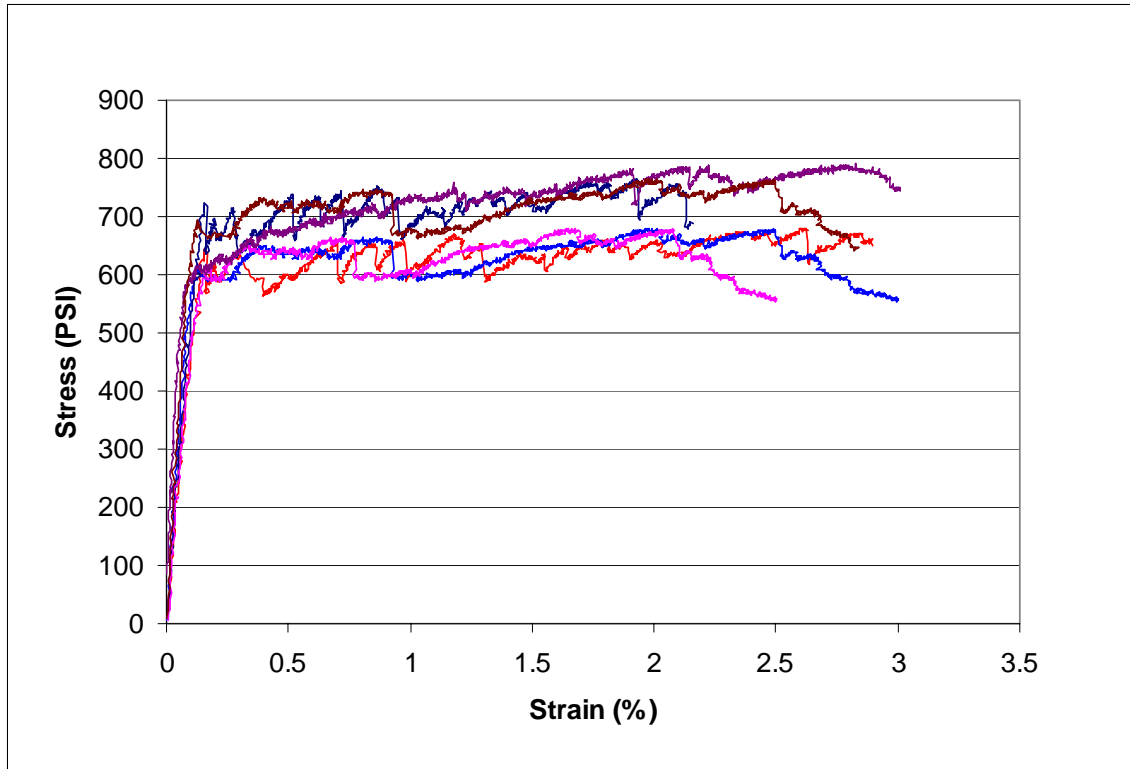


Figure 5.7 Stress-Strain Curve for ECC Normal Curing and Freeze-Thaw Specimens

Table 5.2. Freeze-Thaw Tensile Test Results (Based on 3 test specimens per mix)

Mix No.	First Cracking Strength (PSI)	Ultimate Strength (PSI)	Ultimate Strain (%)
34 NC*	650 ± 60	710 ± 100	2.5 ± 0.23
34FT**	630 ± 30	740 ± 50	2.1 ± 0.34
45NC*	580 ± 30	800 ± 110	3.0 ± 0.52
45FT**	580 ± 50	740 ± 70	2.8 ± 0.60
45LA NC*	620 ± 50	680 ± 40	2.9 ± 0.4
45LA FT**	670 ± 30	680 ± 60	2.8 ± 0.9

*Indicates Normal Curing Samples, age= 14 weeks

**Indicates Freeze-Thaw Samples, age= 14 weeks

5.4 Compression testing of freeze-thaw specimens

Along with prisms and tensile plates, three 3" x 6" compressive cylinders were also subjected to freeze-thaw conditions. Upon completion of 300 freeze thaw cycles, three cylinders were tested using a Satec testing machine based on ASTM C39 procedure (conducted at Purdue University). In addition to the freeze-thaw cylinders, companion specimens cured in a fog room were also tested at the same age. M45 and M45LA ECC

compressive strengths for specimens subjected to freeze-thaw conditions and fog room curing are shown in Table 5.3. Due to testing problems, compressive strengths were not obtained for Mix 34 specimens. The appearance of Mix 45LA cylinders subjected to compression testing after both freeze-thaw exposure and fog room curing are shown in Figure 5.8. As seen from this figure, the failure mode for both of these specimens seems quite similar from outward appearance.

Table 5.3 Freeze-thaw and fog room curing compressive strength

Mix No.	Curing Condition	Average Compressive Strength (PSI)
M45	Fog Room Curing	11600 ± 300
	Freeze Thaw	8800 ± 300
M45LA	Fog Room Curing	9100 ± 300
	Freeze Thaw	5700 ± 200

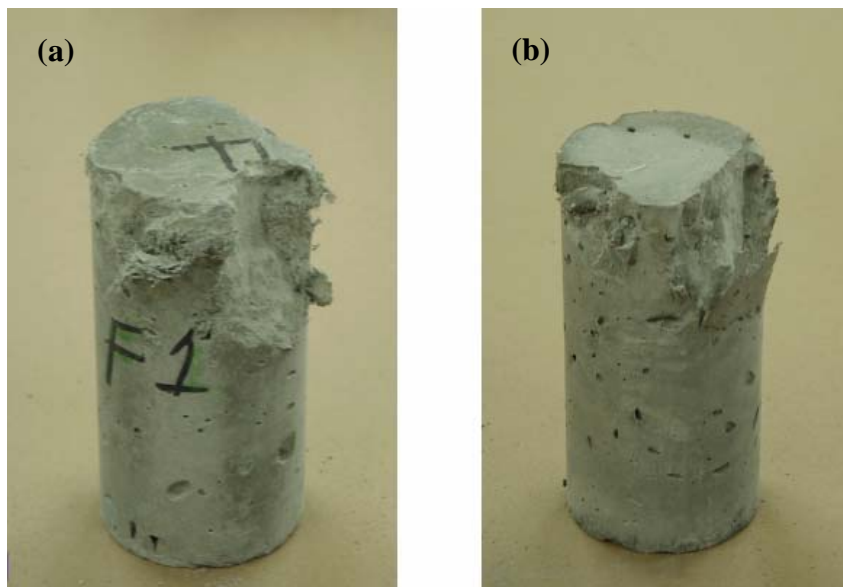


Figure 5.8 Comparison between (a) M45LA Freeze-thaw specimen: and (b) M45LA fog room curing specimen after compression testing

The compressive strength for M45 ECC is well above minimum requirements for bridge deck applications both before and after freeze thaw testing. The same is true for M45LA ECC. Specimens of M45 ECC exhibited compressive strengths of 11,600 psi and 8,800 psi after fog room curing and freeze thaw exposure, respectively. Analogously, specimens of M45LA ECC cured in a fog room showed an average compressive strength of 9,100 psi and 5,700 psi when exposed to freeze-thaw cycles. As mentioned above,

while the compressive strength is lower after freeze-thaw exposure, the compressive strength for both ECC mixes after freeze thaw cycles is still well above the 4,500 psi recommendation by MDOT for minimum compressive strength of bridge deck material.

While the compressive strength is adequate, the 24% difference in compressive strength for M45 ECC and 38% difference for M45LA ECC, both between fog room curing and freeze thaw condition, is a source of concern. A number of mechanisms may be at work affecting the compressive strength of the freeze-thaw exposed ECC specimens. As seen in Figure 5.8, compressive failures are primarily at specimen ends, which may be the cause of the premature failure and low compressive strength test results. In this case, dynamic modulus measurements should be used to evaluate the condition of the material as a whole. Dynamic modulus data discussed earlier show excellent durability of the entire prism specimens throughout the entire freeze thaw test.

Another likely reason for the lower compressive strength of freeze thaw ECC is the difference in maturity between specimens subjected to freeze-thaw conditions and specimens stored in a fog room. Maturity is calculated using the Nurse-Saul equation.

$$\text{Maturity } (^{\circ}\text{F} \cdot \text{days}) = \sum [a_t (T + 50)] \quad (\text{Eq. 2-1})$$

where a_t is time of curing in days and T is curing temperature in $^{\circ}\text{F}$. The maturity of ECC specimens after fog curing is approximately $8600^{\circ}\text{F} \cdot \text{days}$ while the maturity of ECC specimens after freeze thaw is $5700^{\circ}\text{F} \cdot \text{days}$. This significant difference in maturity levels would result in a significant difference in compressive strength of ECC material. Figure 5.9 exhibits the relation between concrete compressive strength gain and maturity. From this relationship, the fog room specimens are expected to exhibit 100% of potential compressive strength. However, the freeze thaw specimens are expected to exhibit about 90% of the potential compressive strength. While this only accounts for a portion of the difference between freeze thaw and fog room specimens, maturity differences most likely have a significant effect on the lower compressive strength of the freeze thaw ECC cylinders.

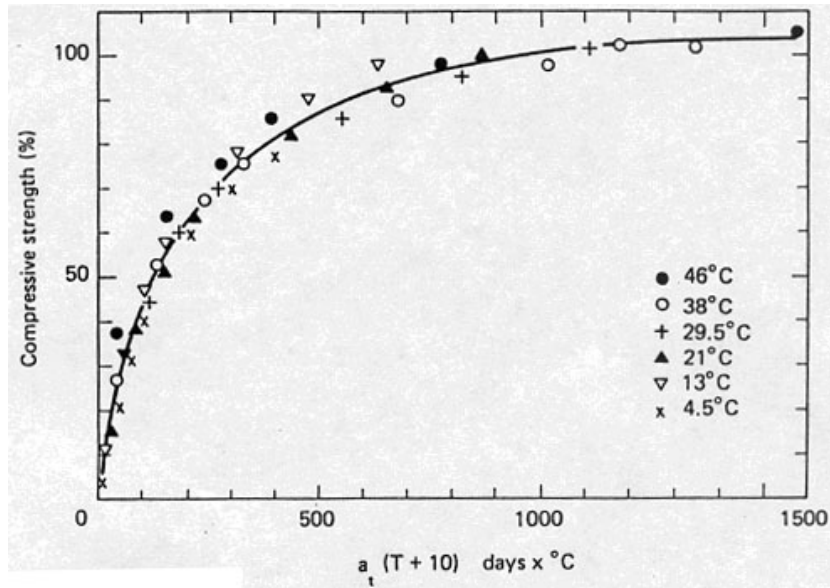


Figure 5.9 Concrete compressive strength vs. maturity (Mindess, 1981)

While relatively few studies have focused on the compressive strength of concrete after freeze thaw exposure, previous work does show, with varying magnitudes, that concrete regularly exhibits a lower compressive strength after freeze-thaw exposure. Toutanji and Deng (2002) found that FRP wrapped concrete cylinders showed lower compressive strength after freeze-thaw exposure. Cylinders cured in normal conditions showed a strength of 21,825 psi compared to freeze thaw cylinders with showed a compressive strength of 20,100 psi, a difference of 8% drop in compressive strength. Unwrapped cylinders were also tested by Toutanji and Deng, but these specimens did not survive freeze-thaw exposure. Toutanji and Balaguru (1999) found a 28% lower strength in GFRP wrapped concrete cylinders when exposed to freeze thaw cycles. Finally, Soudki and Green (1997) experienced a 48% difference in compressive strength from 7,300 psi to 3,900 psi after freeze-thaw exposure of unwrapped plain concrete cylinders. While the reduction in compressive strength of ECC after freeze-thaw exposure is substantial, a similar phenomenon has been documented in concrete.

After 300 freeze-thaw cycles, M45LA ECC exhibits a substantial increase in dynamic modulus, a high durability factor, and no significant change in tensile strain capacity. However, a 38% reduction in compressive strength is significantly larger than the 23% reduction in compressive strength seen in M45 ECC. The use of low alkali content cement exhibits no improvement in freeze thaw durability, but reveals a

substantial drop in compressive strength after freeze thaw exposure when compared to normal Portland cement, at the same age. As a result of these findings, the replacement of normal Portland cement with low alkali content cement in ECC is not suggested for this project. While the use of low alkali content cement may be beneficial in some normal concrete applications, its benefits in ECC applications are minimal and not extensive enough to promote replacement of normal Portland cement.

6.0 Design of ECC link slab/concrete deck slab interface

6.1 Conventional and improved interface design methods

In this project, ECC link slab is used to accommodate bridge deck deformations, replacing typical expansion joint. However, the interface between ECC and concrete may become a weak link due to cold jointing and load transfer between the existing concrete and link slab. This has been demonstrated by MDOT in a preliminary laboratory investigation. During monotonic test to failure on their specimen 1C, the interfacial crack grew noticeably while the width of cracks in the ECC link slab was maintained below 0.002”.

Previous experiments suggested that the bond strength between concrete and ECC (hot joint: both materials are cast at the same time) is roughly 0.3 ksi (Zhang and Li, 2002). In the current project, the interface is cold jointed when an ECC link slab is used for the replacement of an expansion joint, meaning that the bond strength could be considerably lower than that of a hot joint. Methods to strengthen the interface between concrete and ECC and design approaches to reduce stress concentrations at the interface are of major concern for interface design.

The existing design procedure for concrete link slabs does not give enough attention to the design of the deck slab/link slab interface. In conventional concrete link slab design, additional reinforcement is spliced with the existing reinforcement to strengthen the link slab. However these reinforcements typically end at the interface. Additionally, the debond zone (part of the link slab is deliberately debonded from the steel girder to provide additional flexibility to the link slab) begins at the interface (Figure 6.1a). This imposes high stress concentration at the interface. Overall, this design procedure makes the interface the weakest part of the bridge deck system.

In order to strengthen the interface, various methods may be applied such as using continuous longitudinal reinforcement through the interface, installing shear studs, or additional concrete surface preparation. In the proposed design of ECC link slabs, shear studs connecting the steel girder and the deck are extended to within the ECC link slab; therefore the debond zone begins at the end of the lap splice (Figure 6.1b). It is also expected that the stress developed at the interface will be much lower than that of conventionally designed link slabs while at the same time the interface will be strengthened by using the methods aforementioned. Numerical structural analysis (Section 6.2) demonstrates the advantage of improved interface design of an ECC link slab.

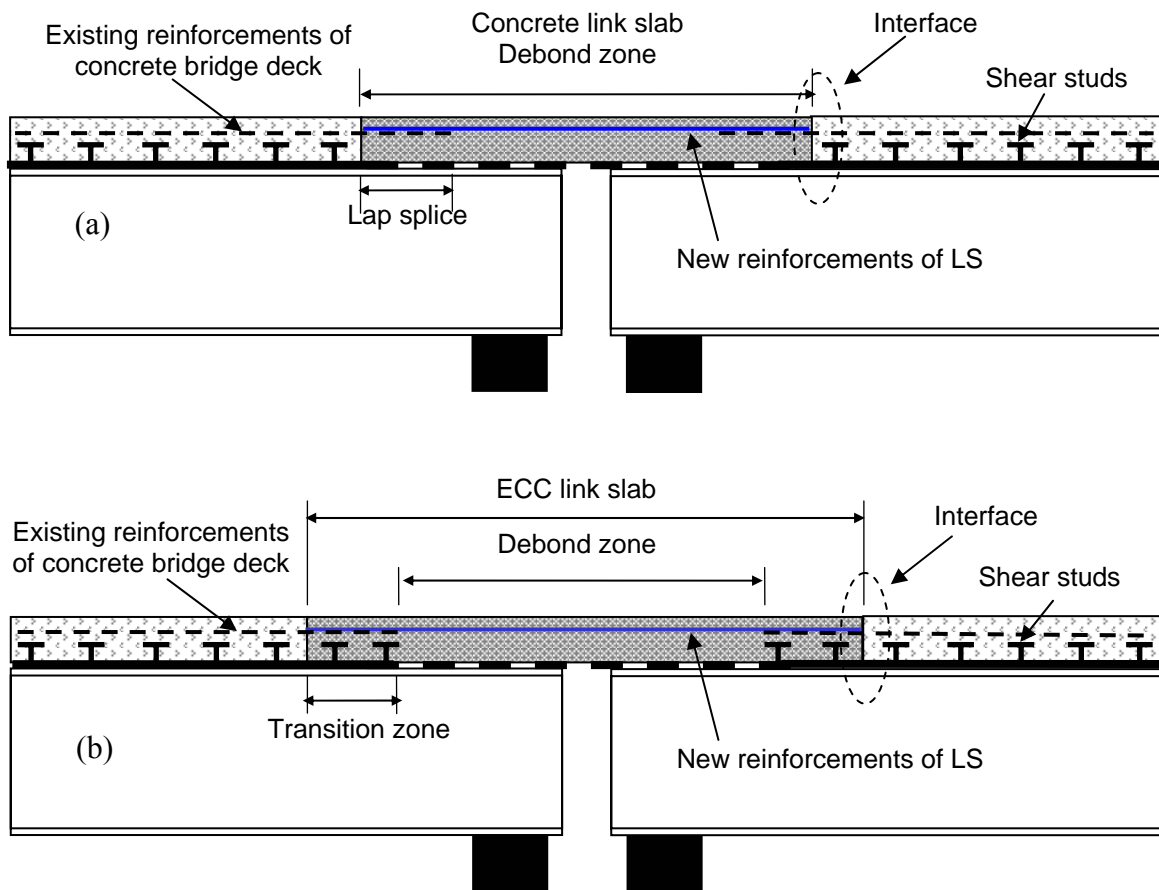


Figure 6.1 Comparison of schematic interface design in LS between (a) conventional method and (b) improved method

6.2 Analysis of Bridge Model

Structural analysis software (RISA) is used to model a simply supported two-span bridge to determine the critical stress induced by a standard AASHTO HS-20 load available in RISA. By applying a moving load, the envelope solution is obtained for the maximum stress state such that both the top and bottom surface have maximum tensile or compressive stress. Both the improved design and conventional link slab design approaches described above (Section 6.1) are modeled and analyzed for comparison.

For simplicity, a general-purpose beam element is used to model both the girder and bridge deck. Furthermore, an infinitely rigid link is used to model the composite action provided by the shear stud between girder and bridge deck. This rigid link has infinite moment of inertia and infinite elastic modulus while the density is zero. Besides this rigid link, other materials defined in this model are steel, concrete, and ECC with elastic moduli of 29000 ksi, 4348 ksi, and 2173 ksi respectively. The thickness and width of link slab are 9” and 63” respectively. The I section used is W24X117.

Both of the adjacent spans modeled are 65.6 feet in length with a debond length of 3.3 feet for each span. Two shear studs (modeled by rigid link) penetrate into the ECC link slab. The distance between shear studs is chosen as 1.64 feet according to AASHTO Standard Specifications for Highway Bridges (AASHTO, 1996). Details of the structural model of the link slab and adjacent parts are shown below (Figure 6.2), where M1 means the concrete deck slab adjacent to the interface and M2 is debond zone of ECC link slab. The corresponding physical model is shown in Figure 6.1b. Since the support condition has a large influence on the analysis results (Caner and Zia, 1998), two typical types of supports are used in the analysis. These include the hinge-roller-roller-hinge condition (HRRH), and the hinge-roller-hinge-roller (HRHR) condition.

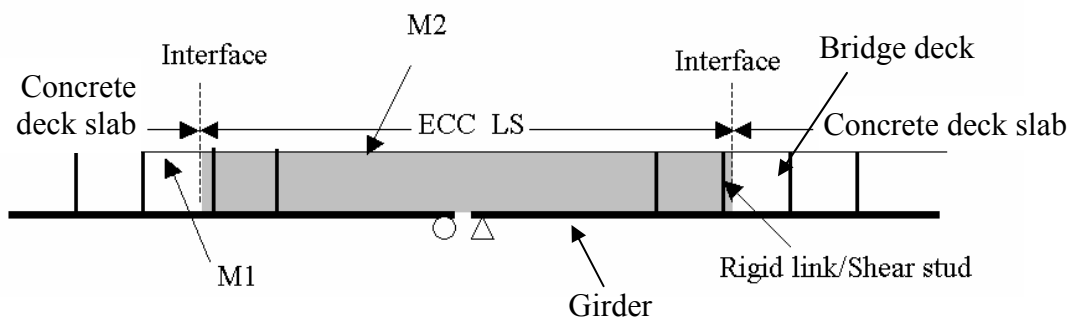


Figure 6.2 Model of the bridge (close look at the link slab)

From the analysis results, member M1 is found to be always subjected to compressive stress (less than 218 psi for all sections) for the HRRH type support, while the debond zone of ECC link slab (M2) is in bending with a maximum tensile stress of 725 psi at the top surface. This means that the deck slab/link slab interface will always be subjected to compressive stress. Hence this type of support does not govern the design of the interface.

For the HRHR type support, member M1 is in tension while member M2 is in bending. The maximum tensile stresses for M1 and M2 are 183 psi and 943 psi, respectively, at the top surface. Therefore, the HRHR type support governs the design of the interface and forces the interface test design to focus on tension rather than bending. Due to the limitation of the RISA (name of commercial structural analysis software), the unique strain hardening behavior cannot be represented in the material model. The linear elastic behavior was “assumed” for ECC. Therefore, in reality, the member M2 should have entered strain hardening stage with a yielding stress of around 580 psi instead of a maximum tensile stress 943 psi.

After analyzing the improved design, the additional shear studs (rigid link in the model) are removed and the analysis for conventional design is performed. Figure 6.3 shows the normalized maximum tensile stresses of the members near the interface for both conventional and improved design (Normalized by the maximum tensile stress of the improved interface design at the interface location). All stresses are on the top surface of the section since these are of major interest. It is found that the maximum tensile stress of the improved interface design at the interface location was only one fifth of that of the conventional design due to the extension of shear studs into the ECC link slab. The additional shear studs shift the peak stress value from the interface to the bulk part of the link slab, which has higher strength and enough strain capacity to accommodate this stress. Therefore, the interface of improved design will perform much better than that of conventional design. Furthermore, with the help of longitudinal reinforcement on the interface, which is not considered in the current model, removal of the potential weakness at the deck slab/link slab interface seems assured. The integrity of the joint will also be demonstrated as a part of the full-scale link slab test (Section 8).

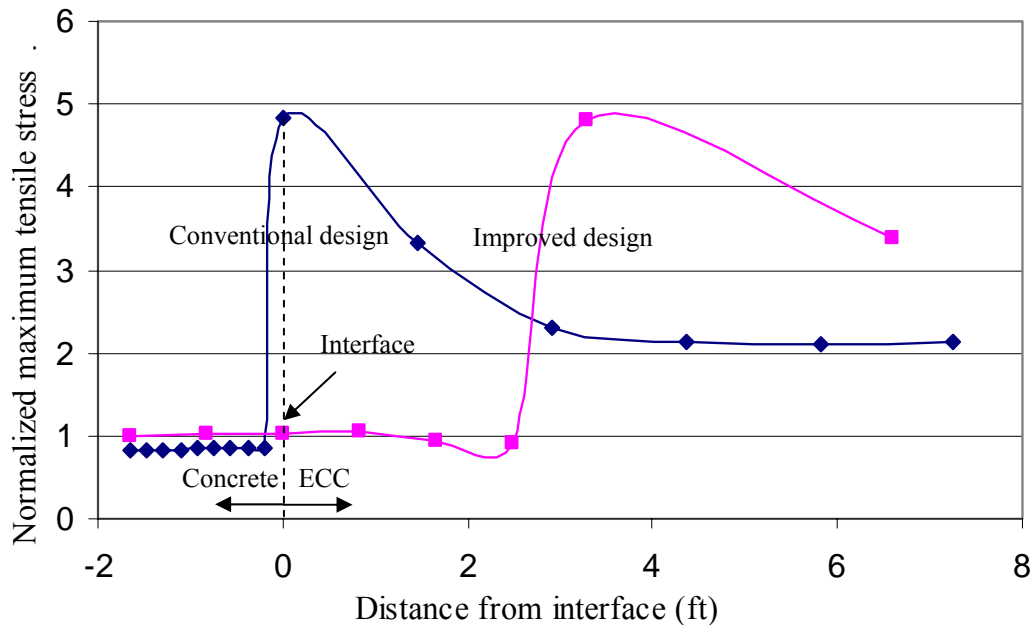


Figure 6.3 Normalized envelope stress developed at the top surface of link slab, ■ computed stress envelope for Improved Design, ◆ computed stress envelope for Conventional Design

7.0 Testing of ECC link slab/concrete deck slab interface

In the proposed interface design between the ECC link slab and concrete deck slab, the location of the shear studs connecting the steel girder and the deck are extended into the ECC link slab to reduce interfacial stress (Figure 6.1b). In addition to shear studs, the existing longitudinal reinforcements are lap spliced with new reinforcing bars within the ECC link slab.

Given these two improved methods to strengthen the interface, however, the development length of the reinforcement in ECC has not been examined. With sufficient embedment length, undesirable cracking at the interface or failure associated with the reinforcement pullout can be prevented. Current design codes such as ACI 318 and AASHTO code provide requirements for the development length of reinforcement in concrete, but the applicability of these codes needs to be demonstrated if these codes were to be directly adopted for ECC link slab design. Therefore, it is desirable to obtain the development length of reinforcement embedded in ECC by implementing a reinforcement pullout test. Companion concrete specimens were tested as well. Since

epoxy-coated reinforcement is widely used in bridge construction in Michigan, epoxy-coated reinforcement embedded in ECC specimens were also tested in pullout mode. In this test, ECC M45 was investigated, along with reference concrete.

Similarly, the load capacity of a stud shear connection in ECC also needs to be examined. With sufficient load capacity, the composite action of the girder and link slab within the transition zone can prevent undesirable cracking at the ECC/concrete interface. The current AASHTO code provides requirements for the ultimate strength (load capacity) of a stud shear connection in concrete, but the applicability of the code must be validated when ECC is used to replace concrete. To obtain the load capacity of shear connections in ECC, a pushout test on studs in ECC was performed. Companion concrete pushout specimens were tested as well. In this test, ECC M45 and its modified version M45+ (higher water/cement ratio to reduce compressive strength) were investigated, along with reference concrete, in which M45+ has a comparable compressive strength as concrete, as shown in Table 7.1.

Table 7.1 Mix Proportion of ECC and concrete by weight and compressive strength (fiber by volume)

Mix	C	W	S	CA	FA	SP	Fiber	f_c' (ksi)
concrete	1	0.45	2	2	0	0	0	5.5 ± 0.2
M45+	1	0.58	0.8	0	1.2	0.03	0.02	6.7 ± 0.1
M45	1	0.53	0.8	0	1.2	0.03	0.02	8.7 ± 0.3

(C: Type I Portland cement; W: water; S: silica sands for M45, regular sand for concrete; CA: coarse aggregate with max size $\frac{3}{4}$ inch; FA: Type F fly ash; SP: Superplasticizer; Fiber: PVA fiber, KURALON K-II REC15, developed by Kurary Co., LTD (Japan) in collaboration with ACE-MRL; f_c' : Average compressive strength based on 3 specimens)

7.1 Development length of reinforcements in ECC

7.1.1 Specimen design and experimental setup/procedure

According to Section 8.20 of AASHTO code, reinforcements for resisting shrinkage and temperature stresses are required, and the total area of reinforcement should be at least $1/8$ inch²/foot in each direction. To provide this amount of reinforcement, No.3 or No.4 reinforcement with spacing of 10 in. or 18 in. are placed longitudinally in the decks of simple span bridges. An observation of a patch repair of a

Michigan bridge deck (Curtis Rd over M14, Ann Arbor) confirms that the longitudinal reinforcements are No.3 bars with approximately 18 inch spacing (Figure 7.1). Considering the retrofit of an existing bridge using an ECC link slab, No.3 reinforcements are expected to be lap spliced with new reinforcing bars of the ECC link slab. Thus, pullout specimens were employed to assess the required development length as well as pullout failure mode focusing on No. 3 bars in concrete and ECC since the existing No. 3 bars have the potential to pull out from concrete or ECC link slabs.

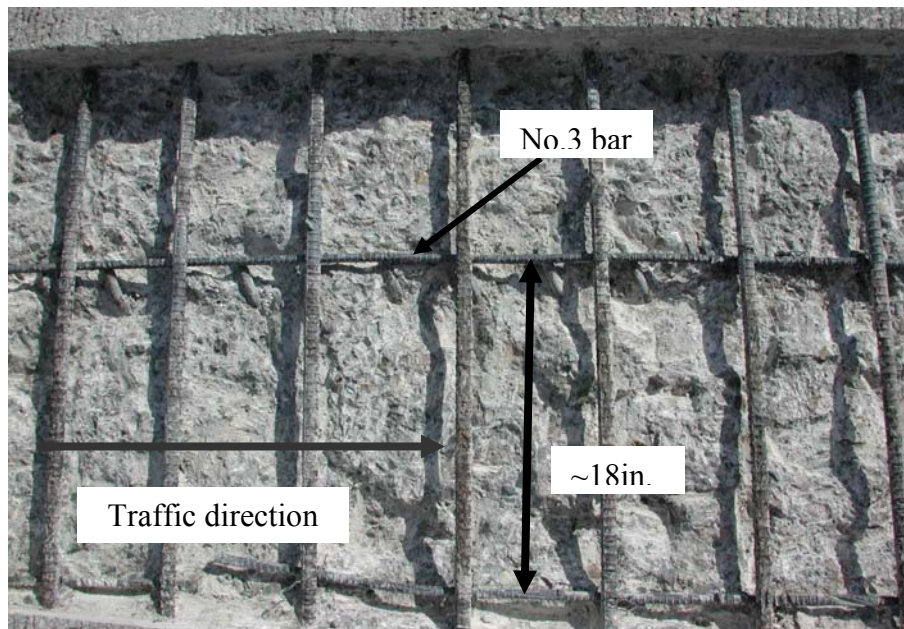


Figure 7.1 Exposed reinforcements before patch repair

The specimen had cross-sectional dimensions of 6in. by 6in. and length of 16in. Exposed No. 3 reinforcement inside the mold is shown in Figure 7.2. Specimens with embedment lengths of 6 in. along with different surrounding materials (ECC and concrete) were prepared for pullout tests.

The load was applied by a steel plate attached to the four threaded bars with nuts at the end to enhance anchoring. During casting, plexiglass plates (on the left end of the mold) were used to ensure the steel plates conformed to the ECC surface such that the applied load can be uniformly transferred. To assure the alignment of reinforcement, two parallel plates were set up with the same size hole at the center. All specimens were demolded after 24 hours and were then cured in air for 28 days.

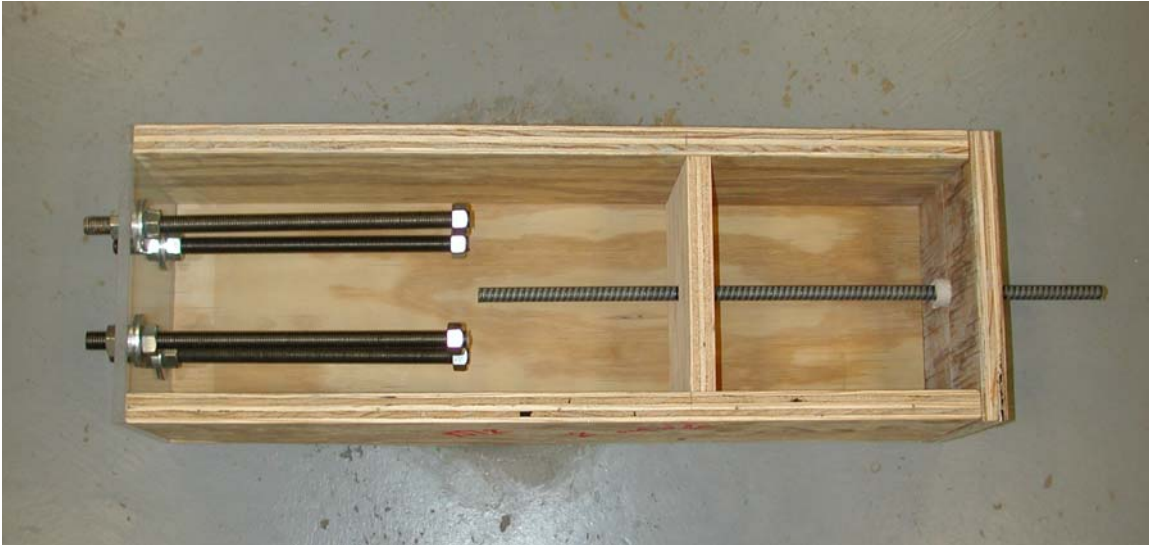


Figure 7.2 Exposed No.3 reinforcement and threaded bars of pullout specimen before casting

All specimens were tested on a MTS testing machine, as shown in Figure 7.3. The protruding reinforcement was gripped at the top with a frictional grip while the steel plate with a welded steel tab was gripped at the bottom. The pullout displacement was measured by a pair of linear variable displacement transducers (LVDTs) on either side of the specimen attached to the steel reinforcement close to the embedded portion of the specimen (Figure 7.4). Loading was applied under displacement control at a rate of 0.0002 in/second.



Figure 7.3 Pullout test setup



Figure 7.4 LVDTs attached to the reinforcement for measurement of pullout displacement

7.1.2 Pullout test results

From the comparison of the pullout load-displacement curves of No.3 reinforcement in concrete and ECC (Figure 7.5 (a) and (b)), both yield at 7.1 kips corresponding to a yield strength of 65 ksi for the bare steel reinforcement. After the yield plateau, reinforcement in both concrete and ECC show a strain hardening regime before the pullout process begins at peak load. The average peak load from pullout tests are 10.8 kips and 10.3 kips for concrete and ECC specimens respectively. This indicates that a 6 inch embedment length (half of the code recommended minimum development length) is adequate to develop the yield strength of reinforcement in ECC, and that reinforcement embedded in ECC has comparable bond properties with that of reinforcement embedded in concrete, in terms of the peak load.

Furthermore, with ECC material as the surrounding matrix, there is no major difference between the pullout behavior of bare and epoxy-coated reinforcement, as shown in Figure 7.5 (b) and (c). Epoxy-coated reinforcement shows only a slightly higher yield load (7.5 kips) and average peak load (10.7 kips) than regular reinforcement (7.1 kips and 10.3 kips).

From the above observations, a 6 inch embedment length is found to be acceptable for both regular and epoxy-coated reinforcement in ECC since peak pullout loads exceed the yield load. Additionally, AASHTO requires a 12 inch development length for No. 3 reinforcement of grade 60. Given the increased modification factor of 1.2 or 1.5 for epoxy-coated reinforcement in the AASHTO code, a safety factor of two exists for the development length of epoxy-coated reinforcement in ECC.

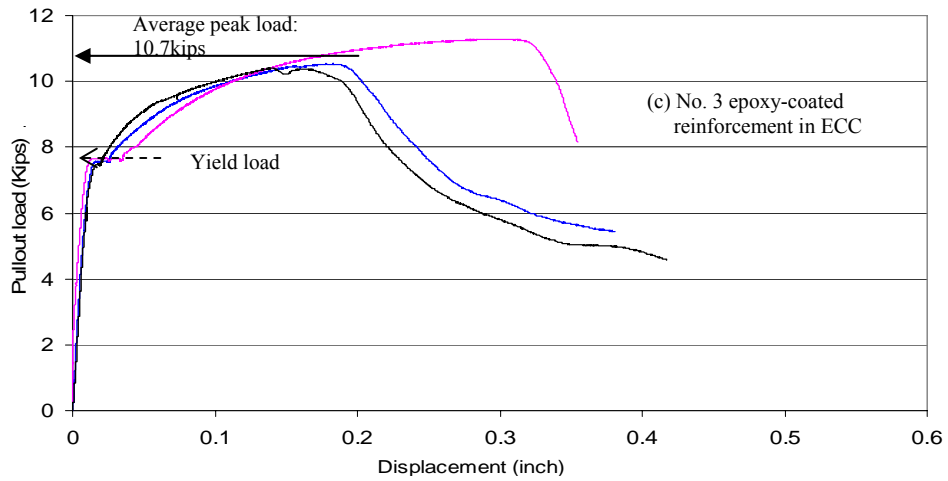
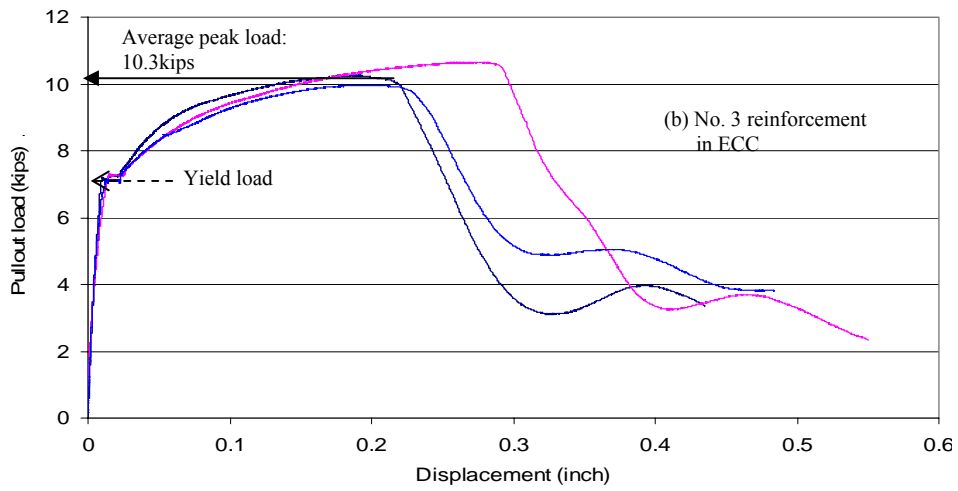
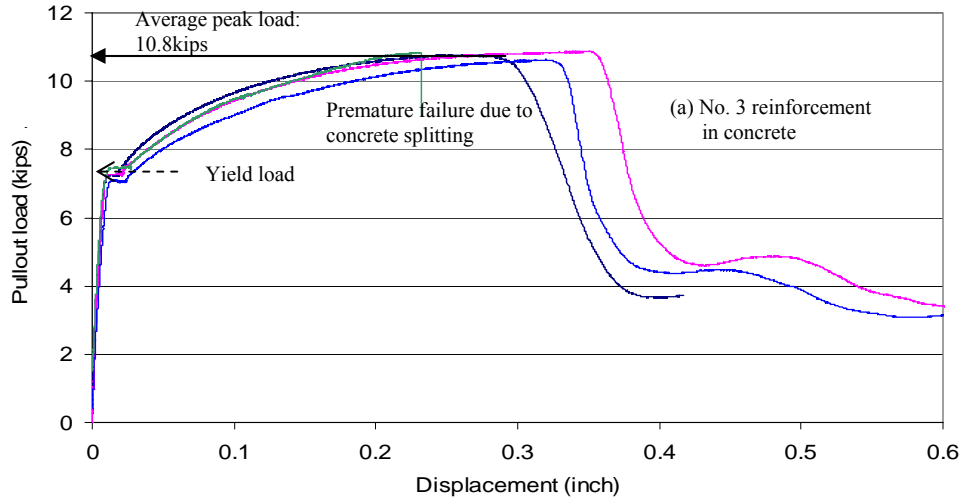


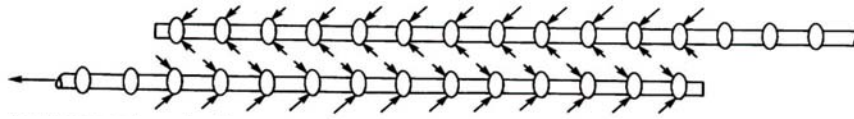
Figure 7.5 Comparison of pullout load-displacement curves for No. 3 reinforcement (a) in concrete; (b) in ECC; and (c) No. 3 epoxy-coated reinforcement in ECC, with 6 inch embedment length (where yield load corresponds to the yield strength of bare steel reinforcement)

7.2 Lap splice length of reinforcement in ECC

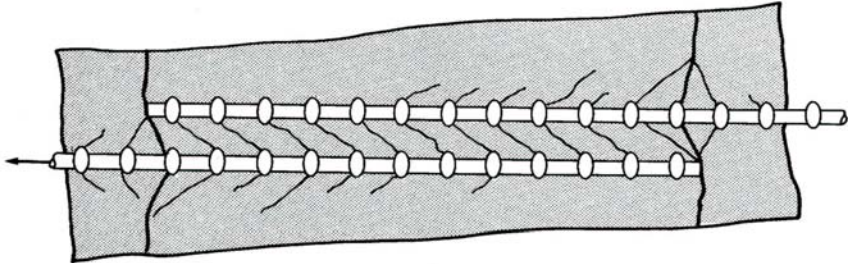
In a lapped splice, the force in one reinforcement is transferred to the surrounding matrix, which then forwards it to the adjacent lapped bar. The force transfer mechanism is shown in Figure 7.6 (a), along with the typical associated crack pattern in Figure 7.6 (b) in concrete. The transfer of forces out of the bar into the concrete is accompanied by radially outward pressures acting on the matrix by the deformed lugs on the bars, as shown in Figure 7.6 (c), which in turn results in splitting cracks along the bars. Once these occur, the splice fails as shown in Figure 7.6 (d). Splitting cracks typically initiate at the ends of the splice where the splitting pressure is usually largest. In addition to splitting cracks, large transverse cracks, which may occur at the ends of the spliced reinforcement, also contribute to the failure of the lap splice. To address this potential brittle failure of the lap splice in concrete, the AASHTO design code requires an increase of splice length over development length by a factor of 1.3 or 1.7, depending on the ratio of the amount of reinforcement (A_s) provided to required, and the percentage of A_s spliced within required lap length.

The ductile pullout failure mode of ECC indicates that the brittle failure of lap splices in concrete would not happen in ECC. As shown in Figure 7.7, it is obvious that the pullout failure mode of the reinforcement from the ECC specimen (frictional pullout) is much more ductile than that of the concrete specimen (splitting), due to the high toughness and ductility of ECC material. In ECC, the reinforcement exhibits frictional pullout failure without causing splitting or transverse macroscopic cracks. Similar ductile failure modes were observed in epoxy-coated reinforcement pullout tests with ECC. In some concrete specimens, the reinforcement pullout process results in catastrophic splitting failure of the specimen accompanied by noticeable transverse cracks. The corresponding pull-out curve is shown in Figure 7.5 (a) with a pre-mature sudden load-drop.

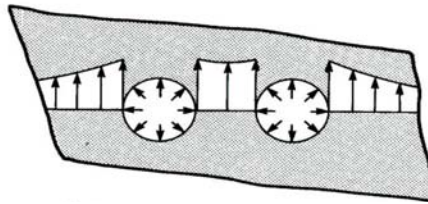
From the above observations, the modification factor of 1.3 or 1.7 for reinforcement lap splice length with respect to development length cannot be directly applied to ECC. However, for design purposes and convenience, adoption of the AASHTO code is expected to be conservative for the design of reinforcement splicing in ECC.



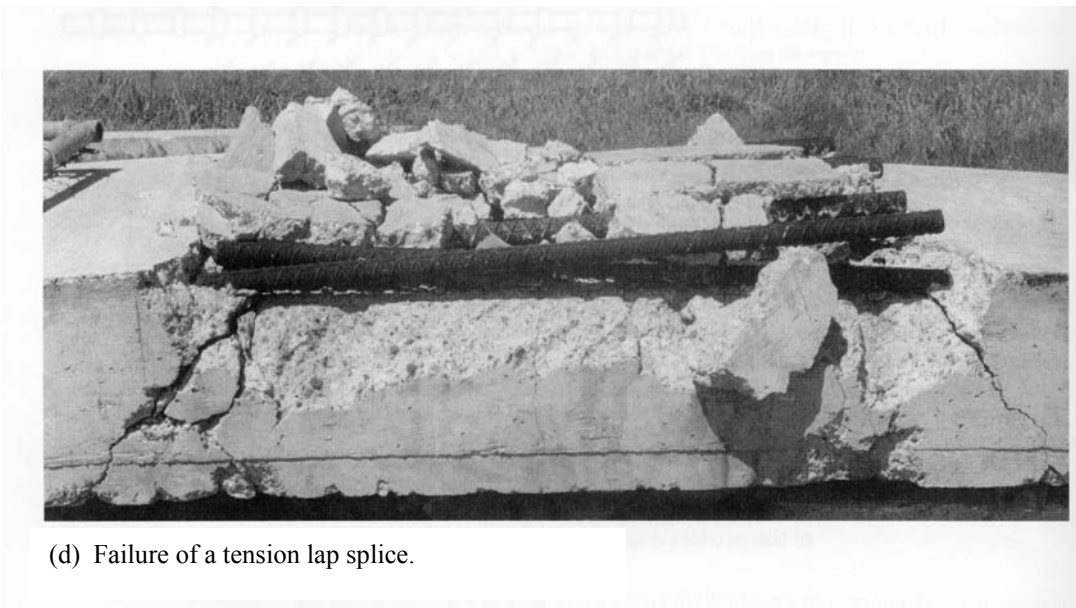
(a) Forces on bars at splice.



(b) Internal cracks at splice.

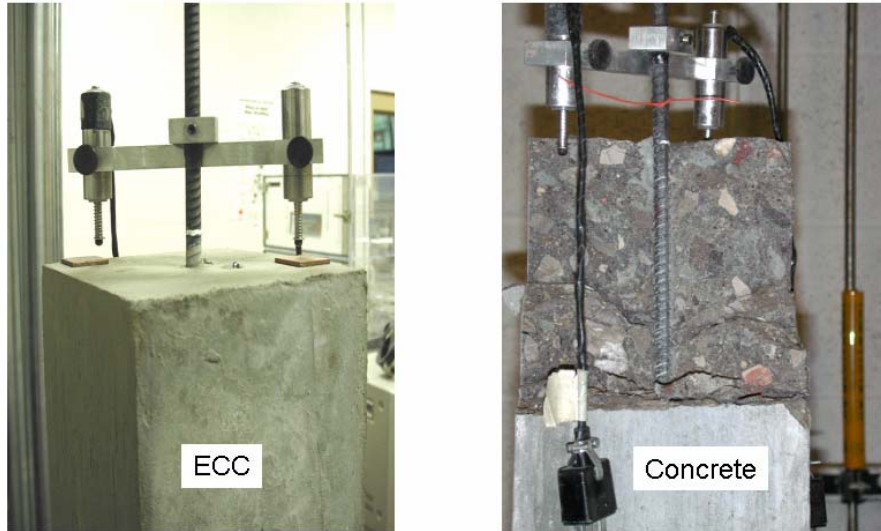


(c) Radial forces on concrete and splitting stresses shown on a section through the splice.



(d) Failure of a tension lap splice.

Figure 7.6 Lap splice of bars in concrete (J. G. MacGregor, 1998)



(a) Ductile frictional pullout failure in ECC (b) Brittle splitting failure in concrete accompanied by noticeable transverse cracks.

Figure 7.7 Comparison of pullout failure modes between ECC and concrete specimen.

7.3 Stud shear connection in ECC

7.3.1 Experimental preparation and setup

The ECC mix M45 and M45+ was used in this test. The ECC mix M45+ has a higher water cement ratio compared with M45 (Table 7.1), so that the compressive strength of M45+ can be comparable to that of the concrete used. M45+ shows a strain capacity around 3% at 28 days age ($2.9 \pm 0.4\%$ based on 3 specimens), similar to M45.

The shear studs used in this test are made from Grade 1018 cold drawn bars, conforming to AASHTO M169 (ASTM A108) Standard Specification for Steel Bars, Carbon, Cold-Finished, Standard Quality. The studs have a minimum yield and tensile strength of 50 ksi and 60 ksi, respectively. The geometry of a shear stud is shown in Figure 7.8.



Figure 7.8 Geometry of a shear stud

The geometry of the pushout specimen is shown in Figure 7.9. Two substrate slabs 12"x12"x6" of matrix material (concrete or ECC) are connected with a wide flange steel beam W8X40 with two shear studs welded on each side of the beam. The geometry is adopted from Ollgaard et al. (1971). During casting, the material is poured from the top of the specimen. Therefore, the steel beam will remain vertical, such that the loading plane is horizontal. Even though this casting orientation is different from field conditions, the pouring direction is thought to be unimportant since PVA fibers in ECC are likely to be distributed in a 3-dimensional state.

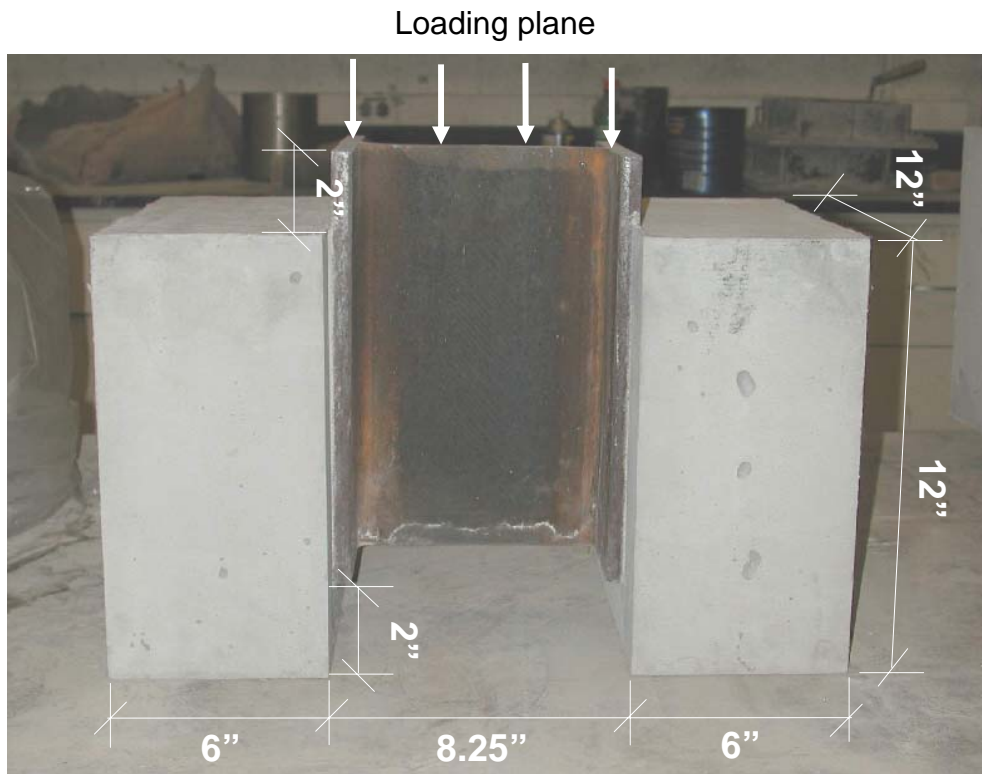


Figure 7.9 Geometry of the pushout specimen (unit: inch)

The ECC specimens were cured in air, and concrete specimens cured in water for 28 days. To ensure the symmetry of the two slabs, the plywood molds were constructed using two integral side plates and a single bottom plate. Testing was conducted on a 500-kip capacity Instron testing machine, as shown in Figure 7.10. Four LVDTs were mounted on the steel beam at the level of the shear studs to measure the slip between the beam and concrete slabs. An average value was taken from these four measurements.

The loading surface was ground for uniform load distribution before testing, and a ball support was used to maintain the alignment of the specimen.

7.3.2 Pushout behavior of concrete and ECC specimens

The overall performance of the ECC/stud system is revealed to be better than the concrete/stud system in terms of failure mode, slip capacity (ductility), and load capacity. Failure modes are switched from brittle matrix failure in concrete specimens to ductile steel yielding in ECC specimens, leading to a higher ductility of ECC specimens at higher loads, as illustrated by Figure 7.11.

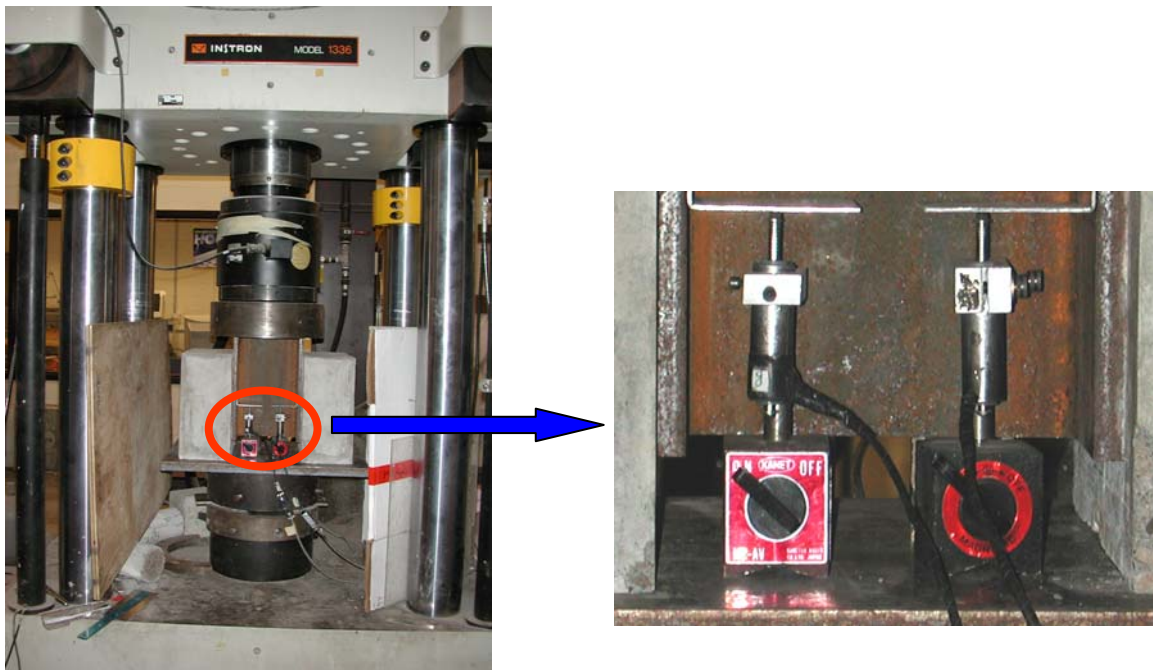


Figure 7.10 Setup of pushout tests and close view of LVDTs

In concrete pushout tests, as loading approached the peak value, large cracks formed near the shear studs and developed rapidly throughout the entire specimen as the peak load was reached. As seen in Figure 7.12, concrete specimens fractured into several parts after testing, clearly initiated from the head of the shear studs. The sudden drop after peak load in Figure 7.11(a) demonstrates that after the concrete was fractured, the bearing resistance of concrete was drastically reduced. The concrete under the shear stud was crushed due to large bearing stress of the stud shank. The brittle nature of concrete

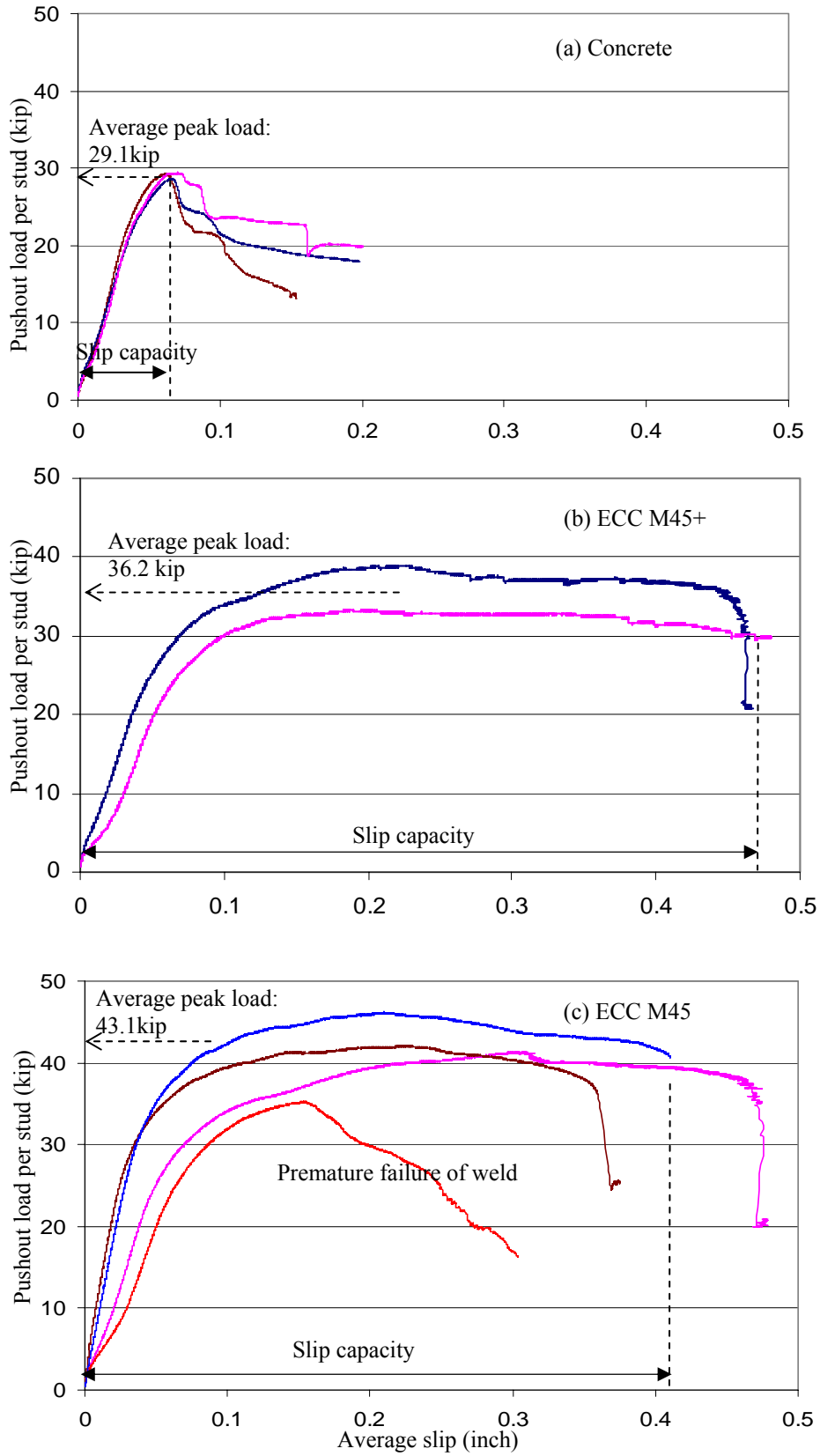


Figure 7.11 Comparison of pushout load per stud–average slip curves for specimens made of (a) concrete; (b) ECC M45+; (c) ECC M45



Figure 7.12 Macro cracks developed in concrete pushout specimen show a brittle failure mode



Figure 7.13 Microcracks developed outside (left) and inside (right, cut section along shear stud) of ECC specimen

lead to the rapid development of macro cracks, resulting in the catastrophic failure of concrete pushout specimens.

Conversely, ECC specimens show a ductile failure mode due to their unique strain hardening property. As can be seen from outside of the specimens, few cracks were initiated as the load increased, accompanied by starting of inelastic range in the load-slip curve. When peak load is reached, many microcracks are present, as revealed in Figure 7.13. In some cases, a dominant crack was initiated, but diffused into many microcracks ($\mu\text{crack width} = 0.00165'' \pm 0.0008''$) due to the ductile nature of ECC in tension. Since the ECC near the stud head developed a large microcrack zone, and the

bearing side resists the compressive force well, the ECC load-slip curve shows a large inelastic range (Figure 7.11 (b), (c)). The large slip capacity revealed in the ECC specimens indicates the feasibility of engaging adjacent shear studs in carrying the shear load.

Except for one specimen, which prematurely failed with a fracture of the stud welds, ECC specimens failed due to yielding and large deformation of the shear studs. This indicates that the use of ECC allows for “plastic yielding” of the matrix material, resulting in large deformation of the shear stud, and finally a shift of the failure from the matrix to the steel stud.

7.3.3 Load capacity of stud shear connection in concrete and ECC matrix

According to the AASHTO code, the ultimate strength of a stud in concrete is as follows:

$$Q_n = 0.5A_{sc}\sqrt{f'_c E_c} \leq A_{sc} F_u \quad (\text{Eq. 7-1})$$

with: A_{sc} = cross-sectional area of a stud shear connector (inch²);

f'_c = specified 28-day compressive strength of concrete (ksi);

E_c = Elastic modulus of concrete (ksi);

F_u = specified minimum tensile strength of a stud shear connector (ksi).

Table 7.2 shows the ultimate strength of a shear stud in the matrix, calculated assuming the validity of AASHTO code (Eq. 7-1) for both concrete and ECC. The tested average peak load per stud in concrete is 29.1 kips, slightly lower than the calculated value of 31.4 kips. Considering the influence of reinforced concrete, which shows a load increase of approximately 6% (An, et al 1996) over plain concrete, the average peak load can be up to 30.8 kips. This agrees well with calculated values, which is expected since the specimen setup is similar to the pushout tests performed by Ollgard et al (1971, adopted by AASHTO). In both tests, the brittle fracture of concrete was the dominant factor controlling the peak load.

Table 7.2 Calculated, measured strength, and slip capacity of a stud in concrete and ECC

Material	Compressive strength, f'_c (ksi)	Young's modulus, E_c (ksi)	Computed strength/stud Q_n (kip)	Measured strength/stud (kip)	Slip capacity (inch)
Concrete	5.5 ± 0.2	3700	31.4	29.1	0.07
M45+	6.7 ± 0.1	2800	30.2	36.2	0.48
M45	8.7 ± 0.3	2900	34.9	43.1	0.41

From the test results (Figure 7.11(b), (c)), the average peak load (ultimate strength) of a shear stud in ECC M45+ and M45 is about 36.2 kips and 43.1 kips, 18% and 23% higher than the calculated values, respectively. Interestingly, the average peak load per stud of ECC M45+ is around 25% higher than that of concrete while according to AASHTO they should have about the same ultimate strength. This is mainly due to the fact that the compressive strength, a main contributing factor in AASHTO design for studs in concrete, is not relevant to the failure of ECC specimens. Instead, the ductile strain hardening behavior caused “yielding” of the ECC, accompanied by a large deformation of the stud, leading to the higher load capacity of the ECC specimens. Therefore the direct adoption of AASHTO code is not suitable for ECC material. However, for design purposes and convenience, adoption of the AASHTO code leads to a large safety margin.

8.0 Laboratory testing of ECC link slab

8.1 Design of Test Specimens

While previous laboratory investigation of link slabs (Caner and Zia, 1998) involved testing of a 1/6 scaled bridge including a link slab with two adjacent spans, the present study focused on testing of a full-scale link slab portion exclusively. Therefore, the end rotations imposed on the link slab by the adjacent spans in a bridge were replicated in the laboratory.

The deformed shape and moment distribution due to applied load of a two-span bridge structure are schematically shown in Figure 8.1(a). Flexural crack formation was

expected at the top of the link slab as illustrated in Figure 8.1(b). Therefore, the link slab specimens were designed to include the link slab within the distance between the points of inflection in the adjacent spans. The location of inflection point should be determined by the stiffness of the link slab. In case of zero stiffness, the point of inflection is located at the support, while for a continuous girder and deck its location is around 25% of the span length from the support. In the case of a link slab with girder discontinuity, the point of inflection is located within these boundaries.

As described above, the specimen test setup focused on the link slab portion between the points of inflection in the adjacent spans as illustrated in Figure 8.1(b). Figure 8.2 shows the specimen geometry of both concrete and ECC link slabs, including the total debond zone length (50 in.) equal to 5.2% of adjacent span. For simplicity, the concrete specimen was cast continuous without the interface, which is conservative for the overall comparison of concrete and ECC link slabs. It is noted that the length and height dimensions of specimens are identical to a link slab between two adjacent 80' span bridges. The thickness of the link slabs was 9 in., which corresponds to typical deck slabs in simply supported composite girder bridges. The width of the link slabs was 28". As described earlier, the location of inflection point should be located in the range from 0% up to 25% of the span. The bridge model in Section 6.2 was used to find the inflection point of the bridge. First, a certain load P was applied at midspan of the bridge. After running the RISA program, the moment distribution of the bridge induced by load P was calculated. The location of zero moment was away from the support about 6.7% of the span length. Hence, we employed an inflection point at 6.7% of the span length based on aforementioned numerical analysis.

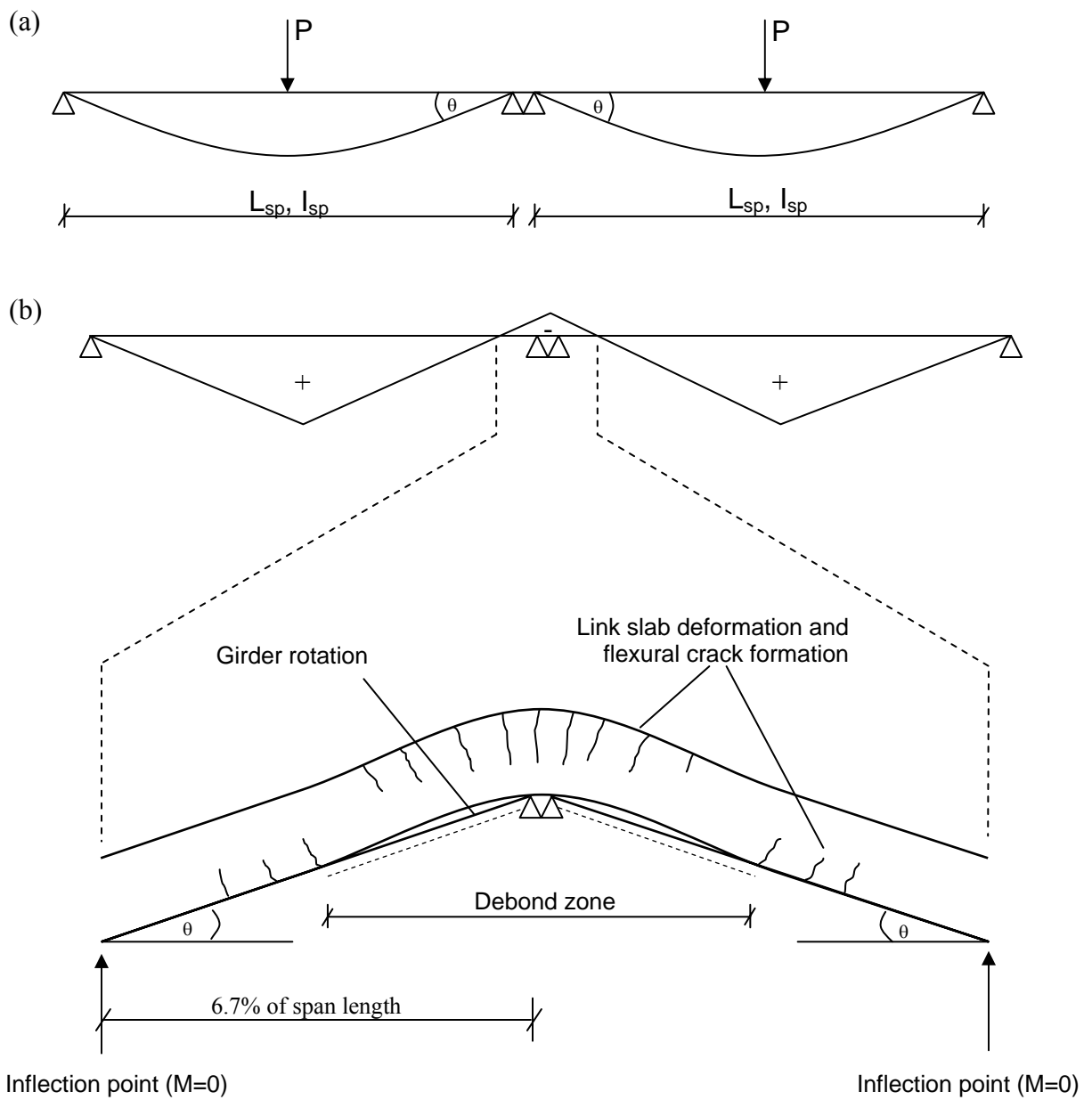


Figure 8.1 Schematics of two span bridge subjected to point load at midspan for (a) deformed shape of bridges; and (b) moment distribution on bridge span and corresponding deformed shape of link slab region.

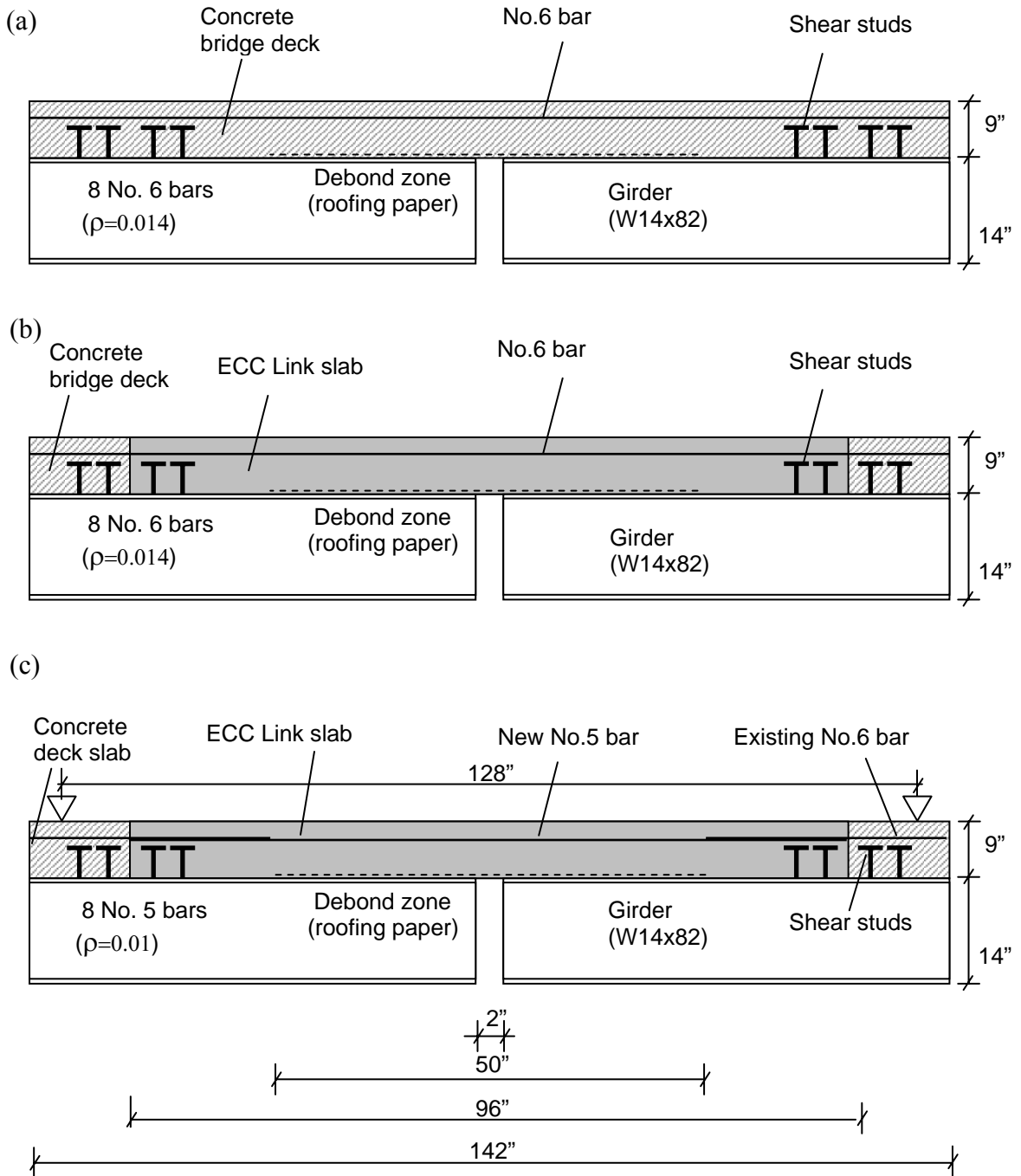


Figure 8.2 Geometry of link slab specimens for (a) LS-1; (a) LS-2; and (b) LS-3.

Three link slab specimens (Figure 8.2) were tested. Specimen LS-1, in which a concrete link slab reinforced with continuous No. 6 reinforcing bars and adjacent spans were cast together, was used to simulate the concrete link slab new construction. According to the current limit stress criterion of reinforced concrete link slabs (Caner and

Zia, 1998), the reinforcement ratio of the concrete link slab was determined to satisfy the stress criterion ($\sigma_s < 0.40\sigma_y$) at 0.0015 rad. end rotation angle. This is the expected rotation angle as derived by Caner and Zia (1998). The moment M_a developed in the uncracked concrete link slab is a function of the elastic modulus of concrete E_c and geometrical dimensions. It is proportional to the imposed end rotation angle

$$M_a = \frac{2E_c I_{ls,g}}{L_{dz}} \theta \quad (\text{Eq. 2-3})$$

where $I_{ls,g}$ is the moment of inertia of link slab based on uncracked section and L_{dz} is the debond zone length. Figure 8.3 illustrates the stress in the reinforcement at 0.0015 rad. end rotation angle and the reinforcement ratio chosen in this test. According to Eq. 2-6 and 2-10, $k = -n\rho + \sqrt{(n\rho)^2 + 2(n\rho)}$, $\sigma_s = M_a / (A_s (d - kd / 3))$. Given a known M_a in this test, and substituting k into σ_s , we can derive a relationship between stress and reinforcement ratio, as shown in Figure 8.3. In the debond zone, no shear connectors were used and 15-lb roofing paper was placed at the top of flange of the W14x82 girder.

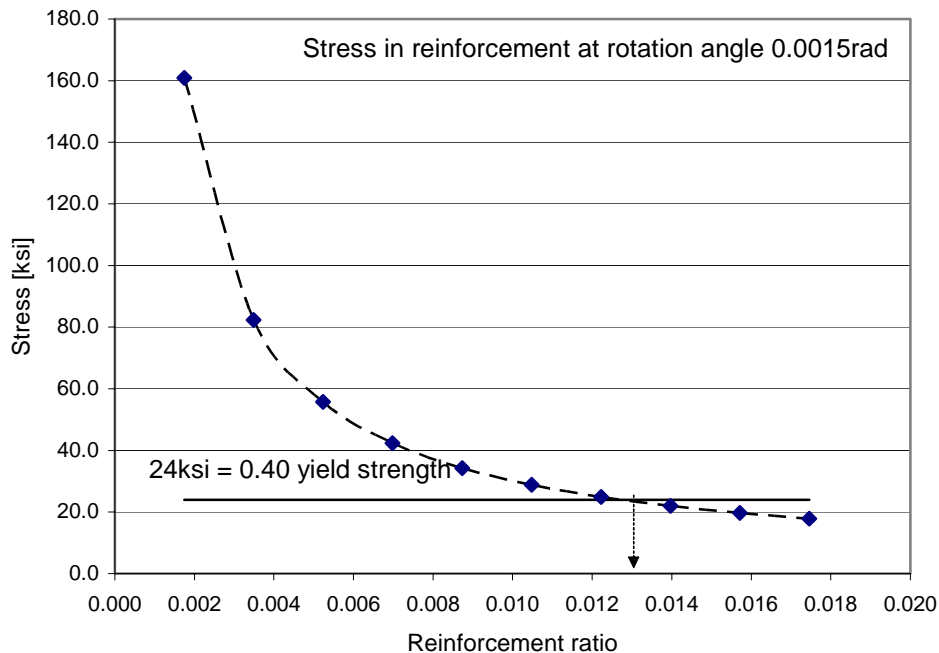


Figure 8.3 Required minimum reinforcement ratio 0.013 (0.014 used in the test) designed at expected rotation angle (0.0015 rad.).

Specimen LS-2 was prepared by removing the concrete from the link slab portion of specimen LS-1 and replacing it with an ECC link slab. This specimen was used to simulate the replacement of a concrete link slab with a new ECC link slab since the continuous reinforcement remained. The length of the link slab was 96 in. including 50 in. length of debond zone. The debond zone in the conventional concrete link slab has been designed to begin at the interface between deck slab and link slab, which results in locating the interface at the weakest part of the bridge deck system. In the present study, four shear studs were welded on the top of the girder flange (Figure 8.2 (b)) in order to strengthen the interface between ECC link slab and concrete bridge deck. The debond zone was 2.5% of span length for conservative concern (Calculated by Eq. 2-3 and shown in Table 8.1). The following steps were followed to prepare specimen LS-2 after the fatigue test on specimen LS-1.

1. Mark the section of the deck to be removed.
2. Provide a 1 in. deep saw cut across the width of the deck.
3. Chip out the concrete using hand held pneumatic breaker; care was taken not to damage the existing reinforcements and shear studs.
4. Place formwork; the interface was located behind the four shear studs.
5. Place a layer of 15-lb roofing paper on the top flange for debonding.
6. Pour two batches of ECC mixed in a 15.9 ft³ capacity drum mixer.

In order to investigate the effects of the reinforcement ratio on fatigue performance of ECC link slab, a third specimen LS-3 was prepared. Specifically, the focus of this test was on the fatigue performance of ECC link slab reinforced with a smaller amount of reinforcement compared to the design value and the fatigue cracking resistance of interface reinforced with the lap spliced existing reinforcement. As shown in Figure 8.2 (c), specimen LS-3 simulates the retrofit of an existing bridge replacing mechanical joints with an ECC link slab. This specimen was prepared by removing the ECC from the link slab portion of specimen LS-2 and pouring new ECC into the removed portion. The existing No.6 reinforcements were cut out with 20 in. left at both ends of link slab. These 20 in. exposed No.6 bars were lap spliced with new No.5 bars to simulate the retrofit of an existing bridge. A reinforcement ratio of 0.01, which is lower than that of specimen LS-1

and LS-2, was employed as the reinforcement ratio of the specimen LS-3. The following steps were followed to prepare specimen LS-3 after the fatigue test on specimen LS-2.

1. Mark the section of the deck to be cut out.
2. Provide saw cut across the width and depth of the deck to cut out the link slab portion of specimen LS-2 except for the lap splice portion.
3. Mark the section of the deck to be chipped out and provide a 1 in. deep saw cut across the width of the deck.
4. Chip out the ECC using hand held pneumatic breaker.
5. Place new reinforcements with 20 in. lap splice length.
6. Place formwork and a layer of roofing paper on the top flange for debonding.
7. Mix and Pour ECC into formwork to create the ECC link slab.

8.2 Experimental Setup and Procedure

The experimental investigation of ECC link slabs was conducted using a representative section (28" wide) of a link slab between the inflection points of the adjacent deck slabs (128" long). The zero moment condition at the inflection points as well as the boundary conditions at the pier were simulated by roller supports at the specimen end supports and at the load points (Figure 8.4). For practical purposes, the test setup represents an inverted orientation of the link slab region.

The loading sequence chosen was similar to the procedure adapted by MDOT. As shown in Figure 8.5, all specimens were subjected to sequential static loading up to two times the deflection causing a reinforcement stress in the specimen LS-1 of 40% of its yield strength, which is the current limit stress criterion for concrete link slab design. The final step of sequential static loading stage simulates potential overload (midspan deflection 0.375 used). In the subsequent cyclic loading procedure, the load at 40% yield of the reinforcement in LS-1 is chosen as the mean load with amplitude up to maximum deflection at 0.00375 rad. end rotation angle (Figure 8.5). This maximum rotation angle θ_{max} (0.00375 rad.) corresponds to the allowable deflection of a bridge span under live load (Δ_{max} , $L_{sp}/800$ in AASHTO code).

$$\theta_{\max} = \frac{\Delta_{\max}}{\Delta} \theta = \frac{\Delta_{\max}}{PL_{sp}^3 / 48 EI_{sp}} \frac{PL_{sp}^2}{16 EI_{sp}} = \frac{L_{sp}}{800} \frac{3}{L_{sp}} = 0.00375 \text{ rad} \quad (\text{Eq. 8-1})$$

where L_{sp} is bridge span length and EI_{sp} is flexural rigidity of the bridge section. Cyclic loading was carried out to 100,000 cycles due to restrictions in the availability of the testing equipment. It should be noted that these test conditions are five times that assumed under field conditions in terms of the bending moment since the debond length is 2.5% of span in test instead of 5%. (Calculated by Eq. 2-3 and shown in Table 8.1).

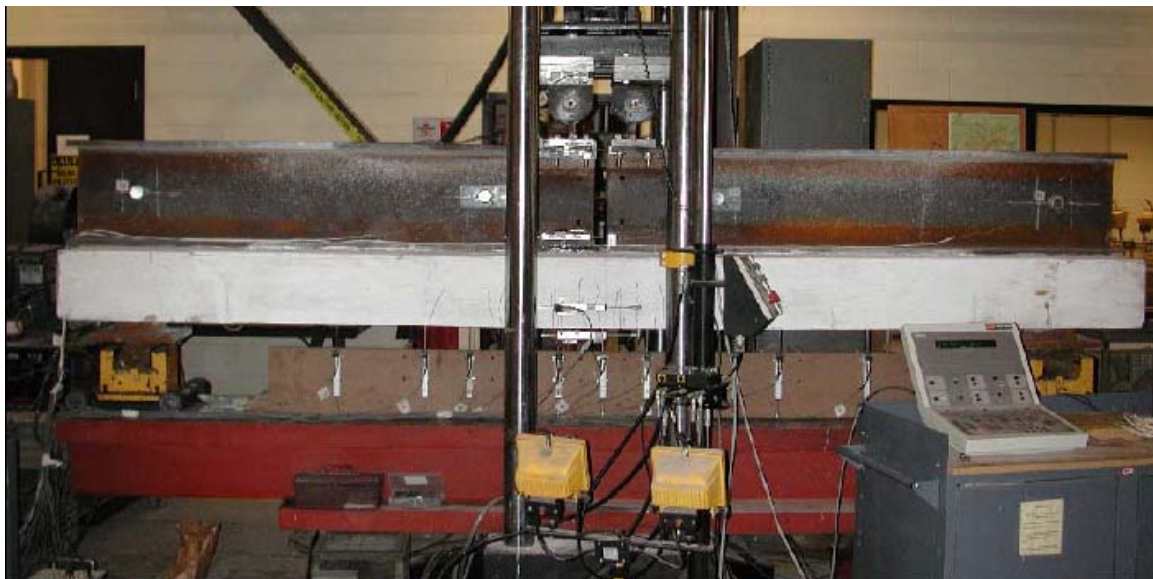
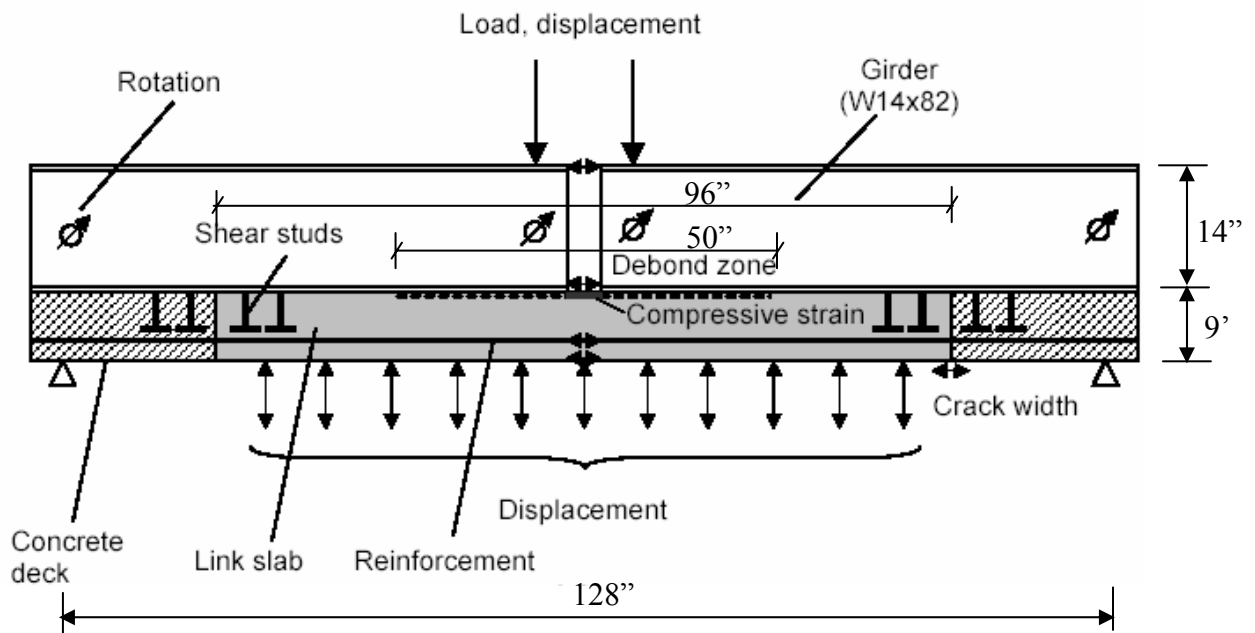


Figure 8.4 Laboratory test setup and instrumentation of specimen.

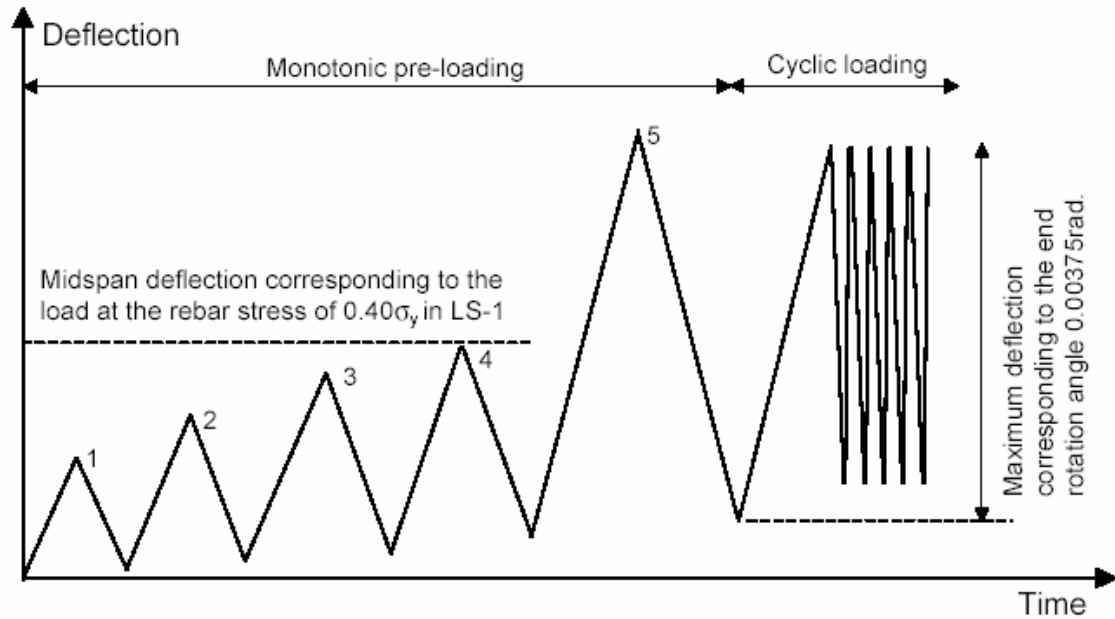


Figure 8.5 Loading sequence, in which the midspan deflections at step4 corresponds to the load at the reinforcement stress equal to $0.4\sigma_y$ in specimen LS-1.

Table 8.1 Comparison between laboratory testing condition and field condition

Condition	End Rotation Angle θ	Debond length	M_a *
Field	0.0015 rad.**	5.0% of span length	M_a in field
Lab. testing	0.00375 rad.	2.5% of span length	5 times of M_a in field

* Moment developed in the link slab at end rotation angle θ ; (Eq. 2-3)

** End rotation angle expected in field as derived in Caner and Zia (1998)

During testing, the applied load, displacements, rotation angles, strains at the compressive face of link slab at midspan and interfacial crack width of the specimen as indicated in Figure 8.4 are monitored using a data acquisition system. Cracks are marked and crack widths are measured at each loading sequence during the monotonic pre-loading procedure as well as at every 10,000 cycles during the cyclic loading procedure.

8.3 Monotonic Behavior of Link Slab Specimens

A monotonic test on the link slab specimen was conducted before fatigue testing. After this initial test, the experimental data were examined and fatigue testing was continued. For LS-1, at a midspan deflection of 0.06" (first step), a small transverse crack formed across the deck near the midspan of the link slab. The crack width gradually grew wider during subsequent loading and reached 0.005" at the final deflection step (0.37") of the monotonic pre-loading test. Additional cracks appeared and propagated across the width of the link slab as the midspan deflection was increased. Ultimately, seven cracks were observed during pre-loading test. Two of those cracks formed within the gage length (9") of LVDTs at midspan. The crack widths within the gage length were below 0.002" up to final deflection step while the width of the largest cracks that developed kept growing (0.005" at final deflection step) as the loading step increased. In contrast to that, several microcracks appeared in the debond zone of LS-2 and LS-3 at a midspan deflection of 0.06" (first step) and 0.1" (second step). Additional hairline cracks formed as the midspan deflection was increased. All the crack widths remained below 0.002" up to the final deflection step (0.375") of pre-loading test.

Figure 8.6 shows the load vs. midspan deflection curves of the three specimens tested. Significant differences in the global response of specimens LS-1 and LS-2 are not apparent. However, the responses in an individual cross section were distinct for the concrete and ECC link slabs. Figure 8.7 illustrates the strain distribution at three locations across the midspan section at each loading step. In this figure, the matrix strain at the tension face and the reinforcement strain were calculated by dividing the measured LVDT

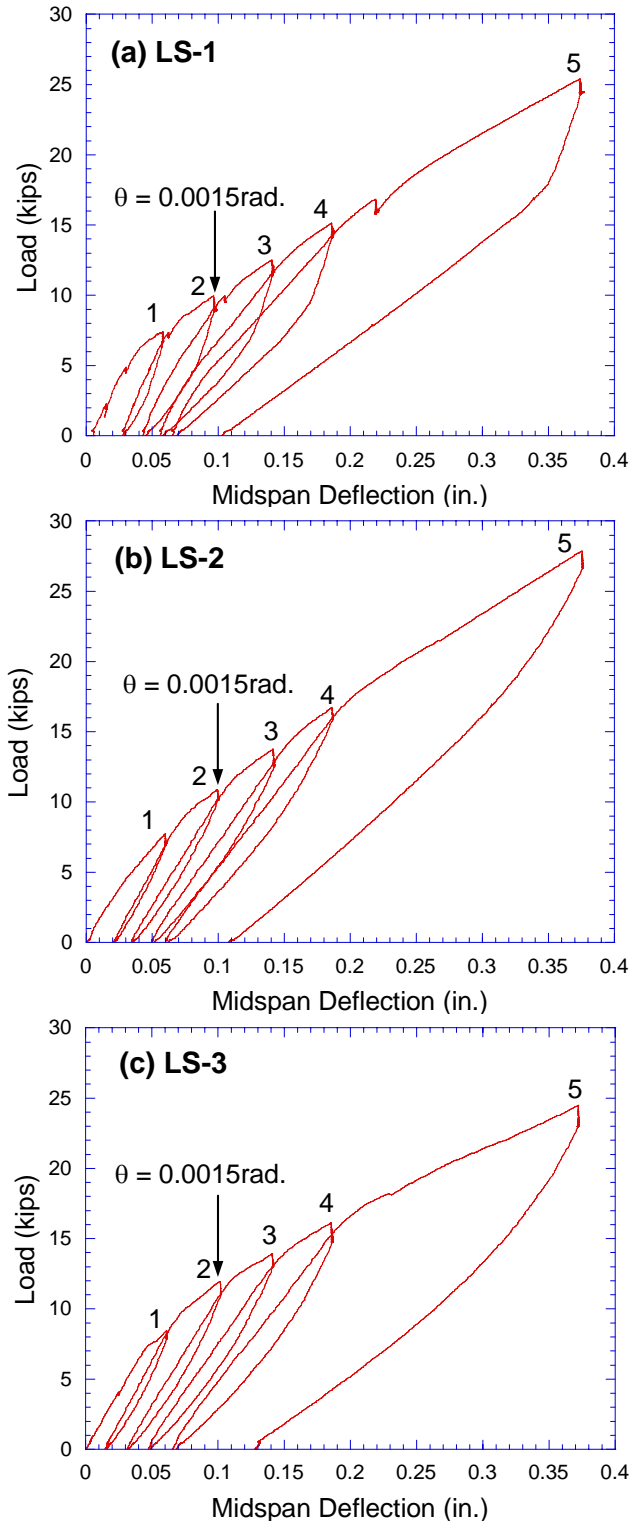


Figure 8.6 Applied load vs. midspan deflection curves during pre-loading test (step1: 0.06in., step2: 0.10in., step3: 0.14in., step4: 0.185in., and step5: 0.375in. in midspan deflection) on (a) LS-1; (b) LS-2; and (c) LS-3.

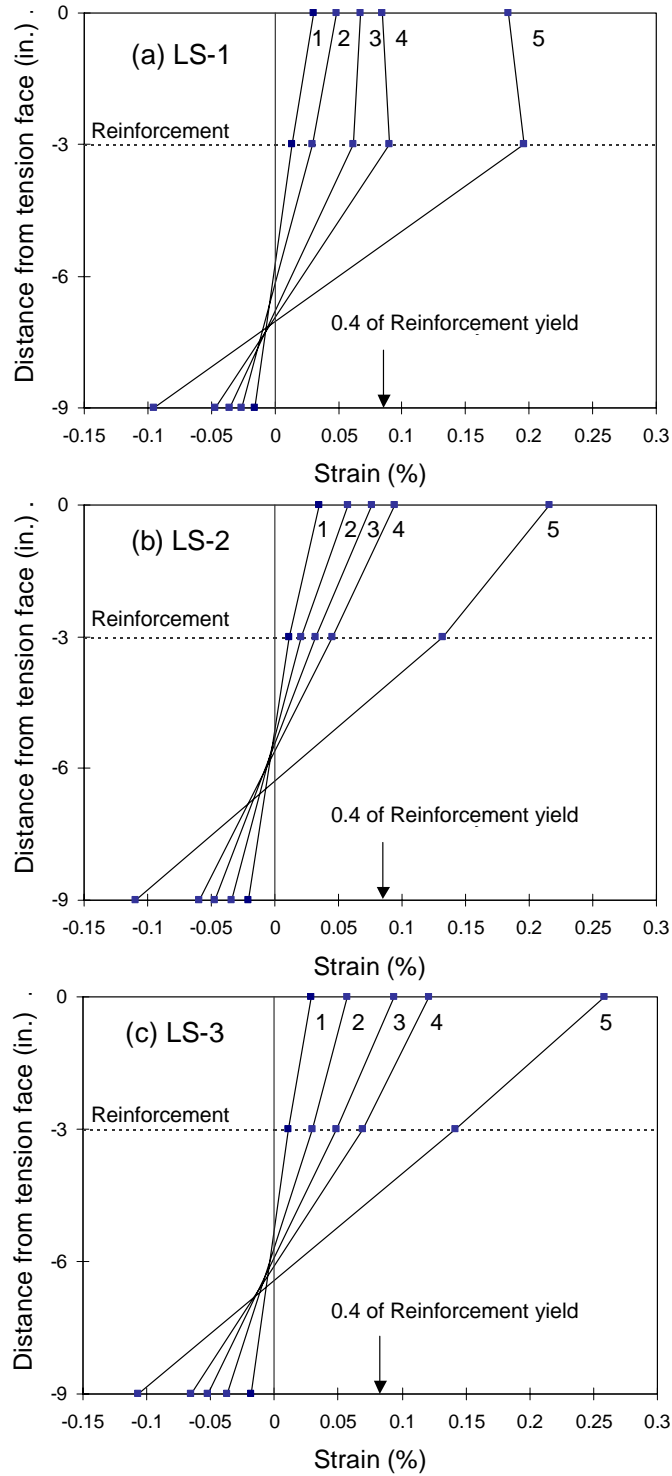


Figure 8.7 Strain distribution measured at three data points across the midspan section at each loading step (step1: 0.06in., step2: 0.10in., step3: 0.14in., step4: 0.185in., and step5: 0.375in. in midspan deflection) for (a) LS-1; (b) LS-2; and (c) LS-3.

displacement by the gage length (9 in.) while strains at the compression face were obtained by averaging data measured from two strain gages placed on the compression face of the link slab at midspan. A comparison of stresses in the reinforcement at the design rotation angle 0.0015 rad. revealed the reinforcement strain of the ECC link slab LS-2 (~0.02%) was relatively smaller than that of the concrete link slab LS-1 (~0.03%). The difference between these two reinforcement stresses became larger as the midspan deflection was increased. This is due to the strain hardening and microcracking of ECC material allowing for compatible deformation of the ECC matrix with reinforcing bars as well as due to the lower stiffness of ECC as compared to concrete in compression.

A comparison of the sequential strain development at midspan section in the three specimens confirms the strain compatibility of ECC link slabs (Figure 8.7). Because of the different distances from the neutral axis of the beam, the measured strain on the tensile face (of concrete and ECC) should be higher than that in the reinforcing bar, if the beam is acting elastically. At a midspan deflection of 0.14 in. (third step), the strain of reinforcement became almost identical to the concrete strain at the tension face in LS-1 specimen. The reinforcement strain became even larger than the concrete strain at the tension face during subsequent loading. This indicates that the concrete in specimen LS-1 lost compatibility with reinforcements due to the localized cracks outside the gage length of the LVDT. For the ECC link slabs, the difference between the strain of reinforcement and the ECC strain at tension face was maintained in a proportional manner, i.e., the three strain data points; ECC at tension face, reinforcement depth, and ECC at compression face, recorded at each step can be plotted on a straight line (Figure 8.7).

As shown in Figure 8.8, the compatible deformation between reinforcement and ECC initiate minimal interfacial shear stress if it exists at all, resulting in intact interface between steel bar and ECC. There is basically no shear lag between reinforcing bars and the surrounding ECC material in steel-reinforced ECC (R/ECC) while the brittle fracture of concrete in R/C causes unloading of concrete, resulting in high interfacial shear and interfacial bond failure (Li, 2002). Stress concentrations on the reinforcement are nonexistent even as the ECC is experiencing micro crack damage. Subsequently, the yielding of the reinforcement is delayed in the ECC matrix compared with that in the concrete matrix. In a study conducted by Fischer and Li (2002) on the tension stiffening

behavior of R/C and R/ECC, strain jumps were measured locally by strain gages attached to the reinforcing bar in concrete whenever the concrete cracked, but these stress jumps were not observed in the reinforcement in the ECC matrix. This unique behavior is caused by ECC material exhibiting a metal-like behavior and deforming compatibly with reinforcing bars. The micro cracks ($< 0.002''$ in widths) developed in ECC act as inelastic damage distributed over the bulk volume of ECC. In contrast, beyond the elastic limit, concrete experienced localized fracture.

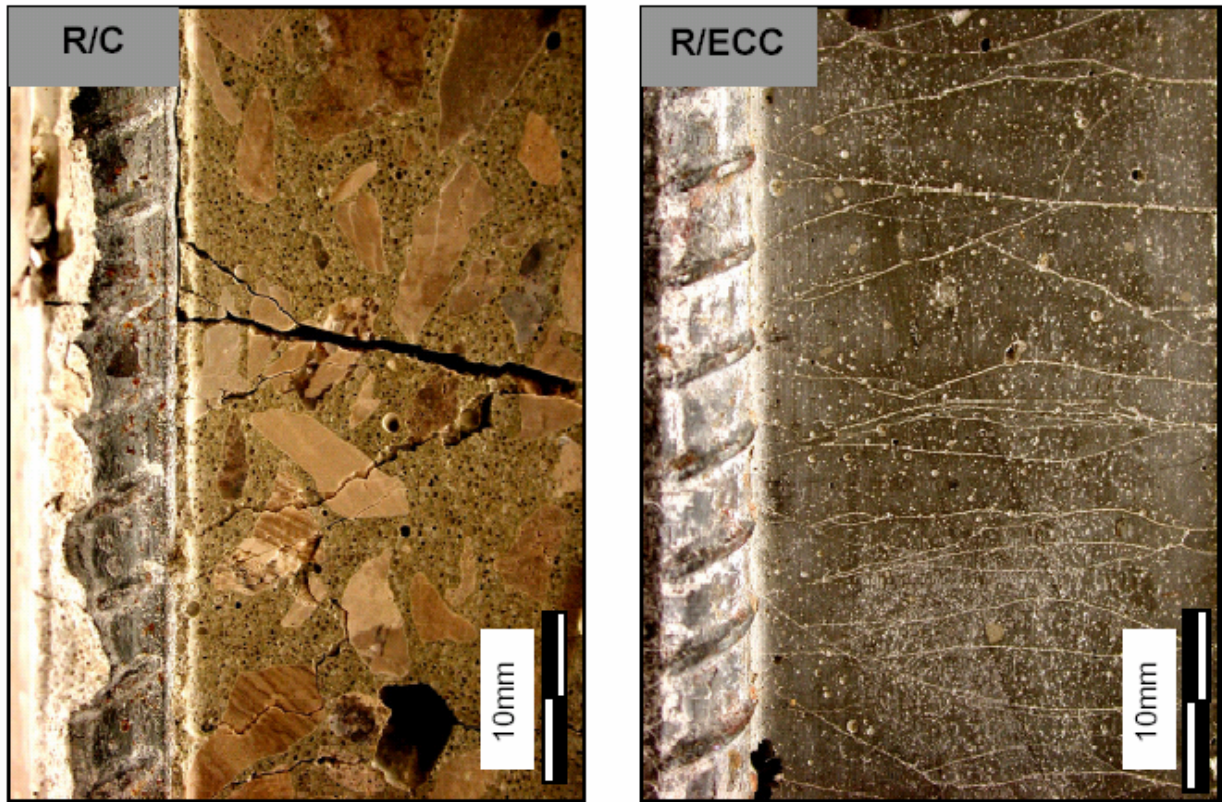


Figure 8.8 Compatible deformation between ECC and steel reinforcement (right) showing microcracking in ECC with load transmitted via bridging fibers. In contrast, the brittle fracture of concrete in normal R/C (left) causes unloading of concrete, resulting in high interfacial shear and bond breakage (Fischer and Li, 2002).

Assuming the same end rotation angle, θ , in both R/C and R/ECC members as seen in Figure 8.9, the members must have an identical curvature, Φ , based on identical span length L as shown in the following equation:

$$\Phi = \frac{M}{EI} = \frac{2EI\theta}{L} \frac{1}{EI} = \frac{2\theta}{L} \quad (\text{Eq. 8-2})$$

where M is the moment induced by end rotation angle, as determined by Eq.2-3, and EI is flexural rigidity. The neutral axis in R/ECC section is located closer to reinforcement when compared to a R/C section, since ECC in tension carries force while deforming compatibly with the reinforcement. Due to the difference in the location of neutral axis, however, the reinforcement strain in R/C is higher than in R/ECC (Figure 8.9). Lower reinforcement stress developed in the ECC link slab indicates that the amount of reinforcement in an ECC link slab can be reduced, resulting in lower structural stiffness. This will be discussed again in the next section on the fatigue cracking resistance of link slabs.

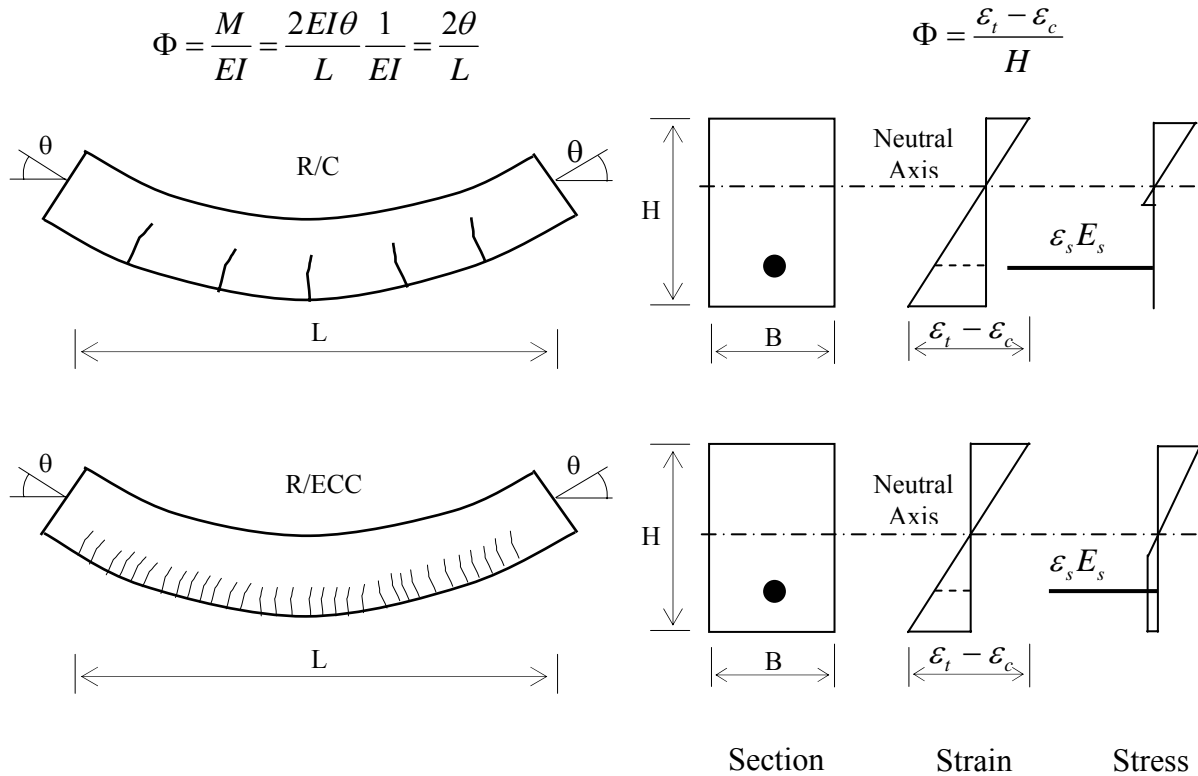


Figure 8.9 Comparison of reinforcement stress in between R/C beam and R/ECC beam with the same geometry and reinforcement ratio at identical rotation angle, θ , and curvature, Φ .

Reinforcement strain ($\sim 0.03\%$) of the concrete link slab at the design rotation angle of 0.0015 rad. did not reach 40% of the yield strain ($\sim 0.08\%$). This demonstrates that the assumption of the link slab in an uncracked condition caused the design moment M_a , based on current limit stress criterion (Caner and Zia, 1998), overestimates the required amount

of longitudinal reinforcement in the link slab (see Section 2). It should also be noted that the maximum strain at the tension face was measured to be lower than 0.1% at a design load corresponding to 0.0015rad. end rotation angle. Considering the relative magnitude of these quantities (0.1% strain caused by end rotation, 3% strain capacity), the ECC material in link slabs remains in the early strain-hardening regime.

8.4 Fatigue Cracking Resistance of Link Slab Specimens

Based on the monotonic test results of concrete specimen LS-1, the load at 40% yield of the reinforcement (~15 kips) was chosen as the mean load level with an amplitude up to a maximum deflection that created an end rotation of 0.00375 radians. Consequently, 0.16in. deflection amplitude was cyclically imposed on the link slab specimens. Figure 8.10 illustrates the response to cyclic loading as a function of midspan deflection during the test of specimen LS-3. This specimen was loaded from 5.8 kips up to 23.2 kips (mean load level = $(23.2-5.8)/2+5.8=14.5$ kips) with the maximum midspan deflection of 0.24in. calculated by subtracting initial residual deflection (~0.13in. caused by pre-loading test) from total deflection (~0.37in.). This maximum midspan deflection corresponds to the maximum end rotation angle of approximately 0.00375 radians.

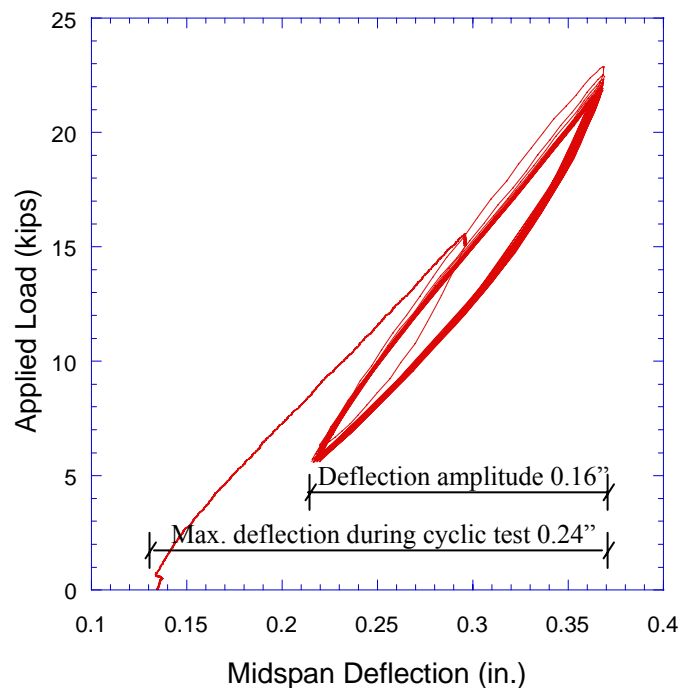


Figure 8.10 The response of midspan deflection vs. actuator force (load) behavior to cyclic deflection during cyclic test on specimen LS-3.

Cyclic test data (Load, midspan displacement and rotation at load point and support) was periodically recorded at every 10,000 cycles. The recorded data indicates that the stiffness of the specimens (slope of load-midspan deflection curve) remained unchanged during the cyclic testing, i.e., there was no global damage observed (Figure 8.11). However, the structural stiffness of specimen LS-3 was measured to be lower than those of the other two specimens while specimen LS-1 and LS-2 had a similar stiffness. This is due to the relatively low reinforcement ratio of LS-3, which was deliberately chosen based on relatively low reinforcement stress in ECC link slabs compared to concrete link slab. Realization of low structural stiffness will be an advantage of an ECC link slab since the structural effect on the main bridge span can be minimized when the link slab acts more like a hinge rather than a continuous element.

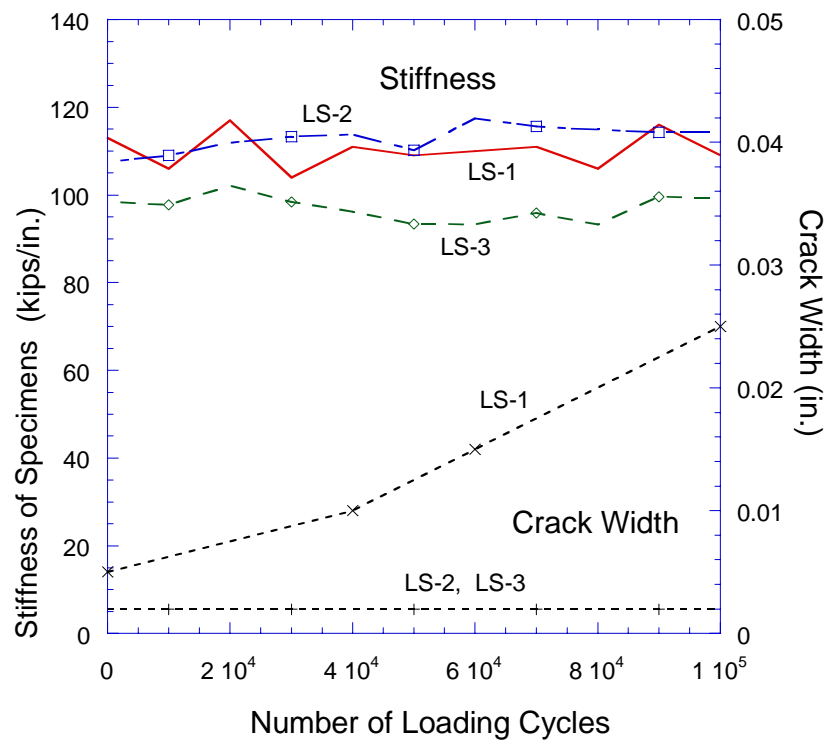


Figure 8.11 Stiffness change and crack width evolution of link slab specimens during cyclic test

Although global damage did not occur in any of the specimens, the cracking patterns were distinctly different for the concrete and ECC link slabs. For LS-1, no additional cracks were seen and the existing cracks generated during the pre-loading stage gradually grew wider. The crack widths in concrete ultimately reached 0.025” at 100,000

loading cycles (Figure 8.11), which corresponds to a permeability coefficient of 10^{-2} in/s, as revealed in Figure 4.7. In contrast, additional microcracks appeared as the number of loading cycles increased for in ECC link slab specimens (LS-2 and LS-3), while the existing crack widths were maintained below 0.002", slightly opening and closing at the maximum and minimum loads, up to 100,000 cycles. As shown in Figure 4.7, the 0.002" crack width in ECC specimens relates to a small permeability of 10^{-9} in/s, which is 7 magnitudes lower than that of concrete. This laboratory testing of ECC link slab again suggests that the low permeability of ECC due to tight crack width control by itself is expected to positively affect the durability of an ECC link slab, particularly under severe environmental conditions.

Figure 8.12 presents the comparison of the marked crack pattern between LS-1, LS-2, and LS-3. A large number of hairline cracks were observed in the ECC link slab specimens while a small number of large cracks in LS-1 specimen were observed. This demonstrates that fatigue cracking resistance of ECC link slabs, in terms of crack width, is independent of the reinforcement ratio because of the inherent multiple cracking and tight crack width control of ECC. Such reduced crack width and high ductility in ECC indicate the potential realization of macroscopically crack free concrete bridge deck systems with ECC material in link slabs. It is also expected that the low permeability of ECC due to relatively small crack widths will enhance the durability of an ECC link slab particularly under severe environmental conditions, such as in regions where deicing salts are frequently used.

Besides the stress limitation requirement described above, the current design procedure of concrete link slab also requires limiting the maximum crack width at the top of the link slab. A minimum reinforcement ratio 0.015 has been suggested with a clear cover of 2.5 in. for controlling the crack width in the concrete link slab (Oesterle et al, 1999). Therefore, the inherent tight crack width of ECC material is expected to provide a more efficient link slab design due to the decoupling of crack width and reinforcement ratio in addition to other advantages represented by enhanced durability, lower structural stiffness and compatible deformation of ECC link slabs.

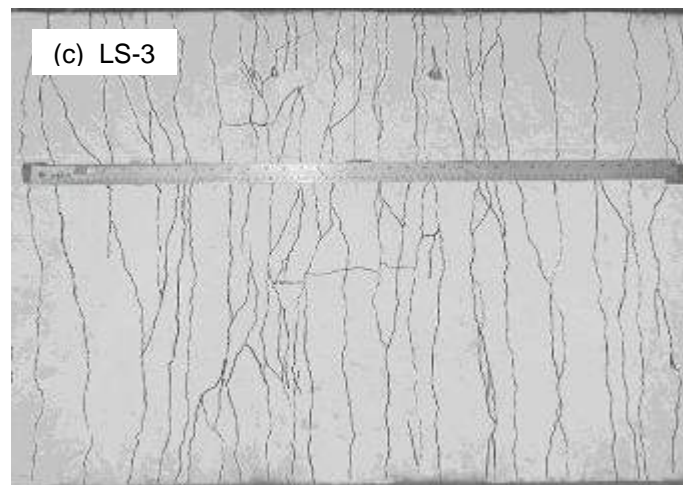
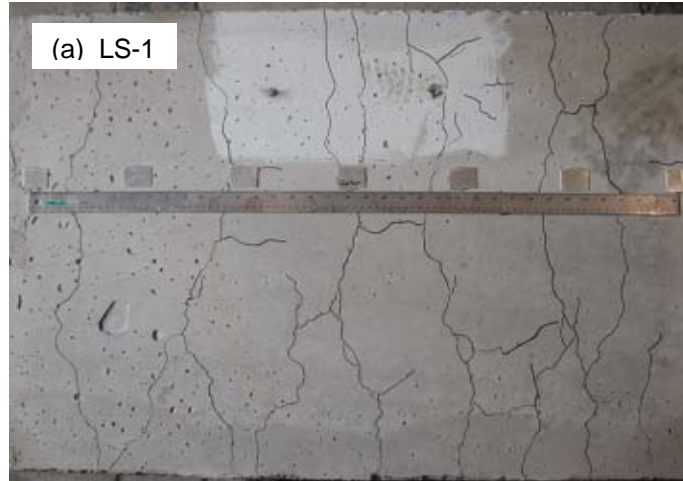


Figure 8.12 Crack pattern marked with black ink pen after cyclic test for (a) LS-1; (b) LS-2 and (b) LS-3.

It should also be noted that there was no cracking observed at the interface between R/C deck slab and ECC link slab (Figure 8.13). In contrast, the cracking formed over the debond span of link slab up to the location of shear studs. This indicates that cracks should have appeared at the concrete/ECC interface if it had been located at the end of debond zone. The modification of the design to locate the concrete/ECC material interface away from the structural interface between the debond zone and girder/deck composite zone prevented cracking at the material interface. Furthermore, the additional shear studs placed between these two interfaces provided composite action between girder and ECC slab. As a result, concrete/ECC interface cracking caused by stress concentrations is prevented. Instead, cracking is limited to within the bulk part of ECC, where higher strength and sufficient strain capacity exist to accommodate the higher stress. This modification of the interface from conventional link slab design will provide enhanced integrity of concrete/ECC interface, preventing undesirable interfacial cracking, which has been partially demonstrated in Section 6.

8.5 Conclusions from laboratory testing of ECC link slab

To demonstrate the potential realization of a durable concrete bridge deck system by the use of an ECC material in link slabs, monotonic and subsequent cyclic tests of full-scale ECC link slabs were performed. The test results were compared with those of a conventional concrete link slab. Prior to the preparation of the link slab specimens, a proper ECC material was chosen for meeting the property requirements for link slab applications. The following conclusions can be drawn from the current experimental results:

1. Property requirements of ECC material for link slabs were examined prior to material choice. It was revealed that the property requirements for link slab applications were satisfied with the hardened properties of ECC material chosen in the present study. This ECC exhibited strain-hardening behavior with tensile strain capacity of 3-5% accompanied by multiple cracking with crack widths below 0.004" while maintaining workability suitable for large volume mixing and casting in the field.

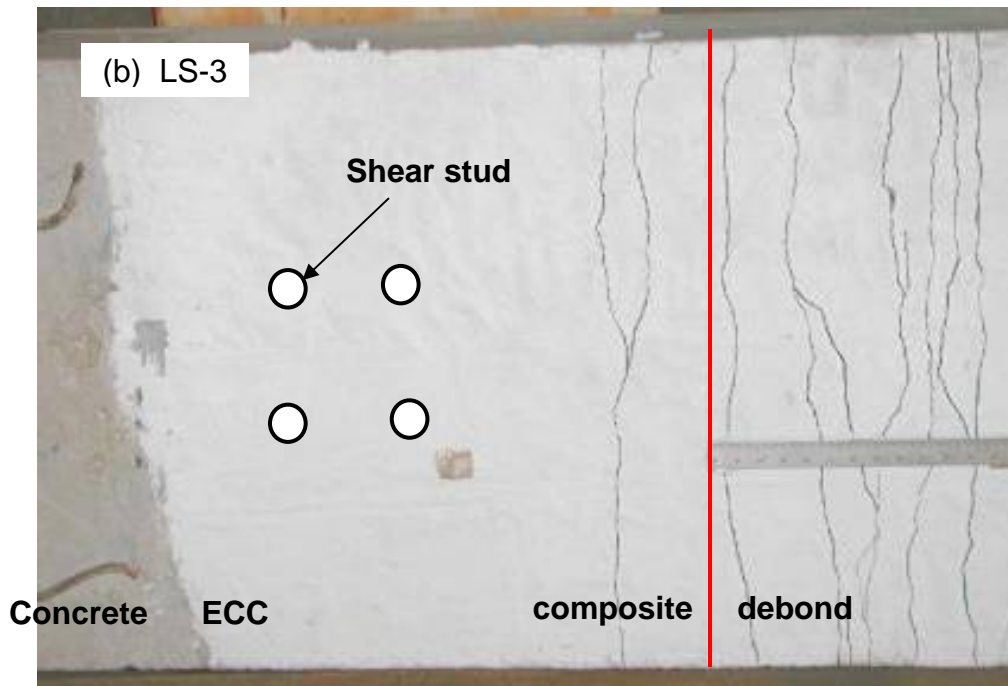
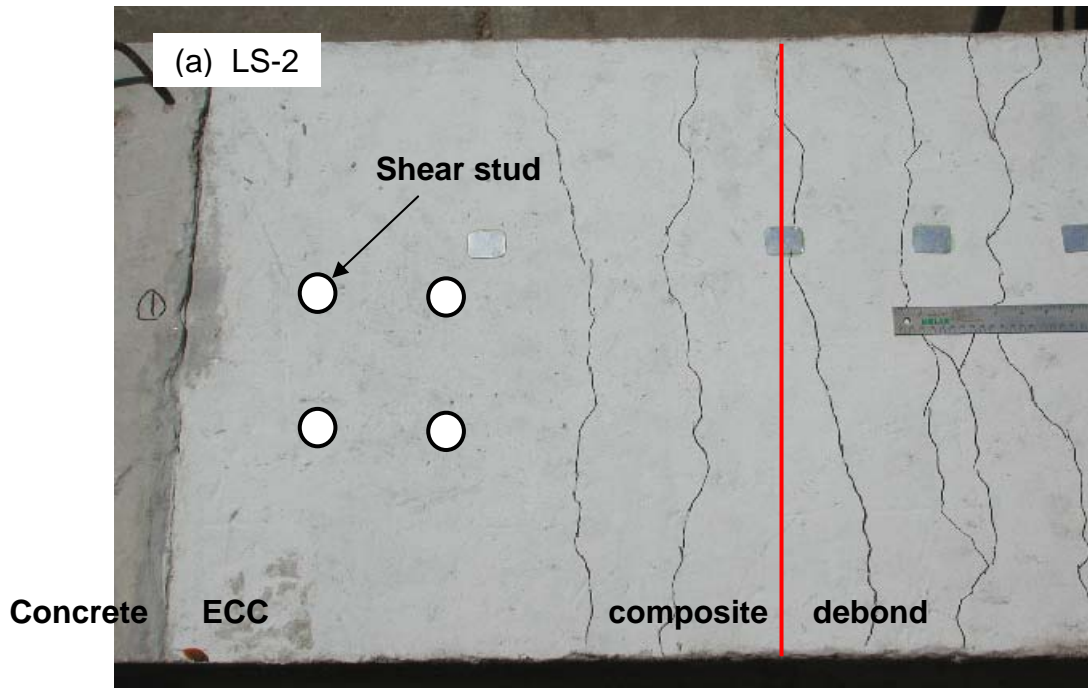


Figure 8.13 Crack pattern marked with black ink pen at tension surface of transition region between debond zone and composite section in (a) LS-2; and (b) LS-3.

2. Monotonic test results revealed the compatible deformation mode of the ECC link slab. The high tensile ductility of ECC material allows the ECC matrix to deform compatibly with the reinforcing bars. As a result, yielding of the reinforcement was delayed in the ECC matrix when compared with that in the concrete matrix. Lower reinforcement stress in the ECC link slab implies a smaller amount of reinforcing bars required, resulting in lower structural stiffness of the link slab. The lower reinforcement stress is confirmed in the ECC link slab, in comparison to the reinforcement stress in the concrete link slab, at the same reinforcement ratio.

3. From the monotonic tests, the maximum tensile strain in the ECC link slab measured at the design end rotation angle remained within the early strain-hardening regime. This confirmed the adequacy of the strain capacity of the ECC used in this study. Indeed, there is room to employ an ECC with slightly lower tensile strain capacity, with potential material cost saving.

4. The cyclic tests performed on three link slabs revealed that the stiffness of the three specimens remained unchanged during cyclic testing. However, the crack widths of the concrete link slab (0.025”) at 100,000 loading cycles were substantially larger than those of the ECC link slabs (< 0.002”), by one order of magnitude. The tight crack width of ECC under cyclic loading will positively contribute to the durability of an ECC link slab and the potential realization of durable concrete deck systems as well. In terms of crack width limitations, the use of ECC, with crack widths and spacing as inherent material properties, will decouple the dependency of crack width on the amount of reinforcement, i.e. the reinforcement ratio. This decoupling allows the simultaneous achievement of structural need (lower flexural stiffness of the link slab approaching the behavior of a hinge) and durability need (crack width control) of the link slab.

5. There was no cracking observed at the interface between ECC link slab and R/C deck slab during cyclic testing, while cracking formed over the debond span of the link slab up to the shear studs. This is due to the fact that the modified location of concrete/ECC interface as well as the additional shear studs installed in ECC link slab, caused a shifting of the stress concentration from the concrete/ECC interface to the inner part of the ECC link slab. This modification is expected to provide enhanced integrity of the interface, preventing interfacial cracking.

The above conclusions support the contention that durable jointless concrete bridge decks may be designed and constructed with ECC link slabs.

9.0 Design guideline of ECC link slab

Notation of live load, geometry, material properties

A_s	=	Total area of longitudinal reinforcement in ECC link slab
B_{ls}	=	Width of ECC link slab (same as width of bridge deck)
E_{ECC}	=	Elastic modulus of ECC
EI_{sp}	=	Flexural rigidity of the bridge section (girder and concrete deck)
H_{ls}	=	Height of ECC link slab
$I_{ls,g}$	=	Moment of inertia of ECC link slab (uncracked)
L_{dz}	=	Length of debond zone = (5 % L_{sp}) x 2
L_{ls}	=	Length of ECC link slab
L_{sp}	=	Length of bridge span (assuming same length for adjacent spans)
M_a	=	Design moment assuming a uncracked link slab
$M_{a,cr}$	=	Actual moment developed in a cracked link slab
P	=	Live load
w_{max}	=	Maximum crack width at the tension face of the link slab
θ	=	Expected rotation angle
ρ	=	Reinforcement ratio of ECC link slab, $A_s / B_{ls} H_{ls}$
σ_f	=	First crack strength of ECC
σ_s	=	Stress of reinforcement
σ_y	=	Yield strength of steel

Current design criteria for concrete link slabs are the stress in the reinforcement (σ_s) at an expected rotation angle (θ), and the maximum crack width (w_{max}) at the tension face of the link slab. As detailed in Section 1, the derivation of the stress in the reinforcement is conservative, yet incorrect since the expected applied moment (M_a) is determined assuming a uncracked link slab, which is consequently relatively stiff and will develop a relatively large resisting moment at a given imposed rotation angle. In

reality, the concrete link slab resists the moment M_a in the cracked condition. However, the reinforcement ratio ρ is chosen for an expected moment M_a in the uncracked condition.

By assuming the ECC link slab in an uncracked condition, the design moment (M_a) at the expected rotation angle (θ_{exp}) will exceed the actual moment ($M_{a,cr}$) that the ECC link slab develops at this angle in the cracked condition. This leads to a conservative estimate of the required amount of longitudinal reinforcement in the link slab to satisfy the limit stress criterion ($\sigma_s < 0.4\sigma_y$). Unlike the concrete link slab, however, the minimum reinforcement ratio for limiting crack width is not considered in ECC link slab design, since the use of ECC, with crack width and spacing as inherent material properties, decouples the dependency of crack width on the amount of reinforcement, i.e. the reinforcement ratio.

Based on the results of the present study, a simple design method can be developed as follows:

Scope

This design guideline provides minimum requirements for design of ECC link slab for retrofit of existing simple span bridges.

For ECC material used in this design, the specified ultimate tensile strain capacity shall not be less than computed by equation 9-1.

The material shall exhibit multiple cracking with controlled crack width ($< 0.004''$) and spacing ($< 0.1''$) in uniaxial tension test.

The specified compressive strength shall not be less than 4,500psi.

$$\varepsilon_{ls} = \frac{\alpha_T \cdot \Delta T \cdot \beta L_{sp}}{L_{dz}} + \varepsilon_{sh} + \varepsilon_{LL} \quad (\text{Eq. 9-1})$$

where:

ε_{ls} : required tensile strain capacity

ε_{sh} : shrinkage strain of ECC

ε_{LL} : maximum tensile strain due to live load

α_T : coefficient of thermal expansion of the span

ΔT : temperature variation

β : support type factor; for Hinge-Roller-Roller-Hinge type support, $\beta = 2$
 (as shown in Figure 3.2)
 for Hinge-Roller-Hinge-Roller type support, $\beta = 1$

Step 1 Determine Length of ECC link slab, L_{ls} , and length of debond zone, L_{dz}
 Length of ECC link slab, L_{ls} , is the sum of 7.5% of each adjacent girder span. Debonding of 5% of each girder span for the ECC link slab is provided to reduce stiffness. Caner and Zia (1998) indicated that the load-deflection behavior of jointless bridge decks supported by simple span girders is not affected by debond length up to 5% of the span length.

Step 2 Determine end rotation angle of spans, θ_{max}

The rotation angle θ is a function of the geometry of the spans, their loading, and material properties. In this procedure, the maximum rotation angle θ_{max} (0.00375 rad.) is employed, which corresponds to the allowable deflection of a bridge span under live load (Δ_{max} , $L_{sp}/800$ based on MDOT bridge design and AASHTO code), as shown in Figure 9.1. The conservatism of using a single point load to replace a more complex truck load, such as HS-20, HS-25, in the calculation of the midspan deflection of the bridge is proven in the Appendix 11.2.

$$\theta_{max} = \frac{\Delta_{max}}{\Delta} \theta = \frac{\Delta_{max}}{PL_{sp}^3 / 48EI_{sp}} \frac{PL_{sp}^2}{16EI_{sp}} = \frac{L_{sp}}{800} \frac{3}{L_{sp}} = 0.00375 \text{ rad.} \quad (\text{Eq. 9-2})$$

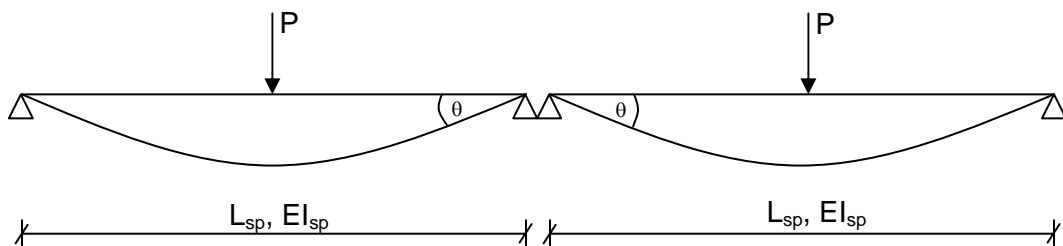


Figure 9.1 Simplified geometry and loading of two-span bridge structure

Step 3 Determine moment of inertia of link slab (uncracked)

The moment of inertia of the link slab in the uncracked condition is a function of the cross-sectional geometry and independent of the reinforcement ratio.

$$I_{ls,g} = \frac{B_{ls} H_{ls}^3}{12} \quad (\text{Eq. 9-3})$$

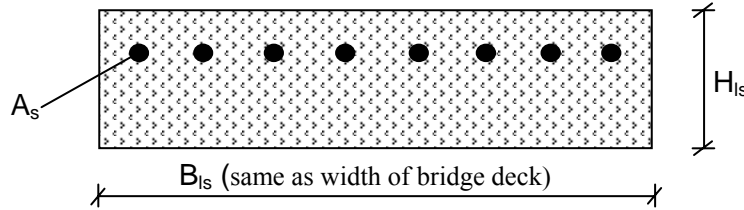


Figure 9.2 Cross-sectional dimensions and reinforcement of link slab in uncracked condition

Step 4 Determine moment M_a developed in the link slab at rotation angle θ_{max}

The moment developed in the uncracked ECC link slab is a function of the material properties and geometrical dimensions. It is proportional to the imposed rotation angle θ_{max} .

$$M_a = \frac{2E_{ECC} I_{ls,g}}{L_{dz}} \theta_{max} \quad (\text{Eq. 9-4})$$

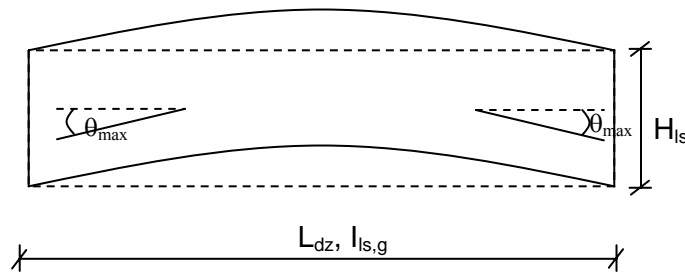


Figure 9.3 Deformed shape of link slab at imposed rotation angle θ

Step 5 Determine required longitudinal reinforcement ratio

The amount of reinforcement is calculated by non-linear sectional analysis (shown in the Appendix 11.1), based on the assumption that ECC is an elastic-perfectly plastic material, as shown in Figure 9.4. The reinforcement ratio is designed using a conservative working stress, such as 40% of the yield strength of the reinforcement, based on M_a . In order to satisfy this condition ($\sigma_s \leq 0.40\sigma_y$), the amount of reinforcement (A_s), i.e. the reinforcement ratio ρ , is to be adjusted.

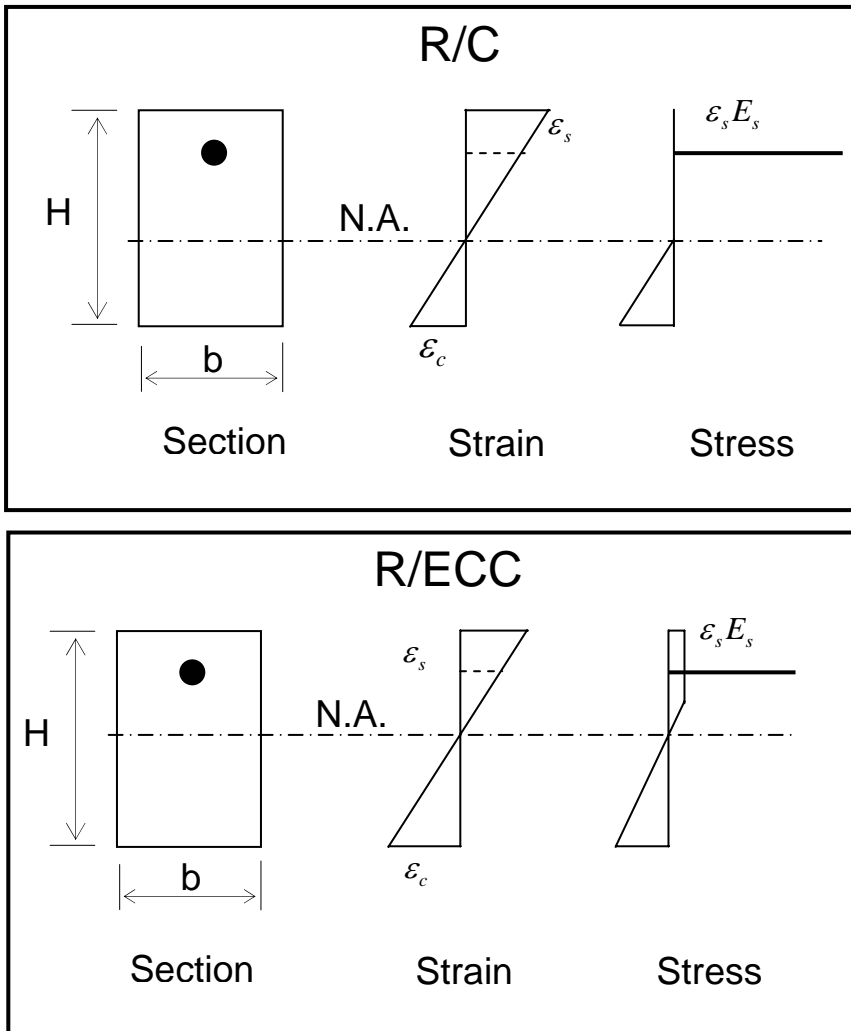
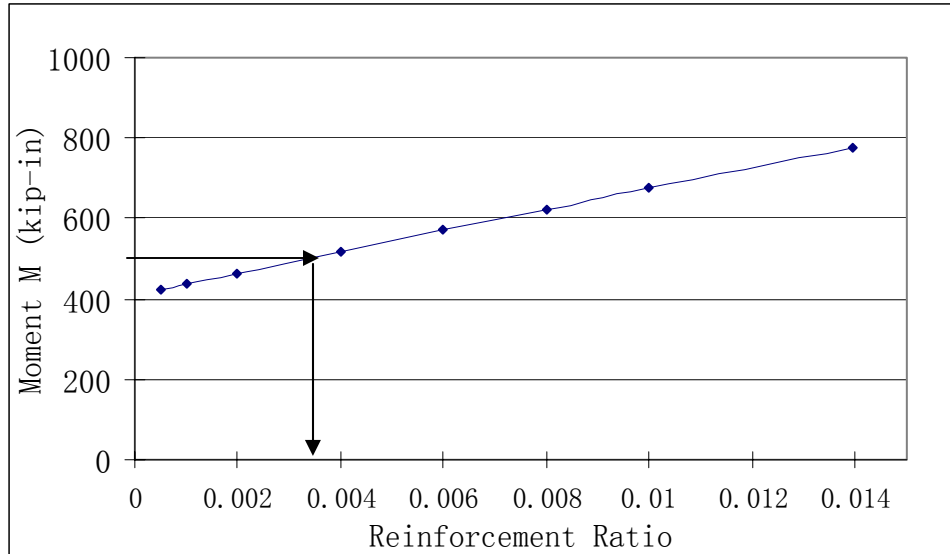


Figure 9.4 Schematic stress and strain profile in a cross section of link slab for calculation of required longitudinal reinforcement ratio (profile of R/C is shown for comparison)

As shown in Figure 9.5, a simple design chart has been developed based on aforementioned concept and assuming a link slab width b of 28 in (Appendix 11.1). To use this design chart, first calculate the 28 inch portion of the imposed maximum moment M_a , i.e., $M = (28/B_{ls}) M_a$. Then find the corresponding reinforcement ratio from the design curve, revealed in Figure 9.5, which is the required longitudinal reinforcement ratio.



Note: $b = 28$ inch, $h = 9$ inch, $E_{ECC} = 2500$ ksi, $\sigma_f = 0.5$ ksi, $E_s = 29000$ ksi, $\sigma_y = 60$ ksi assumed.

Figure 9.5 Design chart for required longitudinal reinforcement ratio

Step 6 Shear connectors (Shear studs) in the interface region

In the interface region between the ECC link slab and the concrete deck, the location of shear studs connecting the steel girder and the bridge deck are extended within the ECC link slab by 2.5% of span length, reducing interfacial stress (Figure 9.6). The AASHTO code can be applied for the design of shear studs in the transition zone. According to the results of pushout tests on ECC specimens, the shear load capacity of ECC/stud connection is higher than that determined based on the AASHTO code. Fifty percent more shear studs, compared to that in simple span bridge, is suggested to be placed in the transition zone to account for the stress concentration at the end of debond zone.

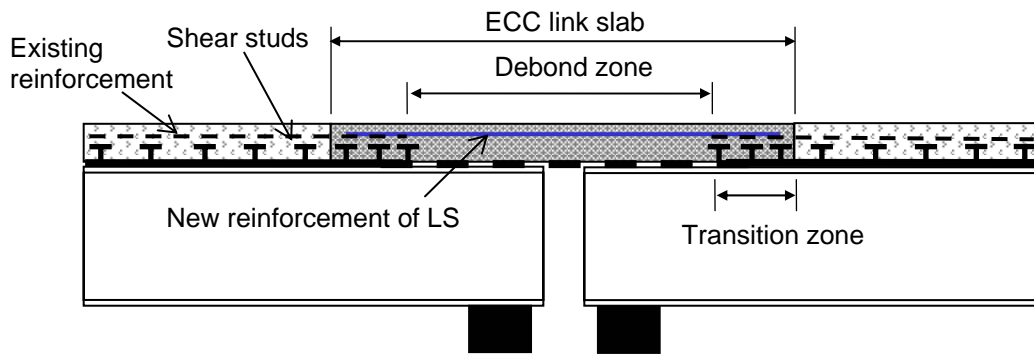


Figure 9.6 Conceptual illustration of the interface design between ECC link slab and concrete deck

Step 7 Lap splice in the interface region

In addition to these shear studs, the existing longitudinal reinforcement is lap spliced with new reinforcing bars in the interface region. The AASHTO code can be used for the design of lap splices. From the test of reinforcement pullout in ECC, it was found that ECC specimens show ductile frictional pullout behavior, without any splitting and transverse macrocracking; therefore the adoption of the AASHTO code will provide a conservative design. The end of the new reinforcement is suggested to be placed away from the interface by 6” and staggered by 24”. This is for the purpose of preventing a stress concentration at the end of the new reinforcement located at the concrete/ECC interface.

10.0 Conclusions

The mechanical property requirements of ECC material for link slabs were examined prior to material design. It was revealed that the requirements for link slab applications were satisfied by the hardened properties of the specific ECC material chosen (M45). This ECC exhibited strain-hardening behavior with tensile strain capacity of around 3.5%, accompanied by multiple cracking with crack widths below 4mil, while maintaining workability suitable for large volume mixing and casting in the field. The 3-month and 6-month strain capacity of M45 is roughly 3.0%, which remains acceptable for an ECC link slab application.

Despite relatively large free shrinkage deformations in ECC, the durability of an ECC link slab is expected to be superior to that of a concrete link slab due to the tight crack widths in ECC ($\sim 0.003''$) under restrained drying shrinkage, resulting in drastically reduced permeability. Even with the large shrinkage strain in ECC ($\sim 0.1\%$), it remains in the early strain-hardening regime ($>3\%$ strain capacity). The use of a low-alkali cement in ECC is not recommended since it has minimal influence on drying shrinkage as compared with using ordinary Portland cement in Michigan.

Testing on freeze-thaw behavior indicates that ECC provides superior resistance to deterioration when subjected to freeze-thaw cycles. Due to the high number of micro-pores entrained in the matrix, the void space provided for water expansion and escape by the ECC is adequate for excellent freeze-thaw protection. These micro-pores may be accompanied by larger pores not sensitive to mercury intrusion, which may be adding to the freeze-thaw protection capability.

A 6 inch embedment length (1/2 of the development length required by AASHTO code) was shown to ensure yielding of epoxy-coated reinforcement in ECC pullout specimens. This demonstrates that the development lengths determined according to the AASHTO code will be adequate (on the conservative side) for the design of the ECC link slab/concrete bridge deck interface. It is also noted that there was no reduction in bond properties observed for epoxy-coated reinforcement in ECC compared to bare steel reinforcement.

The pullout failure mode of reinforcement within ECC specimens (frictional pullout) is more ductile when compared to concrete specimens (splitting) due to the high toughness and ductility of ECC material. Therefore, the required lap splice length determined according to the AASHTO code is expected to be conservative for the design of reinforcing bars in ECC since the modification factors (1.3 or 1.7) were employed to address potential brittle failure of the lap splice in concrete.

The pushout behavior and failure mode of ECC specimens were found to be much more ductile than concrete due to the ductile nature of ECC and resulting microcracks developed around shear studs, followed by large deformation of the studs. The average load capacity per stud in ECC specimens sustained higher value than calculated based on AASHTO code requirements, due to the shift of failure mode from brittle matrix fracture

to ductile steel yielding. The adoption of the AASHTO code for stud design in ECC is expected to be conservative in terms of load capacity and failure mode.

Monotonic testing of ECC link slab revealed the compatible deformation mode of the ECC link slab. The high tensile ductility of ECC material allows the ECC matrix to deform compatibly with the reinforcing bars. As a result, yielding of the reinforcement was delayed in the ECC matrix when compared with that in the concrete matrix. Lower reinforcement stress in the ECC link slab implies a smaller amount of reinforcing bars required, resulting in lower structural stiffness of the link slab. The lower reinforcement stress is confirmed in the ECC link slab, in comparison to the reinforcement stress in the concrete link slab, at the same reinforcement ratio.

From the monotonic tests, the maximum tensile strain in the ECC link slab measured at the design end rotation angle remained within the early strain-hardening regime. This confirmed the adequacy of the strain capacity of the ECC used in this study. Indeed, there is room to employ an ECC with slightly lower tensile strain capacity, with potential material cost saving.

The cyclic tests performed on three link slabs revealed that the stiffness of the three specimens remained unchanged during cyclic testing. However, the crack widths of the concrete link slab (0.025”) at 100,000 loading cycles were substantially larger than those of the ECC link slabs (< 0.002”), by one order of magnitude. The tight crack width of ECC under cyclic loading will positively contribute to the durability of an ECC link slab, and the potential realization of durable concrete deck systems as well. In terms of crack width limitations, the use of ECC, with crack widths and spacing as inherent material properties, will decouple the dependency of crack width on the amount of reinforcement, i.e. the reinforcement ratio. This decoupling allows the simultaneous achievement of structural need (lower flexural stiffness of the link slab approaching the behavior of a hinge) and durability need (crack width control) of the link slab.

There was no cracking observed at the interface between ECC link slab and R/C deck slab during cyclic testing, while cracking formed over the debond span of the link slab up to the shear studs. This is due to the fact that the modified location of concrete/ECC interface as well as the additional shear studs installed in ECC link slab, caused a shifting of the stress concentration from the concrete/ECC interface to the part of

the ECC link slab. This modification is expected to provide enhanced integrity of the interface, preventing interfacial cracking.

The above conclusions support the contention that durable jointless concrete bridge decks may be designed and constructed with ECC link slabs. Based on the above findings, a simple design guideline is presented.

11.0 Appendix

11.1 Non-Linear Sectional Analysis

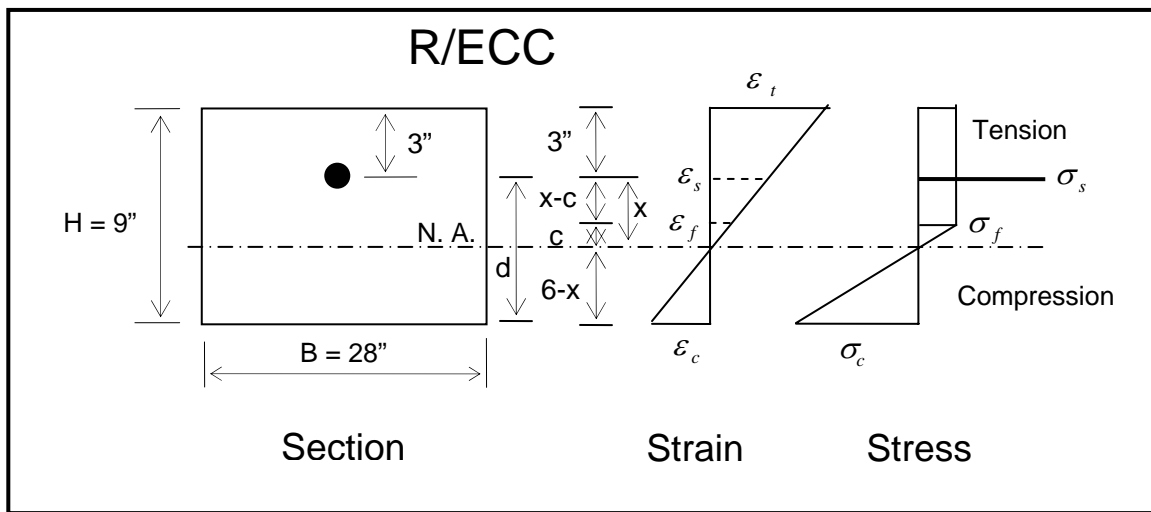


Figure 11.1 Strain and stress profile in a cross section of ECC link slab for calculation of required longitudinal reinforcement ratio/moment capacity

Note: In this calculation, the geometry of the link slab is the same as these tested and described in this research project (shown in Figure 11.1) and the material properties are assumed as follows:

$$E_{\text{ECC}} = 2500 \text{ ksi}$$

$$\sigma_f = 0.5 \text{ ksi}$$

$$E_s = 29000 \text{ ksi}$$

$$\sigma_y = 60 \text{ ksi}$$

Assuming a certain reinforcement ratio ρ ($\rho = A_s / BH$, defined in step 2 of Section 2.1), we can solve for moment capacity M by non-linear sectional analysis and by limiting the stress in reinforcement to $0.4\sigma_y$. (Alternatively, given a known moment

capacity M, we can solve for the required reinforcement ratio ρ utilizing the same method. However, it is more convenient to calculate using the first procedure while the result should be the same.)

$$\varepsilon_s = \frac{\sigma_s}{E_s} = \frac{0.4\sigma_y}{E_s} = \frac{0.4(60)}{29000} = 0.0008276$$

$$\varepsilon_f = \frac{\sigma_f}{E_{ECC}} = \frac{0.5}{2500} = 0.0002$$

$$\frac{c}{x} = \frac{\varepsilon_f}{\varepsilon_s} = \frac{0.0002}{0.0008276} \Rightarrow x = 4.14c$$

$$\text{Similarly, } \frac{c}{6-x} = \frac{\varepsilon_f}{\varepsilon_c} = \frac{c}{6-4.14c} \Rightarrow \varepsilon_c = \frac{0.0002(6-4.14c)}{c}$$

Since the net force $\sum F$ equal to zero over the cross section of the link slab, therefore,

$$\sigma_s \rho \times 9 \times 28 + \sigma_f (x - c + 3) \times 28 + 0.5 \sigma_f c \times 28 - 0.5 E_{ECC} \varepsilon_c (6 - x) \times 28 = 0$$

Plug the actual value into above equation as follows:

$$24 \times \rho \times 9 + 0.5(3.14c + 3) + 0.5 \times 0.5 \times c - 0.5 \times 2500 \frac{0.0002(6 - 4.14c)^2}{c} = 0$$

The above equation can be reduced to:

$$c^2 - 5.65c - 87.63\rho c + 3.65 = 0$$

Assuming ρ equal to 0.01, therefore, the above equation becomes:

$$c^2 - 6.53c + 3.65 = 0$$

$$\Rightarrow c = \frac{6.53 \pm \sqrt{6.53^2 - 4 \times 3.65}}{2} = \frac{6.53 \pm 5.30}{2} = \begin{cases} 5.915" (\text{Not apply}) \\ 0.615" (\text{Apply}) \end{cases}$$

Hence, the moment capacity of the section can be calculated as follows (moment about neutral axis):

$$\begin{aligned} M_{ECCTen} &= \sigma_f (3 + 3.14c) \times 28 \times (0.5(3 + 3.14c) + c) + 0.5 \times 0.5 \times 28c \times 2c/3 \\ &= 212.6 + 1.8 \\ &= 214.4(\text{kip-in}) \end{aligned}$$

$$M_{SteelTen} = 0.4\sigma_y \rho \times 9 \times 28 \times 4.14c = 154.0(\text{kip-in})$$

$$M_{ECCComp} = 0.5E_{ECC}\varepsilon_c \times 28(6 - 4.14c)^2 \times 2/3 = 312.7(\text{kip-in})$$

$$\text{Finally, } M = M_{ECCTen} + M_{SteelTen} + M_{ECCComp} = 214.4 + 154.0 + 312.7 = 681.1(\text{kip-in})$$

Therefore, given ρ equal to 0.01, M is revealed 681.1 kip-in and vice versa. With varying ρ , M can be obtained correspondingly and plotted as shown in Figure 9.5, which can then be utilized for the design of the reinforcement ratio of the link slab.

$$\text{Check: } \frac{\varepsilon_f}{\varepsilon_t} = \frac{c}{3 + 4.14c} = \frac{0.615}{5.5461} = 0.11$$

$$\Rightarrow \max_tensile_strain \varepsilon_t = 0.18\% \ll 3\%(\text{Strain_capacity}) \text{ OK}$$

$$\sigma_c = E_{ECC}\varepsilon_c = 2500 \frac{0.0002(6 - 4.14c)}{c} = 2.8\text{ksi} < 8.7\text{ksi}(\text{Compressive_strength})$$

OK

11.2 Simplified Loading of Bridge Span

Using the bridge model shown in Figure 11.2 (For simplicity, only a I section W44X335 with a moment of inertia of 31100 in⁴ is used), the conservatism of using a single point load to replace a more complex truck load, such as HS-20, HS-25, in the calculation of the midspan deflection of the bridge can be proven as follows:

First, a single point load with the same magnitude as HS-20 is applied in the midspan, as shown in Figure 11.2 (a), the deflection at the midspan, $\delta_1 = PL^3/48EI$, is 0.8 in. Then the HS-20 truck load was applied in the midspan (Figure 11.2 (b)) and a deflection, δ_2 , of 0.7 in was obtained, which means the single point load does give a conservative value as compared to HS-20 truck load. Similar conclusion can be drawn for HS-25 truck load since deflection is proportional to the load applied. Therefore, it is appropriate and conservative to use a simplified midspan point load to replace the more complicated HS-20 or HS-25 truck load in the structural analysis in terms of the deflection.

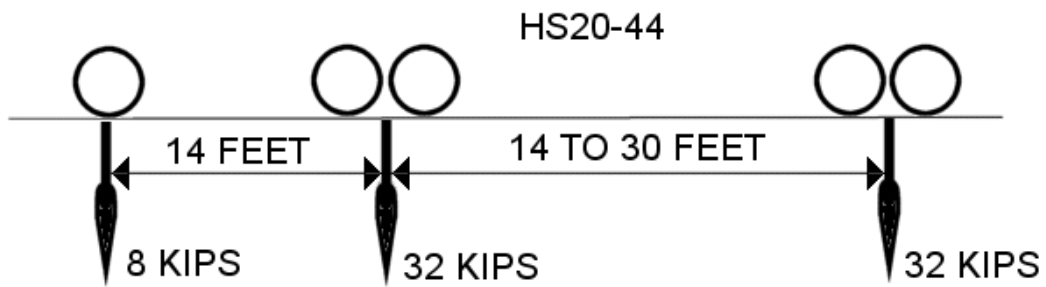
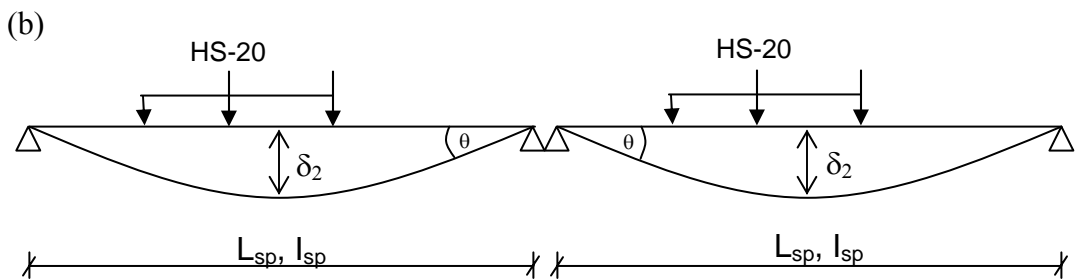
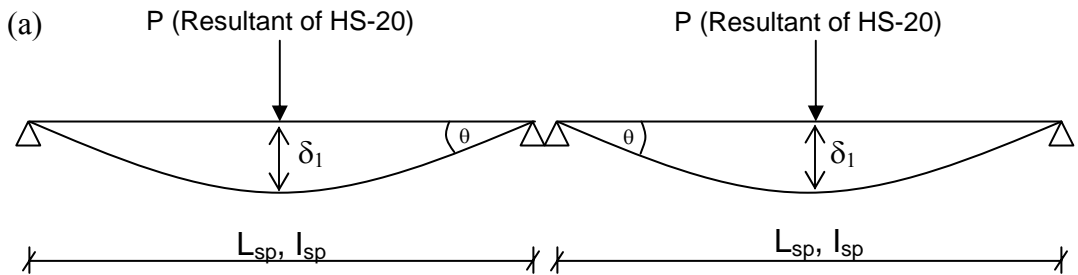


Figure 11.2 Schematics of two span simply supported bridge and loading for (a) resultant of HS-20, and (b) HS-20

12.0 References:

- AASHTO, 1996, Standard specifications for highway bridges, 16th edition, American Association of State Highway and Transportation Officials, Washington D.C., p.205
- AASHTO, 2002, Standard Specifications for Highway Bridges, 17th edition, American Association of State Highway and Transportation Officials, Washington D.C., 1052p.
- ACI 318-2002, Building Code Requirements for Structural Concrete and Commentary, 2002, American Concrete Institute, Farmington Hills, Michigan 48333-9094
- Alampalli, S. and A.P. Yannotti, 1998, In-Service Performance of Integral Bridges and Jointless Decks, Transportation Research Record 1624, Paper No. 98-0540,.
- An, L., and Cederwall, K., 1996, Pushout tests on studs in high strength and normal strength concrete, Journal of constructional steel research, Vol. 36, No. 1, pp15-29
- Ashley, S., 1996, Bridging the cost gap with composites. Mech. Eng., 118, pp76-80
- Beltzung, F., Wittmann, F.H. and Holzer, L., 2001, Influence of composition of pore solution on drying shrinkage, in Creep, Shrinkage and Durability Mechanics of Concrete and other Quasi-Brittle Materials, edited by Ulm, F.-J., Bazant, Z.P. and Wittmann, F.H., Elsevier Science Ltd.
- Caner, A. and P. Zia, 1998, Behavior and Design of Link Slab for Jointless Bridge Decks, PCI J., May-June, pp.68-80.
- Cheng-yi, H., and Feldman, R.F., 1985. Dependence of Frost Resistance on the Pore Structure of Mortar Containing Silica Fume. ACI Journal. Pp. 740-743.
- Fischer, G. and V.C. Li, 2002, Influence of Matrix Ductility on Tension-Stiffening Behavior of Steel Reinforced Engineered Cementitious Composites (ECC), ACI Structural Journal, Vol.99, No.1, Jan.-Feb., pp.104-111.
- Gergeley, P., and Lutz, L.A., 1968, Maximum crack width in reinforced concrete flexural members, Causes, Mechanisms, and Control of Cracking in Concrete, SP-20, ACI, Farmington Hills, MI
- Kim, Y.Y., V.C. Li and H.J. Kong, 2003, Development of Sprayable Engineered Cementitious Composites, HPFRCC4, Univ of Michigan, Ann Arbor, MI, pp233-243
- Kong, H.J., S. Bike and V.C. Li, 2003, Constitutive Rheological Control to Develop a Self-Consolidating Engineered Cementitious Composite Reinforced with Hydrophilic

- Poly(vinyl alcohol) Fibers, *Cement and Concrete Composites*, Vol.25, No.3, pp.333-341.
- Li, V.C., Wu, H.C., Maalej, M., and Mishra, D.K., 1996, Tensile Behavior of Cement Based Composites with Random Discontinuous Steel Fibers, *J. American Ceramics Society*, Vol. 79, No. 1, pp. 74-78.
- Li, V.C., 2002, Reflections on the Research and Development of Engineered Cementitious Composites (ECC), *Proceedings of the JCI International Workshop on Ductile Fiber Reinforced Cementitious Composites (DFRCC) - Application and Evaluation (DRFCC-2002)*, Takayama, Japan, Oct. pp.1-21.
- Li, V.C., and G. Fischer, 2002, Reinforced ECC - An Evolution from Materials to Structures, *Proceedings of the First FIB Congress*, Osaka, Japan, pp.105-122.
- Litvan, G.G., 1983, Air Entrainment in the Presence of Superplasticizers. *ACI Journal*. Pp. 326-331
- MacGregor, J.G., 1998, *Reinforced Concrete*, Prentice-Hall, Inc., New Jersey. 939 pp.
- Mindess, S., and Young, J.F., 1981, *Concrete*, Prentice-Hall, Inc., New Jersey. 391 pp.
- Oesterle, R.G., H. Tabatabai, T.J. Lawson, T.M. Refai, J.S. Voltz and A. Scanlon, 1999. *Jointless and Integral Abutment Bridges – Summary Report, Final Report to Federal Highway Administration*, Washington D.C.,
- Ollgaard, J.G., Slutter, R.G., and Fisher, J.W., 1971, Shear strength of stud connectors in lightweight and normal-weight concrete, *AISC Engineering Journal*, April, pp.55-64.
- Pigeon, M., Pleau, R., Azzabi, M., Banthia, N., 1996, Durability of Microfiber-Reinforced Mortars., *Cement and Concrete Research*. Pp. 601-609
- Shah, S.P., Karaguler, M.E. and Sarigaphuti, M.,1992, Effect of Shrinkage-Reducing Admixtures on Restrained Shrinkage Cracking of Concrete, *American Concrete Institute Materials Journal*, 89, pp. 289-295, May-June
- Soudki, K., and Green, M., 1997, Freeze-Thaw Response of CFRP Wrapped Concrete, *Concrete International*, Vol.19, No.8, pp. 64-67
- Toutanji, H., and Balaguru, P., 1999, Effects of Freeze-Thaw Exposure on Performance of Concrete Columns Strengthened with Advanced Composites, *ACI Materials Journal*, Vol.96, No.5, pp. 605-610

- Toutanji, H., and Deng, Y., 2002, Strength and Durability Performance of Concrete Axially Loaded Members with AFRP Composite Sheets, *Composites Part B: Engineering*, Vol.33, No.4, pp. 255-261
- Wang, K., D.C. Jansen, and S. Shah, 1997, Permeability study of cracked concrete, *Cement and Concrete Research*, Vol.27, No.3, pp. 381-393.
- Wolde-Tinsae, A.M. and J.E. Klinger, 1987, Integral Bridge Design and Construction, Report FHWA/MD-87/04, Maryland Department of Transportation, Jan.,
- Yeih, W., Huang, R., Chang, J.J., and Yang, C.C., 1997, A pullout test for determining Interface properties between reinforcement and concrete, *Advanced cement based materials* No. 5, pp8-57-65.
- Zhang, J., and Li, V.C., 2002, Introducing Ductile Strip for Durability Enhancement of Concrete Slabs, *ASCE J. of Materials in Civil Engineering*, Vol .14, No. 3, June, pp. 253-261